

People's Democratic Republic of Algeria
Ministry of Higher Education and Scientific Research



Le génie pour l'industrie

Ecole Nationale Polytechnique
Algiers, Algeria
Department of Mechanical Engineering
Mechanical Engineering and Development Laboratory

Thesis

Presented for obtaining the

Doctor's degree

In Mechanical Engineering

Option: Clean and Renewable Energies-Mechanical Systems

By

Abdelhamid BOUHELAL

Contribution to the aerodynamic study of the air-sand flow around a wind turbine blade

Before the jury members composed of:

Mr. Saïd RECHAK	Professor, ENP, Algiers, Alegria	Chair
Mr. Arezki SMAILI	Professor, ENP, Algiers, Alegria	Supervisor
Ms. Ouahiba GUERRI	Research Director, CDER, Algiers, Algeria	Co-Supervisor
Mr. Christian MASSON	Professor, ETS, Montreal, Canada	Abroad Co-Supervisor
Mr. Rabah DIZENE	Professor, USTHB, Algiers, Algeria	Examiner
Mr. Mohamed SAIGHI	Professor, USTHB, Algiers, Algeria	Examiner
Mr. Bouzid BENKOUSSAS	Professor, ENP, Algiers, Algeria	Examiner
Mr. Abdelhafid BRIMA	Professor, University of Batna 2, Algeria	Invited

ENP 2018

Ecole Nationale Polytechnique (ENP)
10, Avenue des Frères Oudek, Hassen Badi, BP 182 16200 El Harrach, Alger, ALGERIE
www.enp.edu.dz

People's Democratic Republic of Algeria
Ministry of Higher Education and Scientific Research



Le génie pour l'industrie

Ecole Nationale Polytechnique
Algiers, Algeria
Department of Mechanical Engineering
Mechanical Engineering and Development Laboratory

Thesis

Presented for obtaining the

Doctor's degree

In Mechanical Engineering

Option: Clean and Renewable Energies-Mechanical Systems

By

Abdelhamid BOUHELAL

Contribution to the aerodynamic study of the air-sand flow around a wind turbine blade

Before the jury members composed of:

Mr. Saïd RECHAK	Professor, ENP, Algiers, Alegria	Chair
Mr. Arezki SMAILI	Professor, ENP, Algiers, Alegria	Supervisor
Ms. Ouahiba GUERRI	Research Director, CDER, Algiers, Algeria	Co-Supervisor
Mr. Christian MASSON	Professor, ETS, Montreal, Canada	Abroad Co-Supervisor
Mr. Rabah DIZENE	Professor, USTHB, Algiers, Algeria	Examiner
Mr. Mohamed SAIGHI	Professor, USTHB, Algiers, Algeria	Examiner
Mr. Bouzid BENKOUSSAS	Professor, ENP, Algiers, Algeria	Examiner
Mr. Abdelhafid BRIMA	Professor, University of Batna 2, Algeria	Invited

ENP 2018

Ecole Nationale Polytechnique (ENP)
10, Avenue des Frères Oudek, Hassen Badi, BP 182 16200 El Harrach, Alger, ALGERIE
www.enp.edu.dz

République Algérienne Démocratique et Populaire
Ministère de l'Enseignement Supérieur et de la Recherche Scientifique



Le génie pour l'industrie

Ecole Nationale Polytechnique d'Alger, Algérie
Département de Génie Mécanique
Laboratoire de Génie Mécanique et de Développement

Thèse de Doctorat

En Génie mécanique

Option: Systèmes Mécaniques à Energies Propres Renouvelables

Présentée par

Abdelhamid BOUHELAL

Contribution à l'étude aérodynamique de l'écoulement air-sable autour d'une pale d'éolienne

Devant le jury:

Mr. Saïd RECHAK	Professeur, ENP, Alger, Algérie	Président
Mr. Arezki SMAILI	Professeur, ENP, Alger, Algérie	Directeur de thèse
Mme. Ouahiba GUERRI	Directrice de recherche, CDER, Alger, Algérie	Co- Directeur
Mr. Christian MASSON	Professeur, ETS, Montréal, Canada	Co- Directeur à l'étranger
Mr. Rabah DIZENE	Professeur, USTHB, Alger, Algérie	Examineur
Mr. Mohamed SAIGHI	Professeur, USTHB, Alger, Algérie	Examineur
Mr. Bouzid BENKOUSSAS	Professeur, ENP, Alger, Algérie	Examineur
Mr. Abdelhafid BRIMA	Professeur, Université de Batna 2, Algérie	Invité

ENP 2018

Dedication

I would like to dedicate this modest work:

To my dear father: Mohamed Laid and To my dear mother: Khadidja

To my brother: Mamar and To all my sisters: Imane, Djamila, Zineb, Aicha and Chifa

To my sister's husband: Omrane and To their little son: Djawad

To all members of my family and To all my dear and faithful friends

Acknowledgements

First and foremost, I thank **ALLAH**, who gave me life and health, I am grateful for his help in the realization of this thesis.

There are a number of people without whom this thesis might not have been written, and to whom I am greatly indebted.

First, I would like to thank my thesis supervisor, **Pr. Arezki SMAILI** (Professor, Ecole Nationale Polytechnique (ENP), Algiers) for having entrusted me with this research work and for his availability throughout the project, for providing me with an excellent atmosphere for doing research, his excellent guidance, understanding and patience. I am very grateful to him for the quantity and the quality of the scientific information that he gave me, which made me greatly benefit from his experience in this field of research (aerodynamics of wind turbines). I am very grateful for his efforts and his time, which he devoted so patiently for succeeding this work.

In the second place, I would like to thank **Dr. Ouahiba GUERRI** (Director of research, Centre de Développement des Energies Renouvelables (CDER), Algiers). I am very grateful for her time, help and constant encouragement during the years of this thesis. I am very grateful to her for the quantity and the quality of the scientific information that she gave me, which made me greatly benefit from her experience in the field of aerodynamics of wind turbines.

I am very grateful to **Pr. Christian MASSON** (Professor, Ecole de Technologie Supérieure (ETS), Montreal), my abroad supervisor, who has accepted me to work in his great laboratory of aerodynamics and helped me gain new insights into mechanical engineering. He, with his great personality, not only supervised my research but also did not hesitate to support me in every aspect of life as an international graduate

student. I would also like to thank him for all the scientific and pedagogical help that he gave me during my mobility: funding, giving access to the supercomputer, his availability, his valuable suggestions, his recommendations and for his time.

I also avail myself of this opportunity to thank members of my thesis committee: **Pr. Saïd RECHAK** (Professor, ENP, Algiers), **Pr. Rabah DIZENE** (Professor, USTHB, Algiers), **Pr. Mohamed SAIGHI** (Professor, USTHB, Algiers) and **Pr. Bouzid BENKOUSSAS** (Professor, ENP, Algiers). I really have the honor to have you agree to review this work; I appreciate your time and efforts to evaluate this thesis. Besides, I would like to thank **Pr. Abdelhafid BRIMA** (Professor, University of Batna 2) for the acceptance of our invitation to participate in this work.

This research project was funded by Ministry of Higher Education and Scientific Research of Algeria under “*Programme National Exceptionnel, P.N.E 2016-2017*” and by **Pr. Christian MASSON** from the ETS school. I am very grateful to them, without them, I had never been able to finalize my thesis.

Also, I would like to express my sincere appreciation to **Pr. J. Gerard SCHEPERS** and **Pr. Koen BOORSMA** from the Energy Research Center of the Netherlands (ECN) and **Pr. Niels N. SØRENSEN** from the Technical University of Denmark (DTU), for their support, encouragement, assistance and their important recommendations. The data used in this thesis were supplied by the consortium which carried out the EU FP5 project called MEXICO (Model rotor EXperiments In COntrolled conditions) to which nine European partners contributed.

All the numerical simulations were made on the supercomputer called GUILLIMIN managed by Calcul Québec and Compute Canada. I would like to thank all members of GUILLIMIN team for the answer of our questions, their help and support.

Last but not least, an enormous thanks to all my colleagues at the ETS school, in particular to **Dr. Abdelouahab MOUHAMED-TAIFOUR**. I am grateful to him for his help and valuable recommendations.

I thank all those who helped me and supported me from near or far,

Thank you very much to all.

Abdelhamid

ملخص

يدور موضوع هذه الأطروحة على المحاكاة العددية للتدفق المضطرب حول شفرة توربينة الرياح ذات المحور الأفقي (HAWT) المثبتة في الظروف الصحراوية. للقيام بذلك، تم تطوير طريقة CFD 3D تعتمد على حل معادلات Navier-Stokes المتوسطة باستخدام إجراء رينولدز (RANS). يركز هذا العمل على جانبين. الجانب الأول هو دراسة قدرة مختلف نماذج الاضطراب RANS على التنبؤ بالأداء الديناميكي والسرعة في أعقاب HAWTs. والهدف الثاني هو دراسة تأثير الرمال على الأداء الهوائي لتوربينات الرياح المثبتة في البيئات الصحراوية اعتمادا على نهج Eulérienne-Lagrangienne. وقد أظهرت نتائج المحاكاة أن اختيار نموذج الاضطراب له تأثير كبير على دقة التنبؤات العددية، خصوصا عند سرعات الرياح العالية. كما أنه قد لوحظ أيضا أن وجود جزيئات الرمل يمكن أن يقلل بشكل كبير من الأداء الديناميكي الهوائي.

الكلمات المفتاحية: طاقة الرياح، تحليل الديناميكا الهوائية، محاكاة عددية، نماذج الاضطراب، نهج Eulérienne-Lagrangienne، تأثير الرمال.

Résumé

Le sujet de cette thèse porte sur la simulation numérique de l'écoulement turbulent autour d'une pale d'éolienne à axe horizontal (HAWT) installée en climat saharien. Pour ce faire, une méthode CFD 3D a été développée en se basant sur la résolution des équations de Navier-Stokes moyennées par la procédure de Reynolds (RANS). Ce travail de thèse porte sur deux volets. Le premier volet est d'étudier la capacité des différents modèles de turbulence de type RANS à prédire les performances aérodynamiques et la vitesse dans le sillage proche des HAWTs. Le deuxième volet est d'étudier les effets du sable sur les performances aérodynamiques des éoliennes installées en un environnement désertique en se basant sur une approche Eulérienne-Lagrangienne. Les résultats de simulation ont montré que le choix du modèle de turbulence a un effet important sur la précision des prédictions numériques, particulièrement pour des vitesses élevées du vent. Il a été également noté que la présence des particules de sable pourra réduire considérablement les performances aérodynamiques de l'éolienne.

Mots-clés: Énergie éolienne, Analyse aérodynamique, Simulation numérique, Modèles de turbulence, Approche Eulérienne-Lagrangienne, Effet de sable.

Abstract

The subject of this thesis deals with the numerical simulation of turbulent flow around a horizontal axis wind turbine (HAWT) blade installed in Saharan climate. To do this, a 3D CFD method was developed based on the resolution of the Reynolds averaged Navier-Stokes equations (RANS). This thesis work focuses on two parts. The first part is to study the ability of different RANS turbulence models to predict the aerodynamic performances and the velocity in the wake of HAWTs. The second part is to investigate the sand effects on the aerodynamic performance of wind turbines installed in a desert environment based on an Eulerian-Lagrangian approach. The results of the simulation showed that the choice of the turbulence model has a significant effect on the accuracy of numerical predictions, especially for high wind speeds. It was also noted that the presence of sand particles could significantly reduce the aerodynamic performance.

Keywords: Wind energy, Aerodynamic analysis, Numerical simulation, Turbulence models, Eulerian-Lagrangian approach, Sand effect.

Table of Contents

Acknowledgements	
Abstract	
Table of Contents	
Nomenclature	
List of Tables	
List of Figures	
INTRODUCTION	19
CHAPTER 1: MODERN WIND TURBINES AND AERODYNAMIC METHODS	24
1.1 Brief history of wind turbine	24
1.2 Types and classifications of wind turbines	24
1.2.1 Vertical axis wind turbines	25
1.2.2 Horizontal axis wind turbines	25
1.3 State of the art: Insights into aerodynamic methods	26
1.3.1 Blade Element Momentum methods (BEM)	27
1.3.1.1 BEM corrections models	28
1.3.1.2 Limitations of BEM methods	30
1.3.2 Vortex methods	31
1.3.2.1 Lifting Line/Surface vortex methods	31
1.3.2.2 Panel methods	33
1.3.3 Simplified rotor geometry CFD methods	33

TABLE OF CONTENTS

1.3.3.1	Actuator disk model (ADM)	34
1.3.3.2	Actuator line model (ALM)	34
1.3.3.3	Actuator surface model (ASM)	35
1.3.4	Full rotor geometry CFD methods	35
1.4	Literature review	36
1.4.1	Turbulence models	36
1.4.2	Multiphase flows	44
CHAPTER 2: GOVERNING EQUATIONS		46
2.1	Navier-Stokes equations	46
2.2	Turbulence modeling approaches	46
2.2.1	Large eddy simulation (LES)	47
2.2.2	Statistical approach	47
2.3	Reynolds averaged equations	48
2.3.1	Closure problem	48
2.3.2	Boussinesq hypothesis	48
2.4	The studied RANS models	49
2.4.1	One equation Spalart-Allmaras model	49
2.4.2	Two equations k - ϵ models	50
2.4.2.1	Standard k - ϵ model	50
2.4.2.2	RNG k - ϵ model	51
2.4.2.3	Realizable k - ϵ model	52
2.4.3	Two equations k - ω models	53
2.4.3.1	Standard k - ω model	53
2.4.3.2	BSL k - ω model	54
2.4.3.3	SST k - ω model	56
2.4.4	Transitional models	57
2.4.4.1	Three equations k - kl - ω model	57
2.4.4.2	Four equations γ - Re_θ model	60
2.4.5	Reynolds stresses models	63
2.5	Eulerian-Lagrangian approach	64
2.5.1	Particles motion equation	64
2.5.2	Drag force model	64
2.5.3	Modeling particles rotation	65
2.5.4	Other forces	65
CHAPTER 3: NUMERICAL METHOD		66
3.1	Selected wind turbine model	66

TABLE OF CONTENTS

3.1.1	New MEXICO measurements	67
3.1.2	MEXICO blade	68
3.2	Geometry design	69
3.3	Computational domain	70
3.4	Computational mesh	71
3.4.1	Mesh strategy	71
3.4.1	Prismatic layers	72
3.4.2	Mesh sensitivity test	74
3.4.3	Selected mesh information	75
3.5	Boundary conditions	77
3.5.1	Inlet	77
3.5.1.1	Velocity	77
3.5.1.2	Pressure	78
3.5.1.3	Turbulence quantities	78
3.5.2	Outlet	79
3.5.3	Near wall treatment	79
3.5.3.1	Velocity	79
3.5.3.2	Turbulence quantities	80
3.5.4	Periodic conditions	81
3.5.5	Symmetry	81
3.5.6	Interfaces	82
3.5.7	Moving Reference Frame (MRF)	82
3.6	Numerical resolution	83
3.6.1.1	Integration of particle motion equation	83
3.6.1.2	Coupling between phases	85
3.7	High Performance Computing (HPC)	86
CHAPTER 4: RESULTS AND DISCUSSION: COMPARISON BETWEEN DIFFERENT TURBULENCE MODELS		88
4.1	Operating conditions	88
4.2	Attached and separated flow	89
4.3	Pressure distribution	90
4.4	Flow visualisation	95
4.4.1	Flow path-lines	95
4.4.2	Pressure contours	95
4.5	Aerodynamic loads	97

TABLE OF CONTENTS

4.5.1	Normal force	97
4.5.2	Tangential force	98
4.6	Rotor performances	100
4.7	Wake behavior	104
4.7.1	Axial velocity profile	104
4.7.2	Radial velocity profile	105
CHAPTER 5: RESULTS AND DISCUSSION: IMPACT OF SAND PARTICLES ON THE HAWTS PERFORMANCE		113
5.1	Simplifying assumptions	113
5.2	Initial and boundary conditions	114
5.2.1	Particles volume fraction	114
5.2.2	Characteristics of the sand-air flow	114
5.2.3	Particles injection	115
5.2.4	Wall-Particle Reflection	116
5.3	Numerical setup	117
5.4	Impact of particles concentration	120
5.5	Impact of particles size	122
CONCLUSIONS AND FUTURE WORKS		125
Bibliography		129
Appendix A MEXICO blade geometry		147
Appendix B Numerical results of standard $k-\omega$ and $k-\omega$ BSL turbulence models		148

Nomenclature

ACRONYMS

ADM	Actuator Disk Model
ALM	Actuator Line Model
ASM	Actuator Surface Model
BEM	Blade Element Momentum
BSL	Baseline
CFD	Computational Fluid Dynamics
DNS	Direct Numerical Simulation
DPM	Discrete Phase Model
DU	Delf University
E-E	Eulerian- Eulerian
E-L	Eulerian-Lagrangian
EVM	Eddy Viscosity model
HAWT	Horizontal Axis Wind Turbine
LDA	Laser Doppler Anemometry
LES	Large Eddy Simulation
MEXICO	Model rotor EXperiments In COntrolled conditions
MRF	Multiple Reference Frame
NACA	National Advisory Committee for Aerodynamics
NREL	National Renewable Energy Laboratory
PIV	Particle Image Velocimetry
PRESTO	PREssure STaggering Option
RANS	Reynolds Averaged Navier-Stokes
RNG	Renormalized Group

NOMENCLATURE

RSM	Reynolds Stress Model
SGS	Sub-Grid Scale
SIMPLE	Semi-Implicit Method for Pressure Linked Equation
SIMPLEC	SIMPLE Consistent
SST	Shear Stress Transport
TSR	Tip Speed Ratio
VAWT	Vertical Axis Wind Turbine

GREEK LETTERS

$\bar{\alpha}_s$	Mean particles volume fraction (-)
α_s	Particles volume fraction (-)
δ_{ij}	Kronecker symbol
μ_t	Turbulent (eddy) viscosity (kg/m.s)
$\tilde{\nu}$	Modified kinematic viscosity for Spalart-Allmaras model (m ² /s)
ρ_p	Particles density (kg/m ³)
τ_{ij}	Viscous stress tensor
τ_w	Wall shear stress (N/m ²)
Δt	Time step (s)
η	Turbulence small scale (m)
Ω	Rotor rotational speed (rad/s)
γ	Intermittency (-)
μ	Molecular viscosity (kg/m.s)
ν	Molecular kinematic viscosity (m ² /s ²)
ρ	Fluid density (kg/m ³)
ω	Specific dissipation rate (1/s)
ϵ	Dissipation rate of kinetic energy (m ² /s ³)

LATIN LETTERS

c	Particles concentration (kg/m ³)
\bar{c}	Mean particles concentration (kg/m ³)
C_D	Drag coefficient (-)
C_f	Skin friction coefficient (-)
C_p	Pressure coefficient (-)
C_P	Power coefficient (-)
d_p	Particles diameter (m)
e_n	Coefficient of restitution (-)

NOMENCLATURE

F_N	Normal force (N/m)
F_T	Tangential force (N/m)
\vec{g}	Gravitational acceleration (m/s ²)
G	Production of turbulence
I	Turbulence intensity (%)
k	Turbulent kinetic energy (m ² /s ²)
k_L	Laminar kinetic energy (m ² /s ²)
L	Turbulence length scale (m)
\dot{m}_p	Particles mass flux (kg/s)
p	Pressure (N/m ²)
r	Local radius of the blade (m)
R	Blade radius (m)
Re	Reynolds number
Re_θ	Momentum-thickness Reynolds number
S	Strain-rate tensor
$T_{i,j}$	Reynolds stress tensor ($-\overline{\rho u'_i u'_j}$)
u	Fluid Velocity (m/s)
u_p	Particles velocity (m/s)
U_∞	Freestream wind speed (m/s)
U_τ	Friction velocity (m/s)
x, y, z	Cartesian coordinates (m)
y^+	Dimensionless wall distance (-)
Y	Destruction of turbulence

List of Tables

Table 1: Brief survey of turbulence models, solvers and configurations mostly used in recent years to study the flow around HAWT.....	41
Table 2: The different RANS turbulence models tested.....	49
Table 3: General information about MEXICO wind turbine model.....	68
Table 4: The three tested meshes.	74
Table 5: Mesh sensitivity study.	75
Table 6: Detail information for low Reynolds mesh.....	77
Table 7: Operating conditions of the New MEXICO measurements.....	89
Table 8: Thrust and power relative errors vs computational time per one CPU.	102
Table 9: Chord and twist distribution on the MEXICO blade.	147

List of Figures

Figure 1: The global energy demands with specific share of wind and renewable energies between 2006 and 2016 with projection to 2040. Reproduced from [3].	20
Figure 2: Different types of vertical axis wind turbines [13].	25
Figure 3: Characteristic curves of averaged power coefficient as a function of tip speed ratio for various wind turbines. Reproduced from [16].	26
Figure 4: Schematic of a wind turbine and the annular control volume.	28
Figure 5: An example of the stall delay phenomenon. Reproduced from [3, 86].	29
Figure 6: An example of the dynamic stall phenomenon. Reproduced from [98].	30
Figure 7: The lifting line method.	32
Figure 8: The lifting surface method [27].	32
Figure 9: Notations of panels on the blade, using sources σ , dipoles μ , and vortices Γ . Reproduced from [27, 123].	33
Figure 10: Concept of the actuator disk (AD), line (AL) and surface (AS) models [133].	34
Figure 11: Classification of aerodynamic methods.	36
Figure 12: Normal force coefficient on the 80% blade radius. Reproduced from Duque et al. [158].	37
Figure 13: Comparison of measured and computed shaft torques for the NREL Phase VI rotor. Reproduced from Sørensen et al. [54, 160].	37

LIST OF FIGURES

Figure 14: Prediction of the torque with various turbulence models. Reproduced from Benjanirat and Sankar [161].	38
Figure 15: Pressure coefficient distribution. Reproduced from Tachos et al. [162].	39
Figure 16: Mechanical power comparison. Reproduced from Lanzafame et al. [163].	39
Figure 17: Tangential forces comparison. Reproduced from Sørensen et al. [75].	40
Figure 18: Comparison between two methods for calculating the particle volume fraction. Reproduced from Kang et al. [174].	45
Figure 19: Distribution of sand impacts for different particle sizes. Reproduced from Paz et al. [170].	45
Figure 20: (a) The German Dutch wind tunnels (DNW), and (b) The MEXICO wind turbine model. Reproduced from [5].	67
Figure 21: MEXICO experiments: pressure sensors distribution and PIV sheet position with cameras. Reproduced from [4, 218].	68
Figure 22: (a) Twist/chord distribution along the blade span, and (b) The MEXICO blade airfoil configuration.	69
Figure 23: Aerofoil profiles of the blade in SolidWorks.	69
Figure 24: Three-dimensional geometry of the MEXICO blade model.	70
Figure 25: 3D computational domain and dimensions.	70
Figure 26: Cross-section of the computational domain.	71
Figure 27: The representative diagram of (left) overset grid, and (right) sliding mesh technique. Reproduced from [3, 219].	72
Figure 28: Section view of the mesh at 60 % of the blade span.	73
Figure 29: Details of the prismatic layers in proximity of the leading edge (left) and trailing edge (right).	73
Figure 30: Details of the mesh on the blade surface at (left) tip region and (right) root region.	74
Figure 31: Low Reynolds mesh sensitivity test, comparison of normal forces along the blade for ($U_{\infty} = 15$ m/s) using three mesh cases.	75
Figure 32: Distribution of y^+ at five blade sections for; (a) low Reynolds mesh and (b) high Reynolds mesh respectively.	76
Figure 33: Details of the mesh for high and low Reynolds models.	76
Figure 34: Boundary conditions.	77
Figure 35: Law of the wall and concept of the logarithmic wall function [176].	80
Figure 36: The periodic conditions.	81

LIST OF FIGURES

Figure 37: Stationary and Moving Reference Frame (MRF) [173].	83
Figure 38: Momentum Transfer between the discrete and continuous phases.	85
Figure 39: High performance computing Guillimin cluster [230].	87
Figure 40: Limiting streamlines on the suction side of the MEXICO blade showing the attached and separated flow for three studied cases.	89
Figure 41: Development of the vortex in the downstream behind the rotor.	90
Figure 42: Five spanwise sections of the MEXICO blade.	91
Figure 43: Comparison between CFD results and experimental pressure coefficient distributions at five spanwise sections, case 1 ($U_{\infty}=10$ m/s).	92
Figure 44: Comparison between CFD results and experimental pressure coefficient distributions at five spanwise sections, case 2 ($U_{\infty}=15$ m/s).	93
Figure 45: Comparison between CFD results and experimental pressure coefficient distributions at five spanwise sections, case 3 ($U_{\infty}=24$ m/s).	94
Figure 46: Pressure coefficient contours and streamlines at five span-wise sections normal to the blade surface.	96
Figure 47: Schematic of velocities and angle of attack on a blade airfoil.	96
Figure 48: Normal and tangential forces distribution along the blade for different free stream velocities.	99
Figure 49: Comparison between CFD, experimental and theoretical results of the distribution of power coefficient as a function of tip speed ratio.	101
Figure 50: The relative error based on the thrust for different turbulence models.	103
Figure 51: The relative error based on the power for different turbulence models.	103
Figure 52: An overview of the line positions in which the velocities were measured in the new MEXICO measurements; (this figure does not respect the actual dimensions).	104
Figure 53: Comparison of axial (U) radial (V) and tangential (W) velocities in the inboard ($y = 0.5$ m) and outboard ($y = 1.5$) traverses for $U_{\infty}=15$ m/s.	107
Figure 54: Comparison of axial (U) radial (V) and tangential (W) velocities at the outboard ($y = 1.5$ m) traverses for $U_{\infty}=10$ m/s and $U_{\infty}=24$ m/s respectively.	108
Figure 55: Comparison of axial (U) radial (V) and tangential (W) velocities at the upstream ($x = -0.3$ m) and downstream ($x = +0.3$ m) traverses for $U_{\infty}=10$ m/s.	109

LIST OF FIGURES

Figure 56: Comparison of axial (U) radial (V) and tangential (W) velocities at the upstream ($x = -0.3\text{ m}$) and downstream ($x = +0.3\text{ m}$) traverses for $U_\infty=15\text{ m/s}$	110
Figure 57: Comparison of axial (U) radial (V) and tangential (W) velocities at the upstream ($x = -0.3\text{ m}$) and downstream ($x = +0.3\text{ m}$) traverses for $U_\infty=24\text{ m/s}$	111
Figure 58: Velocity contours behind the blade, comparison of low and high Reynolds models for low wind speed ($U_\infty= 10\text{ m/s}$).....	112
Figure 59: Velocity contours behind the blade, comparison of low and high Reynolds models for high wind speed ($U_\infty= 24\text{ m/s}$).	112
Figure 60: Types of particles injections; (a) group injection, (b) 3D cone injection, (c) injection from a surface.....	116
Figure 61: Particles injection into the inlet surface of the computational domain... ..	116
Figure 62: Sketch of the reflection of sand particles on the blade surface.....	117
Figure 63: Trajectory of particles close to the blade and those far from the blade. .	118
Figure 64: Lagrangian tracking of sand particles around the blade.	119
Figure 65: Variation of the rotor torque as a function of particles concentration for different particles diameter.	121
Figure 66: Power loss as a function of particles concentration for different particles diameter.....	122
Figure 67: Distribution of the pressure coefficient at $r/R=0.25$ spanwise blade section for different particles diameter, for $\alpha s = 1.5 \times 10 - 3$	123
Figure 68: Power/Torque loss as a function of particles diameter for different mean particles volume fractions.	123
Figure 77: Comparison between different velocity components for different wind speeds.	148
Figure 78: Comparison between different velocity components for $U_\infty=10\text{ m/s}$	149
Figure 79: Comparison between different radial velocity components.	150
Figure 80: Comparison between simulated and measured pressure coefficient distributions using ten turbulence models, for $U_\infty= 10\text{ m/s}$	151
Figure 81: Comparison between simulated and measured pressure coefficient distributions using ten turbulence models, for $U_\infty= 15$ and 24 m/s	152

Introduction

Background

Energy is a fundamental input to economic activity. Modern energy services light up our homes and schools, fuel economic activity to produce and consume, provide comfort and mobility, pump water and contribute to health and well-being. Harnessing energy sources to replace manual and animal labour was the platform of the Industrial Revolution: a period of unprecedented economic and social development.

The 20th century witnessed large increases in the global population, economic output and fossil fuel consumption. The gains from growth have been impressive for many people. Yet these gains have taken a toll on a range of environmental systems where unsustainable practices have dominated [1]. Continuing deterioration of natural resources could stress the ability to meet the needs of a growing population and undermine economic activity. Green growth could meet this challenge. Green growth is about fostering economic growth and development while ensuring that natural assets continue to provide the ecosystem services on which our well-being relies. To do this it must catalyse investment and innovation which will underpin sustained growth and give rise to new economic opportunities.

The renewable resources include, but are not limited to, bioenergy, geothermal energy, hydropower, solar energy, ocean energy, and wind energy. According to the International Energy Agency's 2018 report [2], renewables saw the highest growth rate of any energy source (nuclear, gas, oil, coal, etc.) in 2017, meeting a quarter of global energy demand growth last year.

In 2017, the growth of wind power and solar PV was unprecedented; wind power accounted for the largest share of overall renewables growth, at 36%, followed by solar PV (27%), hydropower (22%) and bioenergy (12%) [2]. Figure 1 shows the installed generation capacity of the power sector between 2006 and 2015 with conservative projections to 2040 according to the International Renewable Energy Agency (IEA) [2]

and the Global Wind Energy Council (GWEC) statistics [1]. The wind and renewable capacities are represented by the primary axis, while the total by the secondary axis. Wind energy contributes greatly to the increasing penetration of renewables into electricity generation sector.

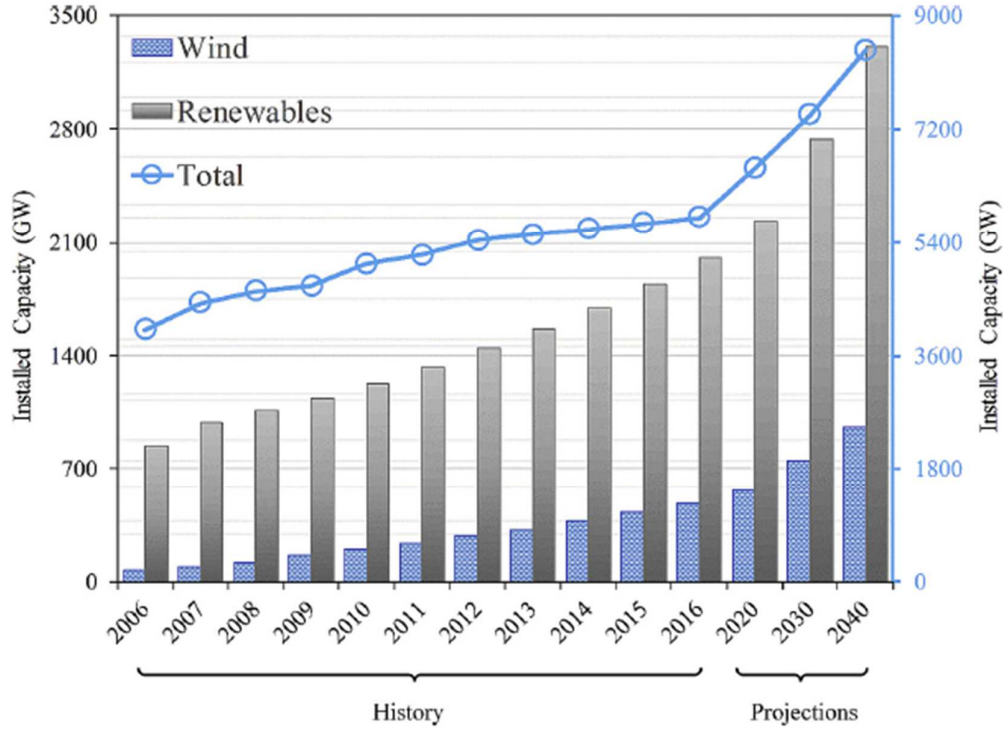


Figure 1: The global energy demands with specific share of wind and renewable energies between 2006 and 2016 with projection to 2040. Reproduced from [3].

It is well acknowledged that aerodynamics plays a very important role in the successful development of wind energy. The wind energy aerodynamics can be divided into two main areas: (i) rotor aerodynamics and (ii) wind farm aerodynamics [4]. Both areas are equally important. An improved understanding of the aerodynamic behavior over blades benefits the design of more efficient wind turbines [3], whereas the analysis of wake aerodynamics aims to enhance the power output of multiple turbines.

Motivations and objectives

First motivation

Aerodynamic methods using CFD with full rotor geometry are the most efficient and the most precise; however, such methods are quite complex due to the fact that these problems are described by the so-called Navier-Stokes equations, which cannot be

solved analytically: the fact that analytical solutions of the Navier-Stokes equations “only” demonstrate the existence of smooth solutions is, in fact, one of the seven Millennium Prize Problems [5]. A numerical solution for the Navier-Stokes equations for all time and length scales was also out of reach, due to the extreme demands it would make on computational resources. This remains true even on the most modern computer clusters. The modeling of turbulence is seen as a key element in CFD applications. Up until now, unfortunately, no single model exists that allows us to predict all the classes of physical phenomena linked to turbulence. The simplest turbulence models available in the literature are based on solving the Reynolds Averaged Navier-Stokes equations (RANS); these models are based on the resolution of the average flow field using additional transport equations to close the open system caused by additional unknowns in the equations produced by the Reynolds averaging process [6, 7]. Today there are many different turbulence models, and each model fits its own phenomenon and cannot serve for other phenomena. It is difficult to find a model that is advantageous over others for all conditions or cases. This is unsurprising, since the main objective of turbulence modeling is to attempt to approximate a highly complicated phenomenon [6]. Therefore, the first main contribution of this work is to evaluate the ability of different types of RANS turbulence models to predict the aerodynamic performance and the near wake behavior of HAWTs under different operating conditions.

Second motivation

Like other countries, Algeria has recently started using wind power to generate electricity, where the first wind farm was established for Algeria in a desert region located in the south, at Kaberten in the Wilaya of Adrar [8]. This wind farm consists of twelve large wind turbines. The rotor diameter of the installed wind turbines is 52 m and the height of the tower is 55 m. The power of each wind turbine is 850 kW (totaling 10.2 MW for the wind farm) [9]. It is evident that the available wind potential and the availability of large spaces are the most important criteria that led to the choice of this region than others. However, the sand wind characteristics of these desert areas may affect the performance of turbines and this leads us to ask an important question: how far the sand particles could affect the aerodynamic performance of wind turbines installed in Saharan zones ?. To our knowledge, until now the effect of the sand on aerodynamics, is not well known. Therefore, the second main objective of this work is to study the sand effects on the aerodynamic performance of HAWTs.

Thesis objectives

The main objective of this work is to give some answers to two important questions:

- (i) To what extent can the choice of turbulence model affect the numerical prediction accuracy of the flows around HAWTs ?
- (ii) How far the sand particles could affect the aerodynamic performance of wind turbines installed in desert regions ?

Thesis structure

To achieve the purposes of this research project, the thesis has been divided into five chapters organized as follows:

Chapter 1. In the first chapter, we will present a general overview of wind turbines and a quick review of the most commonly used aerodynamic methods for studying numerically the wind turbine rotors. Then, the literature review and the state of the current research on the topic will be presented. This research focuses on two different parts: (i) the most used RANS turbulence models for simulating the flows around HAWTs and (ii) some applications of air-sand flows.

Chapter 2. In the second chapter, the mathematical model for the fluid and for the particles will be presented. The ten turbulence models used in this study to close the RANS equations and its main differences will be briefly discussed.

Chapter 3. The objective of the third chapter is to present the numerical methodology used in this thesis. In the beginning, the general information of the used wind turbine model and the measurements will be presented. Then, the different CFD steps and the algorithms of resolutions used in this work will be presented and discussed.

Chapter 4. In the fourth chapter, we will present and discuss the obtained numerical results from the comparison of turbulence models. The numerical CFD results will be analyzed with respect to the different aerodynamic properties: the pressure at different spanwise sections of the blade, the aerodynamic forces (normal and tangential), the torque, the thrusts and the mechanical power. The comparison also includes different components of velocities in the near wake.

Chapter 5. The objective of the fifth chapter is to present the numerical results obtained from the multiphasic E-L model. In the beginning of this chapter, we will

INTRODUCTION

present the initial and boundary conditions. Then, the general influence of sand particles on the aerodynamic performance of the wind turbines will be discussed.

Finally, the main conclusions found in this study and the main recommendations relevant to the future work will ultimately be addressed towards the end of this thesis.

Chapter 1

Modern wind turbines and aerodynamic methods

1.1 Brief history of wind turbine

The use of wind as a form of energy dates from 5000 B.C. in Egypt where people navigated the Nile River on sail boats powered by wind. Windmills were first utilised in China then in the Middle East for food processing by the 11th century. Then, Europeans imported this technology to do mechanical work [10]. With the advent of the Industrial Era, windmills continued to be used and towards the end of the 19th century first experiments took place in USA and in Denmark to generate electricity from wind. Afterwards, years of low interest in wind energy began and lasted till the oil crisis in the 1970's, which caused many countries to seek new forms of energy source [11]. Nowadays wind power is a fully active contributor to electricity production and as reported in the reference [12] in the last two decades there have been tremendous advances in the energy efficiency of wind turbines. In fact, a 2006 wind turbine would produce 180 times more electricity than one at the same location installed 20 years before and at half the cost per kilowatt-hour (kWh).

1.2 Types and classifications of wind turbines

Wind turbine, by definition, is the device to convert kinetic energy in wind into useful mechanical power which can be utilized to generate electricity. There are two types of wind turbine system, differentiated by the outward appearance of the blades: vertical-axis wind turbines (VAWT) and horizontal-axis wind turbines (HAWT).

1.2.1 Vertical axis wind turbines

Vertical axis windmills and the subsequent vertical axis wind turbines seem to be older than those with an horizontal axis of rotation. The VAWT can be classified into drag-driven Savonius rotors and lift-driven Darrieus turbines [3]. The straight-bladed H-rotor is a special type of the Darrieus turbine (Figure 2). One of the big advantages of VAWTs is the independence of directional change in wind. In addition, heavy components can be installed close to the ground.

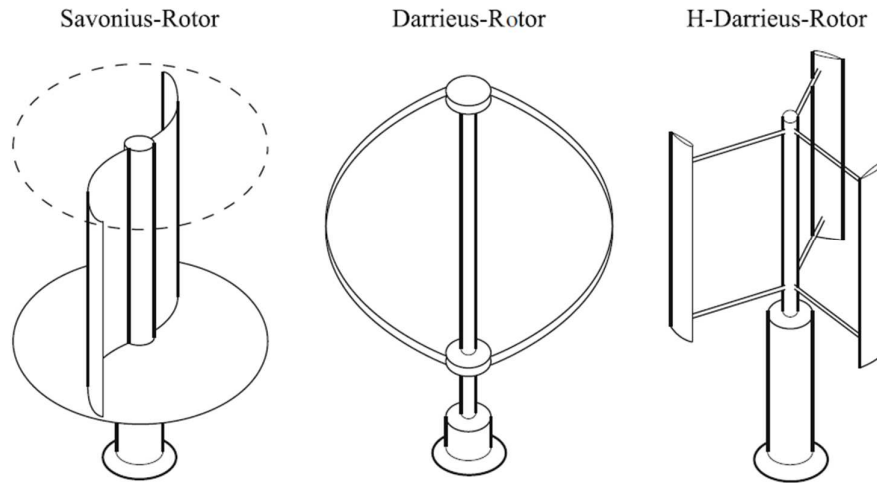


Figure 2: Different types of vertical axis wind turbines [13].

1.2.2 Horizontal axis wind turbines

Generally, more of the wind energy can be captured from HAWT blades than from VAWT blades due to the fact that the entire area swept by HAWT blades always faces in to the wind during operations.

HAWTs are classified according to the diameter of the blade as follows: micro-scale (μ SWT, diameter ≤ 0.1 m), small-scale (SSWT, 0.1 m $<$ diameter ≤ 1 m), mid-scale (MSWT, 1 m $<$ diameter ≤ 5 m), and large-scale (LSWT, diameter > 5 m) [14, 15]. Large-scale HAWTs are installed either as wind farms or in offshore areas. Small-scale HAWTs are commonly seen in residential areas.

To acquire a better insight into different wind turbines concepts, the power performance and operating range for different types of wind turbines are shown in Figure 3.

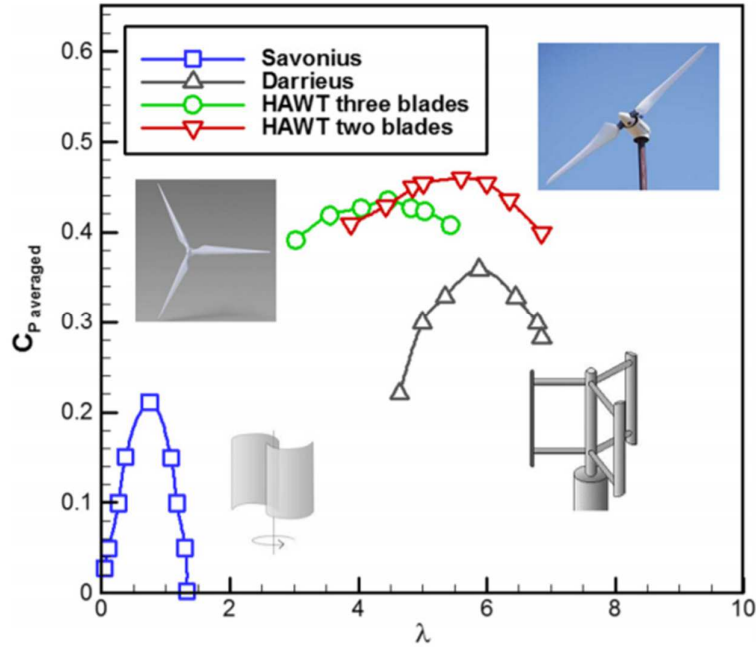


Figure 3: Characteristic curves of averaged power coefficient as a function of tip speed ratio for various wind turbines. Reproduced from [16].

1.3 State of the art: Insights into aerodynamic methods

From an outsider's point of view, aerodynamics of wind turbines may seem simple as compared to, e.g., fixed-wing aircrafts or helicopters. However, the inflow is always subject to stochastic wind fields and for machines that are not pitch-regulated, stall is an intrinsic part of the operational envelope [17]. Stall refers to the phenomenon that the airflow separates from the suction face of the blade and features turbulent mixing and flow reversal close to the surface. This makes an adequate description very complicated. Indeed, in spite of the wind turbine being one of the oldest devices for exploiting the energy of the wind, some of the most basic aerodynamic mechanisms are not yet fully understood.

The first performance predictions of wind turbine rotors, using simple axial momentum and energy considerations, have been achieved in the first decades of the 20th century. The result obtained by Betz [18] in 1920 is famous, and known as Betz limit: no more than 59% of the kinetic energy contained in a stream tube having the same cross section as the disc area can be converted to useful work by the disc. However, Betz was not the only one to derive this result. Bergy [19] found that in 1915, Lanchester was the first to establish the maximum efficiency of a wind turbine rotor and the ideal performance of a hovering helicopter rotor or static propeller. Betz and Lanchester

belonged to two leading aerodynamic research schools in the beginning of the previous century: the German school led by Prandtl, and the British school led by Lanchester himself. Later, a study of early Russian rotor aerodynamic papers revealed that Joukowsky [20] derived the Betz limit in the same year as Betz did: 1920 [21].

Glauert [22] in 1935 developed the 1D momentum theory into a more general theory, which is commonly known as the Blade Element Momentum (BEM) theory. This theory, later extended with many “engineering rules”, is today the basis for all rotor design codes in use by industry.

In order to study wind turbine rotor aerodynamics, one needs to be able to model the rotor under both its operating conditions and its interactions with the wind, and this to a certain degree of accuracy. Today, several methods exist, we can classify them as suggested by Sørensen and his team [23-29] as follows:

- Blade element momentum methods (BEM) [22, 30-36] ;
- Vortex methods: lifting line/lifting surface/panel method [37-42] ;
- Simplified rotor geometry CFD methods: actuator disc (ADM)/actuator line (ALM)/ actuator surface (ASM) [23, 43-52];
- Full rotor geometry CFD methods (Full Navier-Stokes) [53-78].

1.3.1 Blade Element Momentum methods (BEM)

In the BEM method, the rotor is modelled as a series of blade elements, and an iterative process is used to obtain a balance between the forces on the blade elements and the forces on the flow field determines various parameters like the total power, rotor thrust, blade loads, etc.

The BEM theory operates on two fundamental assumptions: that there is no radial dependency, and that forces can be averaged over the individual annuli. Figure 4 shows a schematic of an annulus at a radial location r with thickness dr around a three bladed wind turbine. According to the assumptions, the forces and velocities inside this annular element are not influenced by any other annular element and therefore a wind turbine can be divided into N number of concentric annuli and forces in each annulus can be calculated independently. By the second assumption, the average force on the flow field in the annulus is equal to the sum of the forces on the individual blade

elements. Based on these two assumptions, the idea is to find a balance between the force exerted on the flow field by the blade elements, and the change in the momentum of the fluid between the locations far upstream and far downstream of the rotor [24].

BEM has been developed using software or simple engineering codes for designing and analyzing the performance of HAWT blades [22, 30-36, 79]. Indeed, all modern aeroelastic design codes are based on the BEM theory owing to its simplicity.

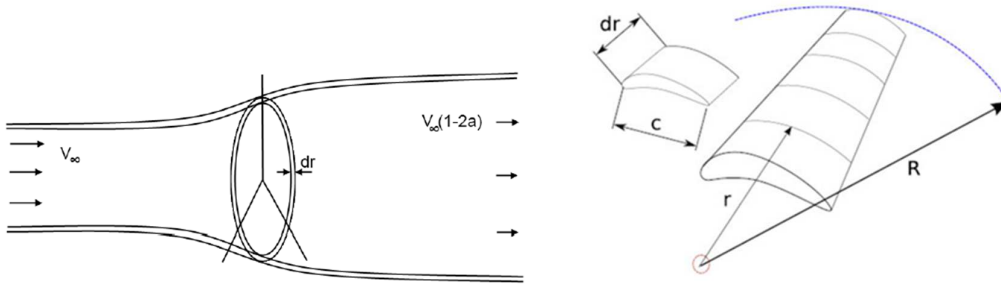


Figure 4: Schematic of a wind turbine and the annular control volume.

1.3.1.1 BEM corrections models

Since the classical BEM theory is adapted under ideal assumptions that lead to certain limitations [14]: (i) incompressible flow; (ii) stationary flow; (iii) ideal fluid: lack of viscous effects; (iv) infinite number of blades; (v) uniform thrust on the surface swept by the rotor; (vi) stable wake: missing the blade rotation effects. Several efforts have been made in order to correct for the aerodynamic effects, which present on a real turbine that are not modeled in the classical BEM method.

(i) Tip loss factors models

For simplicity, the wind turbine rotor is assumed to be an actuator disc of infinite number of blades in the classical BEM theory. As a result, modelling a real rotor with finite number of blades introduces an error in the loads estimated in the tip region. To correct for these effects, tip loss correction factors are used, e.g., see [22, 80-84].

(ii) Stall delay models

The accuracy of BEM performance prediction codes is dependent on the input airfoil characteristics, namely, the lift coefficient (C_l) and drag coefficient (C_d). These airfoil characteristics are typically based on 2D wind-tunnel measurements that are known to

normally underpredict peak power by 10% to 30% as well as the associated blade flapwise bending moment. Experimentally measured airfoil characteristics on rotating blades have found them to be substantially altered over the inboard portion of the blade by 3D effects due to rotation. These effects result in airfoil maximum lift coefficients ($C_{l,max}$) much larger than 2D measurements [85].

Figure 5 shows the lift coefficient as a function of angle of attack (AOA) derived from NREL measurements at the 30% radial location for the wind speed of 25 m/s, and the static data comes from DUT wind tunnel tests at the same condition [3, 24, 86]. It can be seen from this figure that the airfoil stalls at around 15° at 2D static condition and the lift coefficient reaches a maximum of 1.05. However, for the rotating blade, the phenomenon of C_l stall does not happen at such angle, but is delayed to 24.6° and the lift coefficient is then enlarged to 2.1.

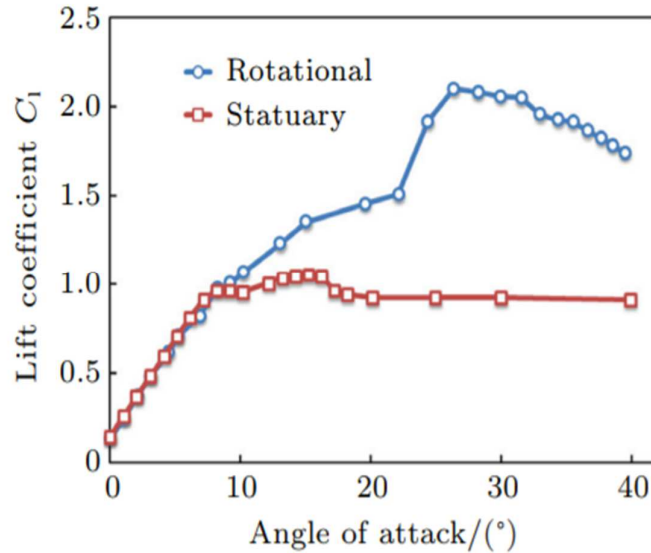


Figure 5: An example of the stall delay phenomenon. Reproduced from [3, 86].

The increase in $C_{l,max}$ has been attributed to centrifugal pumping which is modified by a Coriolis displacement in the chordwise direction. Blade rotation results in centrifugal-induced outward radial flow in the separated flow region. The radial flow due to rotation develops in the presence of an adverse velocity gradient where the flow is strongly retarded. To improve the accuracy of the classical BEM, several stall delay empirical models have been proposed, such as Snel model [87], Du & Selig model [88, 89], Chaviaropoulos & Hansen model [90], Lindenbug model [91], Dumitrescu & Cardos model [92, 93] and Bak et al model [94].

(iii) **Dynamic stall models**

When an airfoil undergoes an unsteady change in its angle of attack, a phenomenon known as dynamic stall occurs, where the airfoil temporarily experiences lift coefficients that are significantly different than its 2D values [24]. This can happen due to unsteady effects such as yawed flow, inflow turbulence, wind shear, etc.

For convenience, dynamic stall is often studied under periodic pitching conditions [95-98]. Figure 6 shows an example case where an airfoil undergoes a sinusoidal pitching motion with a mean angle of attack of 10° and a pitching amplitude of 6° . The physical mechanism that underlies dynamic stall is complicated and has been described in various texts in detail, e.g., [99-102].

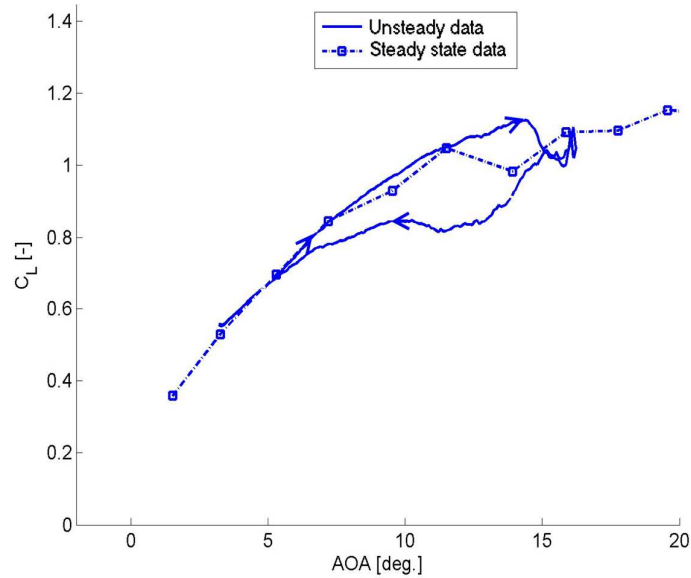


Figure 6: An example of the dynamic stall phenomenon. Reproduced from [98].

Various dynamic stall models exist which can be used with BEM codes, such as Gross & Harris model [103], Tarzanin model [104], Tran & Petot model [105], Leishman & Beddoes model [106], Øye model [107] and Hnasen model [108].

1.3.1.2 Limitations of BEM methods

The momentum models are featured by its fast calculation and low fidelity, and remain predominant in engineering design. However, they are expected to be discontinued in the wind turbine aerodynamics primarily due to the following reasons [3].

First, the use of the BEM is restricted by its empiricism. The engineering correction models incorporated into the BEM method greatly expand its applicability and enhance its accuracy. However, they were all developed at specific operating conditions. The BEM method is unable to accurately predict loads at off-design conditions [109]. The uncertainty of the BEM is approximately 20% for blade loads which should be further improved.

Secondly, the lack of reliable airfoil data is deemed responsible for most unfavorable behaviors of the BEM method. The values of C_l and C_d are a function of AOA and Reynolds number. They are usually collected in wind tunnel experiments for stationary aerofoils at low AOAs before stall conditions. Yet a rotating wind turbine, has higher AOAs. The data for post-stall conditions are conventionally extrapolated using empirical correlations [110, 111]. A recent study showed that these empirically extrapolated data resulted in incorrect power predictions at high AOAs [112].

Three-dimensional (3D) inviscid aerodynamic models (vortex methods) have been developed in an attempt to obtain a more detailed description of the 3D flow that develops around a wind turbine.

1.3.2 Vortex methods

In vortex models the rotor blades, trailing and shed vorticity in the wake are represented by lifting lines or surfaces [27]. On the blades, the vortex strength is determined from the bound circulation that stems from the amount of lift created locally by the flow past the blades. The trailing wake is generated by the spanwise variation of the bound circulation while the shed wake is generated by a temporal variation and ensures that the total circulation over each section along the blade remains constant in time. Knowing the strength and position of the vortices the induced velocity can be found in any point using the Biot–Savart law [113].

1.3.2.1 Lifting Line/Surface vortex methods

In some models (namely the lifting line models) the bound circulation is found from airfoil data table-look up just as in the BEM method [114]. The inflow is determined as the sum of the induced velocity, the blade velocity and the undisturbed wind velocity (Figure 7). The relationship between the bound circulation and the lift is denoted as the Kutta–Joukowski theorem.

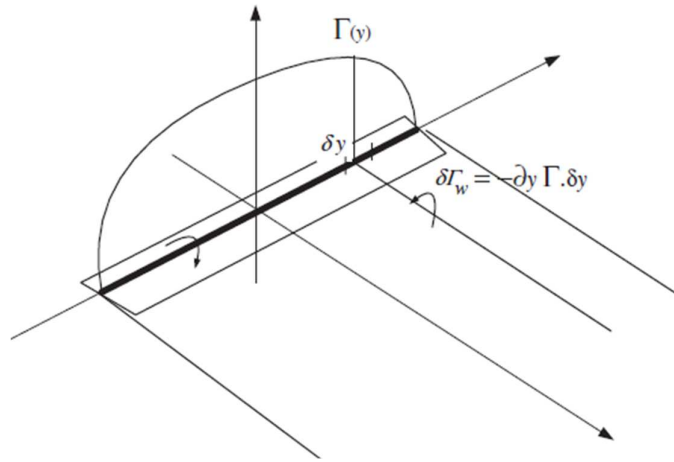


Figure 7: The lifting line method.

In lifting line/surface vortex models, the wake structure can either be prescribed or computed as a part of the overall solution procedure [115-117]. In a prescribed vortex technique, the position of the vortical elements is specified from measurements or semi-empirical rules. This makes the technique fast to use on a computer, but limits its range of application to more or less well known steady flow situations. For unsteady flow situations and complicated wake structures, free wake analysis become necessary [118-120]. A free wake method is more straightforward to understand and use, as the vortex elements are allowed to convect and deform freely under the action of the velocity field. The advantage of the method lies in its ability to calculate general flow cases, such as yawed wake structures and dynamic inflow. The disadvantage, on the other hand, is that the method is far more computing expensive than the prescribed wake method.

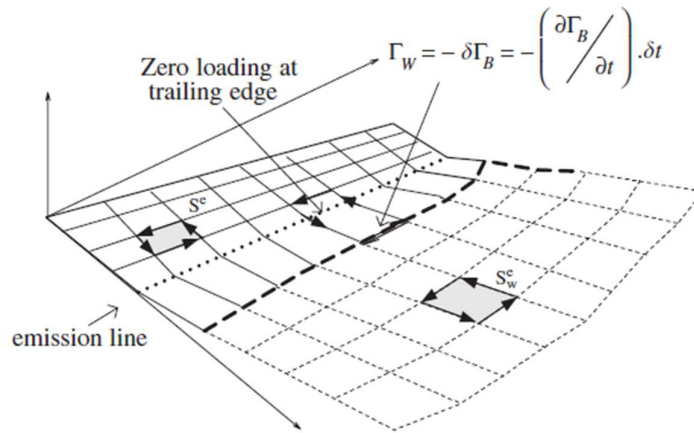


Figure 8: The lifting surface method [27].

1.3.2.2 Panel methods

In the panel model, the inviscid and incompressible flow past the blades themselves can be found by applying a surface distribution of sources and dipoles (see Figure 9). The background is Green’s theorem [121], which allows obtaining an integral representation of any potential flow field in terms of the singularity distribution. The free wake panel method that represents the real blade geometry is the most versatile and precise vortex model. It can analyze the pressure distribution and dynamic stall mechanism apart from the functions of the momentum theory [122, 123].

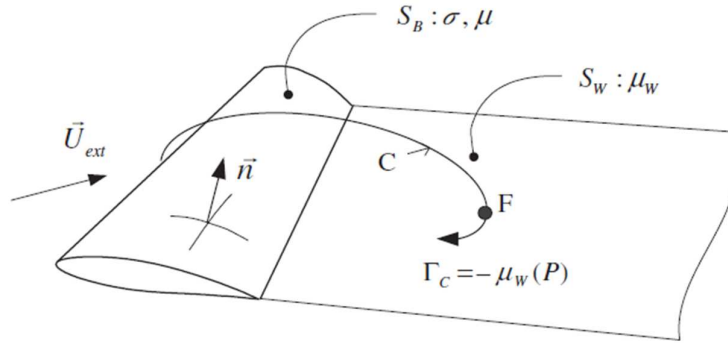


Figure 9: Notations of panels on the blade, using sources σ , dipoles μ , and vortices Γ .
 Reproduced from [27, 123].

Vortex methods have been applied on wind turbine rotors particularly in order to better understand wake dynamics [124-126]. It has been shown that the vortex model provides more physics of rotor aerodynamics than the BEM using boundary layer corrections [125, 127], and it is also valid over a wider range of turbine operating conditions [27, 128]. However, the exclusion of viscous effect is a problem of the potential flow models. This issue may be alleviated by some viscous-inviscid interaction methods [129, 130]. However, they are still immature [27] and restricted to mild flow separation [3].

1.3.3 Simplified rotor geometry CFD methods

The actuator disc model is probably the oldest analytical tool for analysing rotor performance. In this model, the rotor is represented by a permeable disc that allows the flow to pass through the rotor, at the same time as it is subject to the influence of the surface forces. The “classical” actuator disc model is based on conservation of mass, momentum and energy, and constitutes the main ingredient in the 1D momentum theory, as originally formulated by Rankine [131] and Froude [132]. Combining it with

a blade-element analysis, we end up with the celebrated Blade-Element Momentum Technique. In its general form, however, the actuator disc might as well be combined with the Euler or Navier-Stokes equations.

Within the force approach a set of different methods exists, namely the actuator disk method (ADM), the actuator line method (ALM) and the actuator surface method (ASM), which will be discussed in the upcoming sections.

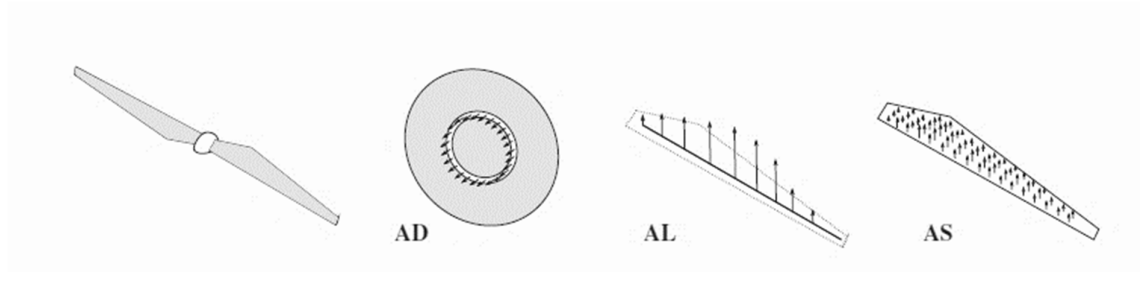


Figure 10: Concept of the actuator disk (AD), line (AL) and surface (AS) models [133].

1.3.3.1 Actuator disk model (ADM)

The ADM simulates the turbine as a disc within the flow that imposes forces on the fluid. Many versions of the ADM exist. Some apply thrust and tangential forces [134] while others only apply thrust [135]. Many researchers have adopted the ADM for simulating wind turbines [43-46]. Even though the ADM may simulate the turbines and their wakes, it does not create the tip vortices that are carried onto the wake.

The ADM provided reasonable overall results [45, 133, 136]. However, there are still many things to improve. For example, the forces imposed on the fluid were averaged through the rotor whereas the actual forces acted only in the instantaneous location of the blades. The ADM was not able to capture tip vortices, which are important when studying the near wake of a wind turbine [137]. With these limitations, researchers have devised other models which improve the results provided by the ADM.

1.3.3.2 Actuator line model (ALM)

As an extension of the non-uniformly loaded actuator disk approach, Sørensen and Shen [138] introduced the actuator line approach (ALM). This approach models the wind turbine blades as a set of blade elements along each blade axis [137]. This model combines a 3-D Navier-Stokes solver with a technique in which body forces are distributed radially along each of the rotor blades. Thus, the kinematics of the wake is

determined by a full 3-D Navier-Stokes simulation whereas the influence of the rotating blades on the flow field is included using tabulated aerofoil data to represent the loading on each blade.

The ALM yielded accurate results [23, 51, 139-143] but it still had limitations [137]. Each blade-element force was the total force over that element, whereas the real forces were distributed smoothly over the chord of the blade-element. To distribute the blade element point force, a Gaussian projection was used [139], which eliminated numerical instabilities but did not reproduce the actual force distribution on the blades.

1.3.3.3 Actuator surface model (ASM)

Another model that has been explored recently is the ASM [50]. This model calculates the forces on a 2-D airfoil as a function of the chord, thus avoiding one of the major simplifications of the ALM. This is done by using empirical formulas with forces as a function of the chord position [48, 144]. The model's main advantage is its ability to provide a more realistic force distribution [137]. The limitation of the ASM is its dependency on an external calculation for the force distribution as a function of position within the chord of an airfoil.

1.3.4 Full rotor geometry CFD methods

The first applications of CFD (using full geometry) to wings and rotor configurations were studied back in the late seventies and early eighties in connection with airplane wings and helicopter rotors [145-148] using potential flow solvers. To overcome some of the limitations of potential flow solvers, a shift towards unsteady Euler solvers were seen through the eighties [149-151]. When computing power allowed the solution of full Reynolds Averaged Navier-Stokes equations, the first helicopter rotor computations including viscous effects were published in the late eighties and early nineties [152-155].

The complete or direct modeling of the rotor by constructing a body-fitted grid is physically the most sound method to compute the flow around a turbine [133]. This approach has potential to provide a consistent and physically realistic simulation of the turbine flow field. Using this approach, flow characteristics can be obtained directly by avoiding any kind of restrictions: neither in the flow equations, nor in the modeling of the rotor itself [53-78]. Due to its high accuracy, the direct modeling approach can replace experimental studies [3, 14, 86, 133]. The disadvantage, however, is that this method is far more computing expensive than other methods, see Figure 11.

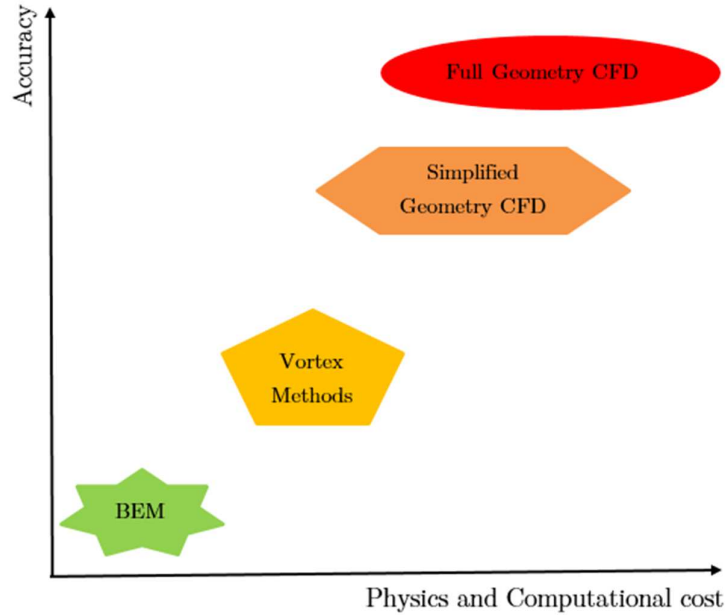


Figure 11: Classification of aerodynamic methods.

1.4 Literature review

1.4.1 Turbulence models

It is well known, that the Navier-Stokes equations cannot be directly solved for any of the cases of practical interest to wind turbines, and that some kind of turbulence modelling are needed. The standard approach to derive turbulence models is by time averaging the Navier-Stokes equations, resulting in the so-called Reynolds Averaged Navier-Stokes equations (RANS). Several different RANS models have been used for wind turbine applications.

The first simulations (for wind turbine applications) with direct modeling were done by Sørensen and Hansen [156, 157], employing a rotating reference frame and the $k-\omega$ SST model. The rotor power is predicted well for wind speeds below 10 m/s, but at higher speeds, the power is underpredicted. The strongly separated flow on the blade is not correctly captured at these speeds, which the authors attribute to insufficient mesh resolution and limitations of the turbulence model.

Duque et al. [158] used the compressible thin-layer Navier–Stokes equations with the Baldwin-Lomax (algebraic) turbulence model [159]. A comparison with the NREL

phase II rotor showed good agreement of the pressure distributions, but the rotor-tower interaction was not predicted well (see Figure 12).

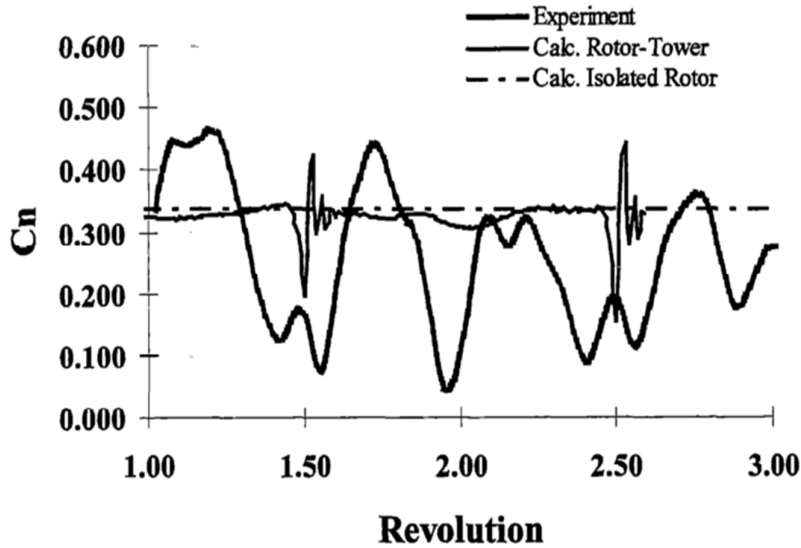


Figure 12: Normal force coefficient on the 80% blade radius. Reproduced from Duque et al. [158].

Sørensen et al. [54, 160] performed simulations for the NREL phase VI rotor under different wind speeds with $k-\omega$ SST turbulence model using two computational domain: namely tunnel and free configurations. Good results have been found, especially for the pressure distribution. However, it has been shown that the torque curve is underpredicted by more than 20% at high wind speeds (see Figure 13).

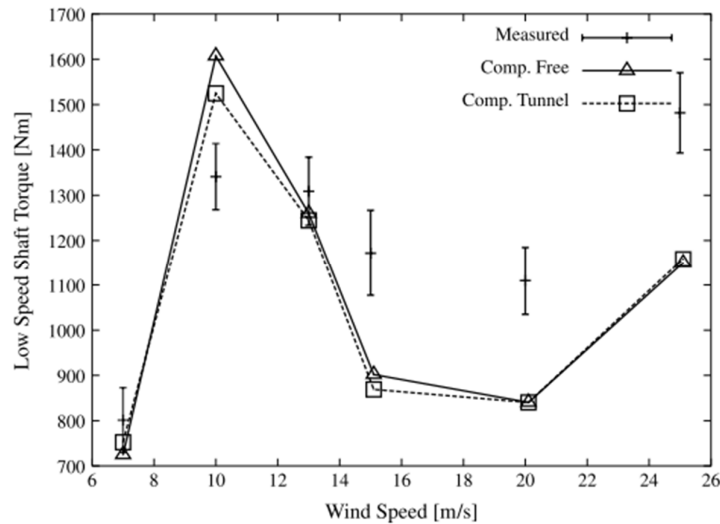


Figure 13: Comparison of measured and computed shaft torques for the NREL Phase VI rotor. Reproduced from Sørensen et al. [54, 160].

Benjanirat and Sankar [161] used an overset grid model to study the effect of different turbulence models: the Baldwin-Lomax, the Spalart-Allmaras and the standard $k-\epsilon$. All the models predicted the out-of-plane forces and associated bending moments well, but difficulties were found in predicting the in-plane forces and therefore in predicting power generation (Figure 14). This can probably be explained by the fact that lift prediction is less sensitive to turbulence modeling than drag prediction [133].

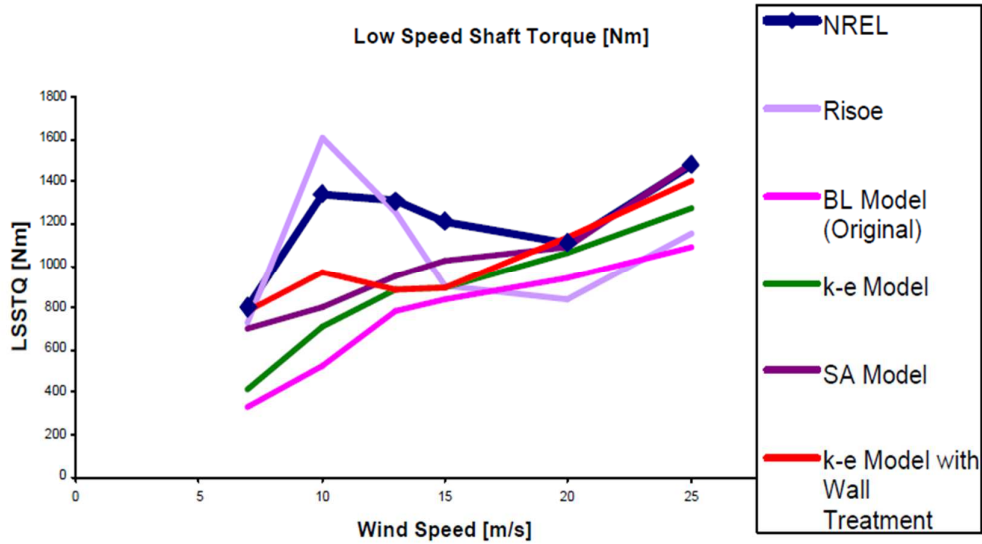


Figure 14: Prediction of the torque with various turbulence models. Reproduced from Benjanirat and Sankar [161].

Tachos et al. [162] explored the effectiveness four RANS models: the Spalart-Allmaras, the standard $k-\epsilon$, the $k-\epsilon$ RNG and the $k-\omega$ SST (Figure 15). They found that even at relatively low wind speeds the predictions of these models strongly deviated from the NREL data.

From experiments it is known that laminar/turbulent transition influences the flow over rotor blades for some cases [27]. It has been demonstrated for 2D applications, that transition models can greatly improve the accuracy for cases where transition phenomena are important. Even though nearly all rotor studies so far have been computed assuming fully turbulent conditions, it is generally accepted that it is important to include laminar/turbulent transition in RANS models. Predicting transition in 3D is a much more complex task than dealing with 2D, and 3D transition is an active research field. The effects of the transition have been investigated in the literature by some researchers.

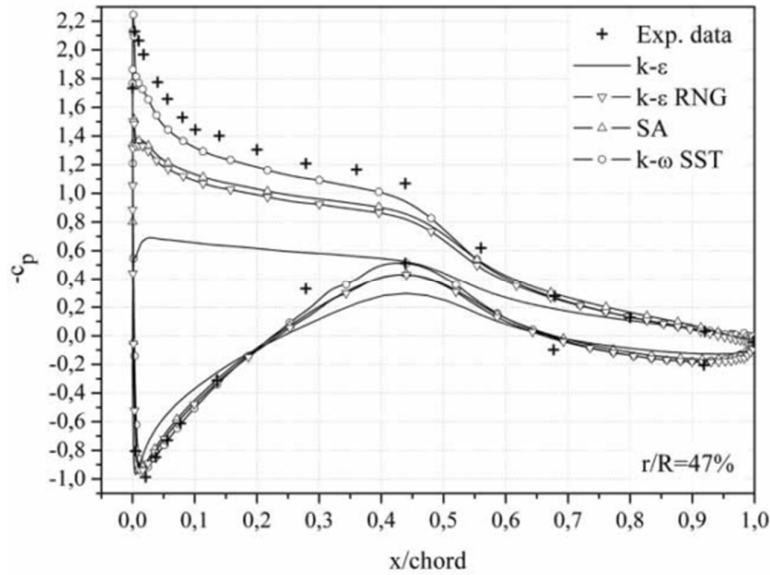


Figure 15: Pressure coefficient distribution. Reproduced from Tachos et al. [162].

Lanzafame et al. [163] investigated the effect of transition using γ_{Re_θ} model. It has been found that while the fully turbulent SST $k-\omega$ presents inaccuracy in the incipient stall region, the transitional γ_{Re_θ} model accurately follows the experimental data trend. The relative error is less than 5% for all wind speeds except for very high wind speeds where an underestimation of nearly 6% occurs (see Figure 16).

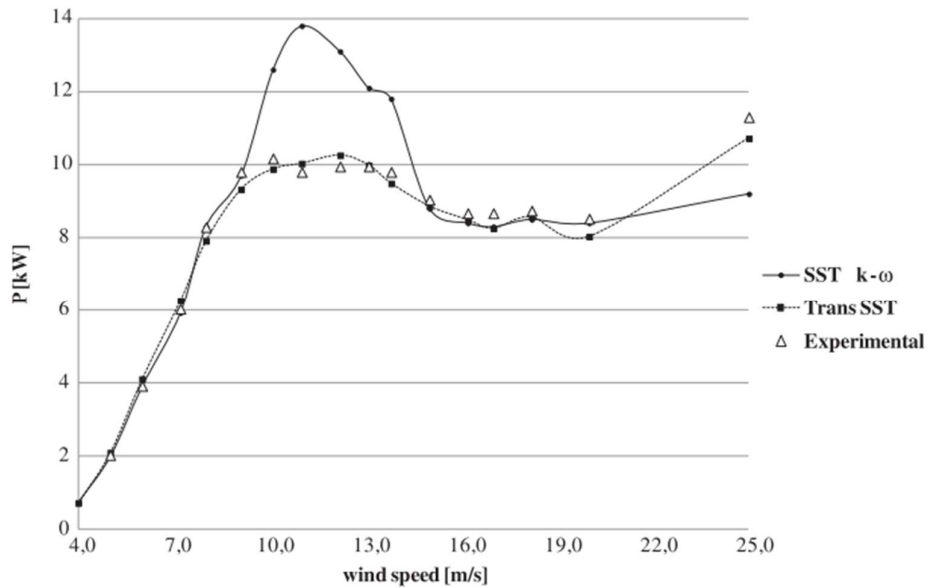


Figure 16: Mechanical power comparison. Reproduced from Lanzafame et al. [163].

Recently, Sørensen et al. [75] simulated the flow around the MEXICO wind turbine rotor using two turbulence models: the fully turbulent $k-\omega$ SST and the transitional $k-\omega$ SST. The transition was modeled using the so-called E^n method [164]. They found that the difference is very minor between the fully turbulent and transitional results (Figure 17).

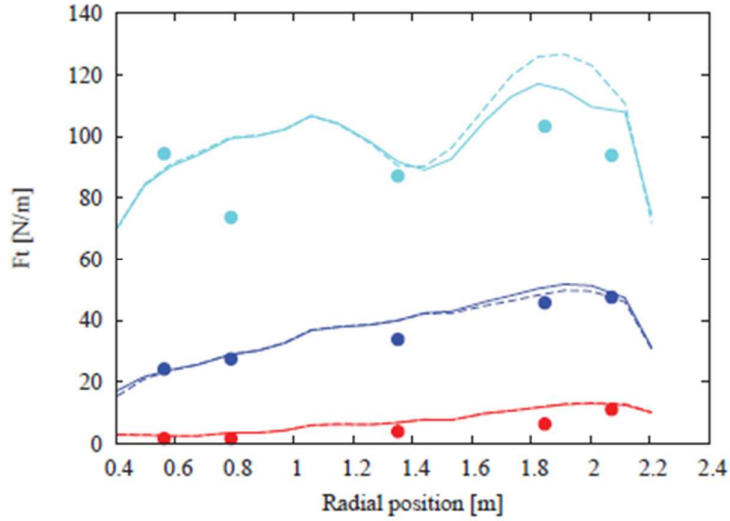


Figure 17: Tangential forces comparison. Reproduced from Sørensen et al. [75].

Table 1 shows a brief survey of turbulence models, solvers and configurations mostly used in recent years to study the flow around HAWTs.

Table 1: Brief survey of turbulence models, solvers and configurations mostly used in recent years to study the flow around HAWT.

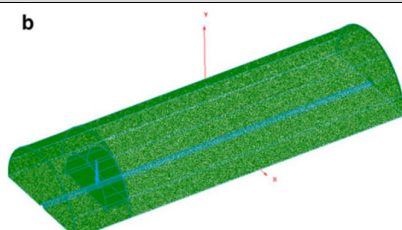
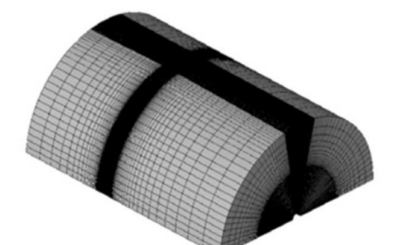
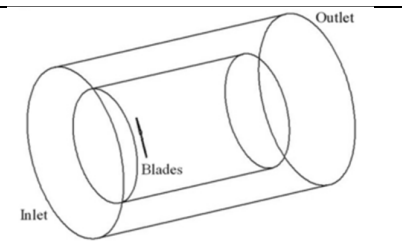
Authors/year	Rotor Model	Outer Domain Dimensions	Rotating Domain Dimensions	Turbulence Model	CFD Solver	Configuration
Tadamasa and Zangeneh. 2011 [55]	NREL phase VI $r^{(1)}=5.029\text{m}$	$DL^{(2)}=10xr$ $UL^{(3)}=2xr$ $R^{(5)}=2xr$	$L^{(4)}=0.5 \times r$ $R^{(5)}=1.25 \times r$	SST $k-w$	ANSYS CFX 11.0	
Yu et al. 2011 [56]	NREL phase VI $r=5.029\text{m}$	$DL=3xr$ $UL=2xr$ $R=2xr$	All domain rotating	SST $k-w$	ANSYS Fluent	
Moshfeghi et al. 2012 [57]	NREL phase VI $r=5.029\text{m}$	$DL=10xr$ $UL=4xr$ $R=4.8xr$	$L=4.6 \times r$ $R=3.2 \times r$	SST $k-w$	ANSYS CFX 11.0	

Table 1: Continued

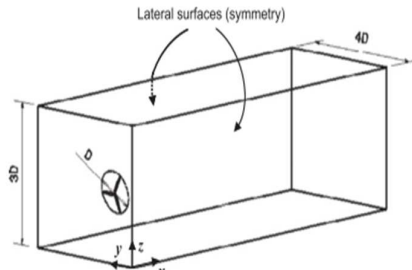
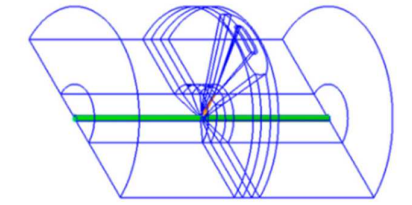
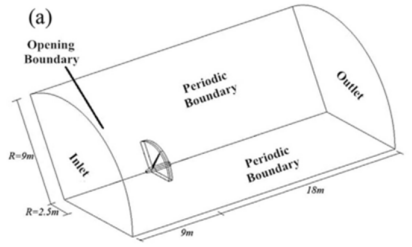
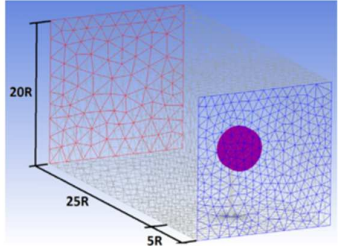
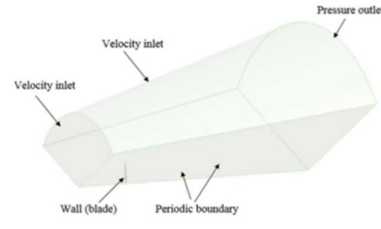
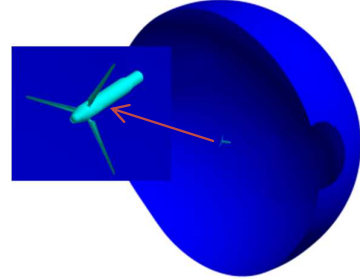
Authors/year	Rotor Model	Outer Domain Dimensions	Rotating Domain Dimensions	Turbulence Model	CFD Solver	Configuration
AbdelSalam et al. 2014 [61]	Danwin 180 kW r=11.6m	DL=50xr UL=4xr H= 6xr W=8xr	R =1.25×r L= 0.5×r	standard $k - \epsilon$	<i>Fluent 6.3</i>	
Elfarra et al. 2014 [62]	NREL phase VI r=5.029m	DL =5xr UL=5xr R=3.5xr	R =3.5×r L= 1×r	Lauder–Sharma $k - \epsilon$	<i>NUMECA</i>	
Yang et al. 2014 [35]	MEXICO r=2.25m	DL=8xr UL=4xr R=4xr	R=1.25×r L= 0.25×r	SST $k - w$	<i>ANSYS CFX 14.0</i>	

Table 1: Continued

Authors/year	Rotor Model	Outer Domain Dimensions	Rotating Domain Dimensions	Turbulence Model	CFD Solver	Configuration
Plaza et al. 2015 [68]	MEXICO r=2.25m	DL =25xr UL =5xr H= 20xr W= 20xr	R = 1.375×r L= 0.5×r	SST $k-w$	ANSYS FLUENT 14.50	
Wang et al. 2015 [77]	NREL WindPACT 1.5MW r=35m	DL=10xr RD ⁽⁸⁾ = 6.85xr UL = 2.57xr RU ⁽⁹⁾ =3.42xr	All domain rotating	SST $k-w$	ANSYS FLUENT 13.0	
Sørensen et al. 2016 [75]	MEXICO r=2.25m	Spherical domain with diameter of 10xr in all directions	All domain rotating	SST $k-w$	EllipSys3D	

⁽¹⁾r=Radii of the Rotor; ⁽²⁾DL=Downstream Length; ⁽³⁾UL=Upstream Length; ⁽⁴⁾L=Length; ⁽⁵⁾R=Radii; ⁽⁶⁾H=height; ⁽⁷⁾W=width; ⁽⁸⁾DR= Downstream Radii; ⁽⁹⁾UR= Upstream Radii.

1.4.2 Multiphase flows

To our knowledge, no reference data are available in the field of particle impacts in aerodynamics. The existing studies investigate the penalties caused on airfoils by heavy rain (because of the liquid film) [165] or the effect of dust on wind turbines (because of increasing roughness) [166].

From the point of view of computational fluid dynamics (CFD) simulations, two different strategies are generally accepted as the most suitable to evaluate the multiphase flows (gas-solid). On the one hand, the Eulerian–Eulerian (E–E) approach [167] treats both phases as continuous flows interpenetrating each other. On the other hand, the Eulerian–Lagrangian (E–L) approach [168, 169] solves the fluid flow using Navier–Stokes equations, and the solid particles are injected into the flow and are then tracked individually to calculate their trajectories inside the gas [165]. This strategy offers a more comprehensive picture of the particle flow interaction but requires more powerful computational resources [170].

The comparison between these two approaches was performed by Adamczyk et al. [171] for modeling the sand particle transport phenomena in small-scale circulating fluidized beds, and by Zhang and Chen [172] for simulating particles transport in enclosed spaces. It has been shown that the E–L approach is considered appropriate for this purpose because the discrete volume fraction is much lower than 10% and the computational resources are sufficiently powerful [170, 173].

In order to calculate the volume fraction of the sand in the fluid phase, two different methods exist: (i) using the volumes of fluid-solid, or (ii) using the sand mass flux. These two methods have been evaluated experimentally by Kang et al. [174]. It has been confirmed that these two methods give similar results, see Figure 18.

The multiphase flow model used in this thesis is the DPM model (Discrete Phase Model) which is an E-L model implemented in the ANSYS Fluent. This model has been widely used in the literature for simulating the air-sand flows. The most applied applications using this kind of problem were performed for predicting the erosion in the solid body surfaces due to the sand impact.

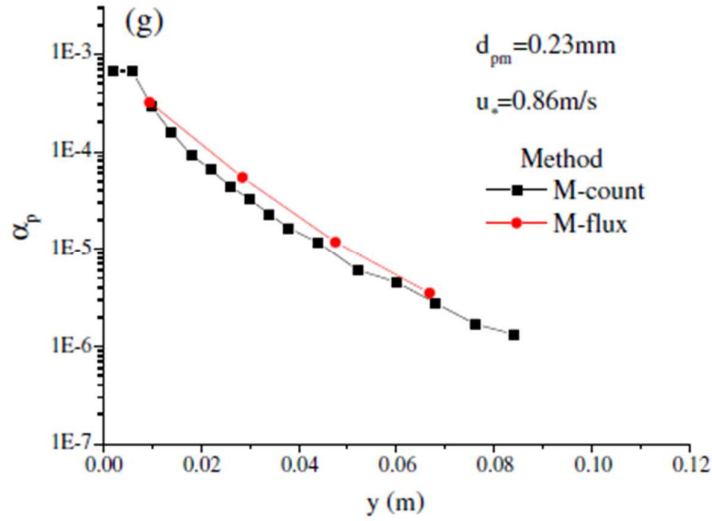


Figure 18: Comparison between two methods for calculating the particle volume fraction. Reproduced from Kang et al. [174].

Mansouri et al. [175] used the DPM model to study the erosion of a 90° sharp bend in water–sand slurry flow. Two different sand types were used: sharp silica sand (25 μm) and rounded quartz (256 μm). Two RANS models were employed for resolving the near wall region: standard wall-function and low-Reynolds number approach. The numerical results showed that adequately resolving the near wall region and employing the low-Reynolds number model can significantly improve the prediction. The DPM model has also been used by Paz et al. [170] to evaluate the effect of particle impacts on the motion of high-speed trains in a sand-laden flow. A drag force reduction of 10% for each 0.2 decrease in the coefficient of restitution was noted.

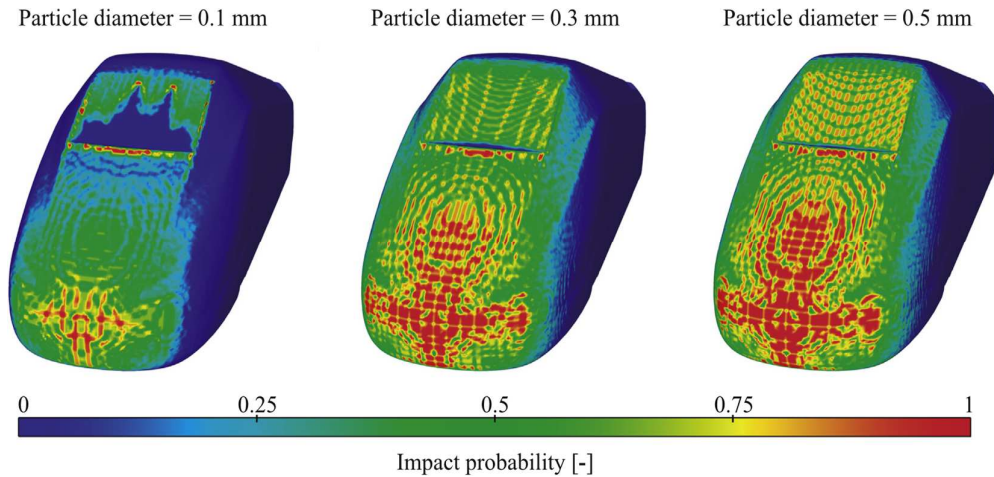


Figure 19: Distribution of sand impacts for different particle sizes. Reproduced from Paz et al. [170].

Chapter 2

Governing equations

2.1 Navier-Stokes equations

For an incompressible flow, the continuity and the momentum equations are respectively given by:

$$\frac{\partial u_i}{\partial x_i} = 0 \quad (1)$$

$$\rho \frac{\partial u_i}{\partial t} + \rho u_j \frac{\partial u_i}{\partial x_j} = -\frac{\partial p}{\partial x_i} + \frac{\partial}{\partial x_j}(\tau_{ij}) \quad (2)$$

where u_i denotes the i^{th} velocity component, p is the pressure, ρ is the fluid density and τ_{ij} is viscous stress tensor. For Newtonian fluid, it can be defined as:

$$\tau_{ij} = 2\mu s_{ij} \quad (3)$$

where μ is the molecular viscosity and s_{ij} is the strain-rate tensor defined as:

$$s_{ij} = \frac{1}{2} \left(\frac{\partial u_i}{\partial x_j} + \frac{\partial u_j}{\partial x_i} \right) \quad (4)$$

2.2 Turbulence modeling approaches

Turbulent flows are characterized by fluctuating velocity fields. These fluctuations mix transported quantities such as momentum, energy, and species concentration, and cause the transported quantities to fluctuate as well. Since these fluctuations can be of small scale and high frequency, they are too computationally expensive to simulate

directly in practical engineering calculations. Instead, the instantaneous (exact) governing equations can be time-averaged, ensemble-averaged, or otherwise manipulated to remove the small scales, resulting in a modified set of equations that are computationally less expensive to solve. However, the modified equations contain additional unknown variables, and turbulence models are needed to determine these variables in terms of known quantities [176].

2.2.1 Large eddy simulation (LES)

Large eddy simulation (LES) provides an alternative approach in which the large eddies are calculated in a time-dependent simulation that uses a set of “filtered” equations. Filtering is essentially a manipulation of the exact Navier-Stokes equations to remove only the eddies that are smaller than the size of the filter, which is usually taken as the mesh size. The idea was derived from Kolmogorov's theory [177, 178], which assumes that the large eddies of the flow are dependant on the geometry while the smaller scales are more universal. The filtering process creates additional unknown terms that must be modeled in order to achieve closure. Statistics of the mean flow quantities, which are generally of most engineering interest, are gathered during the time-dependent simulation. The attraction of LES is that, by modeling less of the turbulence (and solving more), the error induced by the turbulence model will be reduced. Different sub-grid scale models are available in the literature, such as Smagorinsky model [179], Algebraic Dynamic model [180], Localized Dynamic model [181], WALE (Wall-Adapting Local Eddy-viscosity) model [182] and Dynamic Global-Coefficient model [183].

In contrast to RANS, where the computational cost is only weakly dependent on Re , the computational cost of LES scales roughly with Re^2 [184]. Near solid boundaries, where boundary layers are present, LES is extremely expensive because it requires refinement in three directions, whereas RANS only requires refinement in the direction normal to the wall.

2.2.2 Statistical approach

Because turbulence consists of random fluctuations of the various flow properties, the statistical approach can be used. This approach is mainly based on the procedure introduced by Reynolds [185], in which all quantities are expressed as the sum of mean and fluctuating quantities [186]. The Reynolds-averaged Navier-Stokes (RANS) equations represent transport equations for the mean flow quantities only, with all the

scales of the turbulence being modeled. The approach of permitting a solution for the mean flow variables greatly reduces the computational effort. Therefore, this approach is currently the most commonly used CFD approach.

2.3 Reynolds averaged equations

For an incompressible flow, the RANS equations can be written as:

$$\frac{\partial \bar{u}_i}{\partial x_i} = 0 \quad (5)$$

$$\rho \frac{\partial \bar{u}_i}{\partial t} + \rho \bar{u}_j \frac{\partial \bar{u}_i}{\partial x_j} = -\frac{\partial p}{\partial x_i} + \frac{\partial}{\partial x_j} (\bar{\tau}_{ij} - \overline{\rho u'_i u'_j}) \quad (6)$$

$$\bar{\tau}_{ij} = 2\mu \bar{s}_{ij} \quad (7)$$

$$\bar{s}_{ij} = \frac{1}{2} \left(\frac{\partial \bar{u}_i}{\partial x_j} + \frac{\partial \bar{u}_j}{\partial x_i} \right) \quad (8)$$

Equation (6) is usually referred to as the Reynolds-Averaged Navier-Stokes equation. The quantity $(-\overline{\rho u'_i u'_j})$ is known as the Reynolds-stress tensor, we denote it by T_{ij} , thus:

$$T_{ij} = -\overline{\rho u'_i u'_j} \quad (9)$$

2.3.1 Closure problem

Because T_{ij} is a symmetric tensor ($T_{ij} = T_{ji}$), it has six independent components. Hence, six unknown quantities have been produced as a result of Reynolds averaging. However, no additional equations were gained. The system of equations is not yet closed. To close the system, additional equations are needed.

2.3.2 Boussinesq hypothesis

To model the Reynolds stresses in terms of mean flow quantities, the Boussinesq hypothesis [187, 188] is commonly used. This hypothesis assumes that the Reynolds stress is related linearly to the mean strain-rate tensor as in a laminar flow. The proportional factor is the eddy viscosity. The Boussinesq hypothesis for an incompressible flow can be written as [189]:

$$T_{ij} = 2\mu_t \bar{s}_{ij} - \frac{1}{2} \rho k \delta_{ij} \quad (10)$$

where μ_t is the eddy viscosity, δ_{ij} is the Kronecker symbol and k is the turbulent kinetic energy defined as:

$$k = \frac{1}{2} (\overline{u'_i u'_i}) \quad (11)$$

2.4 The studied RANS models

In this work, ten different RANS models, grouped in Table 2, were tested. Their main features will be briefly described in the following subsections.

Table 2: The different RANS turbulence models tested.

Closing approach	Near-wall resolution type	Turbulence model	Developed by	Transports equations number
Eddy-Viscosity Models (EVM)	High Reynolds	Spalart-Allmaras	Spalart and Almaras [190]	1
		Standard $k-\epsilon$	Launder and Spalding [191]	2
		$k-\epsilon$ RNG	Yakhot and Orszag [192]	2
		$k-\epsilon$ Realizable	Shih et al. [193]	2
	Low Reynolds	Standard $k-\omega$	Wilcox [186]	2
		$k-\omega$ BSL	Menter [194]	2
		$k-\omega$ SST	Menter [194]	2
		$k-\text{kl}-\omega$	Walters and Cokljat [195]	3
	$\gamma-Re_\theta$	Langtry and Menter [196]	4	
Reynolds stress Models (RSM)	High Reynolds	<i>RSM-LPS</i>	Gibson and Launder [197] Launder et al. [198-200]	7

2.4.1 One equation Spalart-Allmaras model

The Spalart-Allmaras model [190] is a one-equation model that solves a modeled transport equation for the kinematic eddy (turbulent) viscosity. The Spalart-Allmaras model was designed specifically for aerospace applications involving wall-bounded flows and has been shown to give good results for boundary layers subjected to adverse pressure gradients.

In the Spalart-Allmaras model, the turbulent viscosity is calculated by:

$$\mu_t = \rho \tilde{\nu} f_{v1} \quad (12)$$

where the viscous damping function f_{v1} is given by:

$$f_{\nu 1} = \frac{\chi^3}{\chi^3 + C_{\nu 1}^3} \quad (13)$$

and

$$\chi = \frac{\tilde{\nu}}{\nu} \quad (14)$$

where ν is the molecular kinematic viscosity.

The variable $\tilde{\nu}$ is given by:

$$\frac{\partial}{\partial t}(\rho\tilde{\nu}) + \frac{\partial}{\partial x_i}(\rho\tilde{\nu}u_i) = G_\nu + \frac{1}{\sigma_{\tilde{\nu}}} \left[\frac{\partial}{\partial x_i} \left\{ (\mu + \rho\tilde{\nu}) \frac{\partial \tilde{\nu}}{\partial x_j} \right\} + G_{b2}\rho \left(\frac{\partial \tilde{\nu}}{\partial x_j} \right)^2 \right] - Y_\nu \quad (15)$$

The production term G_ν is modeled as:

$$G_\nu = C_{b1}\rho\tilde{\nu} \left(S + \frac{\tilde{\nu}}{\kappa^2 d^2} f_{\nu 2} \right) \quad (16)$$

$$f_{\nu 2} = 1 - \frac{\chi}{1 + \chi f_{\nu 1}} \quad (17)$$

where d is the distance from the wall and S is a scalar measure of the deformation tensor defined as:

$$S = \sqrt{2\Omega_{ij}\Omega_{ij}} \quad (18)$$

where Ω_{ij} is mean rate of rotation tensor defined as:

$$\Omega_{ij} = \frac{1}{2} \left(\frac{\partial u_i}{\partial x_j} - \frac{\partial u_j}{\partial x_i} \right) \quad (19)$$

The destruction term Y_ν is modeled as:

$$Y_\nu = C_{w1}\rho[r + C_{w2}(r^6 - r)] \left[\frac{1 + C_{w3}^6}{[r + C_{w2}(r^6 - r)]^6 + C_{w3}^6} \right]^{1/6} \left(\frac{\tilde{\nu}}{d} \right)^2 \quad (20)$$

$$r = \frac{\tilde{\nu}}{(S\kappa^2 d^2 + \tilde{\nu} f_{\nu 2})} \quad (21)$$

The model constants are [190]:

$$C_{b1} = 0.1335, C_{b2} = 0.622, \sigma_{\tilde{\nu}} = \frac{2}{3}, C_{\nu 1} = 7.1, C_{w1} = 3.1945 \quad (22)$$

$$C_{w2} = 0.3, C_{w3} = 2.0, \kappa = 0.4187$$

2.4.2 Two equations k - ϵ models

2.4.2.1 Standard k - ϵ model

The standard k - ϵ model [191] is the most widely used turbulence model in the CFD community due to its simplicity and robustness. This model involves transport equations for the turbulent kinetic energy (k) and its dissipation rate (ϵ).

In the standard k - ϵ model, the turbulent (or eddy) viscosity is calculated by combining k and ϵ as follows:

$$\mu_t = \rho C_\mu \frac{k^2}{\epsilon} \quad (23)$$

The turbulent kinetic energy k and its dissipation rate ϵ are obtained from the following transport equations:

$$\frac{\partial(\rho k)}{\partial t} + \frac{\partial(\rho k u_i)}{\partial x_i} = \frac{\partial}{\partial x_j} \left[\left(\mu + \frac{\mu_t}{\sigma_k} \right) \frac{\partial k}{\partial x_j} \right] + G_k - \rho \epsilon \quad (24)$$

and

$$\frac{\partial(\rho \epsilon)}{\partial t} + \frac{\partial(\rho \epsilon u_i)}{\partial x_i} = \frac{\partial}{\partial x_j} \left[\left(\mu + \frac{\mu_t}{\sigma_\epsilon} \right) \frac{\partial \epsilon}{\partial x_j} \right] + C_{1\epsilon} \frac{\epsilon}{k} G_k - C_{2\epsilon} \rho \frac{\epsilon^2}{k} \quad (25)$$

The production of turbulent kinetic energy G_k is modeled as:

$$G_k = -\overline{\rho u'_i u'_j} \frac{\partial u_j}{\partial x_i} \quad (26)$$

where the model constants are [191]:

$$C_{1\epsilon} = 1.44, C_{2\epsilon} = 1.92, C_\mu = 0.09, \sigma_k = 1.0, \sigma_\epsilon = 1.3 \quad (27)$$

As the strengths and weaknesses of the standard k - ϵ model have become known, modifications have been introduced to improve its performance. Two of these variants have been tested in this work: the RNG k - ϵ model and the realizable k - ϵ model.

2.4.2.2 RNG k - ϵ model

The RNG k - ϵ model [201] was derived using a statistical technique called renormalization group theory [192]. It is similar in form to the standard k - ϵ model, but includes the following refinements:

- (i) The RNG model has an additional term in its ϵ equation that improves the accuracy for rapidly strained flows.

- (ii) The effect of swirl on turbulence is included in the RNG model, enhancing accuracy for swirling flows.
- (iii) The RNG theory provides an analytical formula for turbulent Prandtl numbers, while the standard k - ϵ model uses constant values.

These features make the RNG k - ϵ model more accurate and reliable for a wider class of flows than the standard k - ϵ model [176].

In the RNG k - ϵ model, the transport equation for ϵ is given by:

$$\frac{\partial(\rho\epsilon)}{\partial t} + \frac{\partial(\rho\epsilon u_i)}{\partial x_i} = \frac{\partial}{\partial x_j} \left[\left(\mu + \frac{\mu_t}{\sigma_\epsilon} \right) \frac{\partial \epsilon}{\partial x_j} \right] + C_{1\epsilon} \frac{\epsilon}{k} G_k - C_{2\epsilon}^* \rho \frac{\epsilon^2}{k} \quad (28)$$

where

$$C_{2\epsilon}^* = C_{2\epsilon} + \frac{C_\mu \eta^3 (1 - \eta/\eta_0)}{1 + \beta \eta^3} \quad (29)$$

$$\eta = k(2S_{ij}S_{ij})^{1/2}/\epsilon \quad (30)$$

The constants of the model are [176, 201]:

$$C_{1\epsilon} = 1.42, C_{2\epsilon} = 1.68, \sigma_k = \sigma_\epsilon = 1.393, \eta_0 = 4.38, \beta = 0.012 \quad (31)$$

2.4.2.3 Realizable k - ϵ model

The realizable k - ϵ model [193] differs from the standard k - ϵ model in two important ways:

- (i) The realizable k - ϵ model contains an alternative formulation for the turbulent viscosity.
- (ii) A modified transport equation for the dissipation rate ϵ has been derived from an exact equation for the transport of the mean-square vorticity fluctuation.

In the realizable k - ϵ model, the eddy viscosity factor C_μ is computed by:

$$C_\mu = \frac{1}{A_0 + A_s \frac{kU^*}{\epsilon}} \quad (32)$$

where

$$U^* = \sqrt{S_{ij}S_{ij} + \tilde{\Omega}_{ij}\tilde{\Omega}_{ij}} \quad (33)$$

and

$$\tilde{\Omega}_{ij} = \Omega_{ij} - 2\epsilon_{ijk}w_k \quad (34)$$

$$\Omega_{ij} = \bar{\Omega}_{ij} - 2\epsilon_{ijk}w_k \quad (35)$$

The model constants are:

$$A_0 = 4.04, A_s = \sqrt{6} \cos(\phi), \phi = \frac{1}{3} \cos^{-1}(\sqrt{6}W), W = \frac{S_{ij}S_{jk}S_{ki}}{\tilde{S}^3}, \tilde{S} = \sqrt{S_{ij}S_{ij}} \quad (36)$$

2.4.3 Two equations k - ω models

2.4.3.1 Standard k - ω model

The standard k - ω model [6, 202] is an empirical model based on model transport equations for the turbulent kinetic energy (k) and the specific dissipation rate (ω), which can also be thought of as the ratio of ϵ to k .

In the standard k - ω model, the turbulent viscosity is computed as follows:

$$\mu_t = \alpha^* \frac{\rho k}{\omega} \quad (37)$$

The coefficient α^* is given by:

$$\alpha^* = \frac{\alpha_0^* + Re_t/R_k}{1 + Re_t/R_k} \quad (38)$$

where

$$Re_t = \frac{\rho k}{\mu \omega} \quad (39)$$

The turbulence kinetic energy k and the specific dissipation rate ω are obtained from the following transport equations:

$$\frac{\partial(\rho k)}{\partial t} + \frac{\partial(\rho k u_i)}{\partial x_i} = \frac{\partial}{\partial x_j} \left[\left(\mu + \frac{\mu_t}{\sigma_k} \right) \frac{\partial k}{\partial x_j} \right] + G_k - Y_k \quad (40)$$

and

$$\frac{\partial(\rho \omega)}{\partial t} + \frac{\partial(\rho \omega u_i)}{\partial x_i} = \frac{\partial}{\partial x_j} \left[\left(\mu + \frac{\mu_t}{\sigma_\omega} \right) \frac{\partial \omega}{\partial x_j} \right] + C_\omega - Y_\omega \quad (41)$$

The production of ω is given by:

$$C_\omega = \frac{\alpha\omega}{k} G_k \quad (42)$$

where

$$\alpha = \frac{\alpha_\infty}{\alpha^*} \left(\frac{\alpha_0 + Re_t/R_w}{1 + Re_t/R_w} \right) \quad (43)$$

The dissipation of k is given by:

$$Y_k = \rho\beta^* f_{\beta^*} k\omega \quad (44)$$

where

$$f_{\beta^*} = \left\{ \begin{array}{ll} 1 & \chi_k \leq 0 \\ \frac{1 + 680\chi_k^2}{1 + 400\chi_k^2} & \chi_k > 0 \end{array} \right\} \quad (45)$$

and

$$\chi_k \equiv \frac{1}{\omega^3} \frac{\partial k}{\partial x_j} \frac{\partial \omega}{\partial x_j} \quad (46)$$

$$\beta^* = \beta_\infty^* \left(\frac{4/15 + (Re_t/R_\beta)^4}{1 + (Re_t/R_\beta)^4} \right) \quad (47)$$

The dissipation of ω is given by:

$$Y_\omega = \rho\beta_i f_\beta \omega^2 \quad (48)$$

where

$$f_\beta = \frac{1 + 70\chi_\omega}{1 + 80\chi_\omega}, \chi_\omega = \left| \frac{\Omega_{ij}\Omega_{ik}S_{ki}}{(\beta_\infty^*\omega)^3} \right| \quad (49)$$

The constants of the standard k - ω model are:

$$\alpha_\infty = 0.52, \alpha_0 = \frac{1}{9}, \beta_\infty^* = 0.09, \beta_i = 0.072, R_k = 6, \alpha_0^* = \frac{\beta_i}{3}, \sigma_k = \sigma_\omega = 2.0 \quad (50)$$

2.4.3.2 BSL k - ω model

The main problem with the standard k - ω model is its well known strong sensitivity to freestream conditions. The baseline (BSL) k - ω model was developed by Menter [194] to effectively blend the robust and accurate formulation of the k - ω model in the near-wall region with the freestream independence of the k - ϵ model in the far field. To

achieve this, the k - ϵ model is converted into a k - ω formulation. The BSL k - ω model is similar to the standard k - ω model, but includes the following refinements [176]:

- (i) The standard k - ω model and the transformed k - ϵ model are both multiplied by a blending function and both models are added together. The blending function is designed to be one in the near-wall region, which activates the standard k - ω model, and zero away from the surface, which activates the transformed k - ϵ model.
- (ii) The BSL model incorporates a damped cross-diffusion derivative term in the equation.
- (iii) The modeling constants are different.

In the BSL k - ω model, the turbulent Prandtl numbers for k and ω are:

$$\sigma_k = \frac{1}{F_1/\sigma_{k,1} + (1 - F_1)/\sigma_{k,2}} \quad (51)$$

$$\sigma_\omega = \frac{1}{F_1/\sigma_{\omega,1} + (1 - F_1)/\sigma_{\omega,2}} \quad (52)$$

where the blending function F_1 is given by:

$$F_1 = \tanh(\phi_1^4) \quad (53)$$

$$\phi_1 = \min \left[\max \left(\frac{\sqrt{k}}{0.09\omega y}, \frac{500\mu}{\rho y^2 \omega} \right), \frac{4\rho k}{\sigma_{\omega,2} D_\omega^+ y^2} \right] \quad (54)$$

$$D_\omega^+ = \max[D_\omega, 10^{-10}] \quad (55)$$

The cross-diffusion term is defined as:

$$D_\omega = 2(1 - F_1)\rho \frac{1}{\omega\sigma_{\omega,2}} \frac{\partial k}{\partial x_j} \frac{\partial \omega}{\partial x_j} \quad (56)$$

where the constants are given by:

$$\sigma_{k,1} = 2.0, \sigma_{k,2} = 1.0, \sigma_{\omega,1} = 2.0, \sigma_{\omega,2} = 1.168 \quad (57)$$

The production of ω is given by:

$$G_\omega = \frac{\alpha\alpha^*}{\nu_t} G_k \quad (58)$$

For the BSL k - ω model, α_∞ is given by:

$$\alpha_\infty = F_1\alpha_{\infty,1} + (1 - F_1)\alpha_{\infty,2} \quad (59)$$

where

$$\alpha_{\infty,1} = \frac{\beta_{i,1}}{\beta_\infty^*} - \frac{\kappa^2}{\sigma_{\omega,1}\sqrt{\beta_\infty^*}} \quad (60)$$

and

$$\alpha_{\infty,2} = \frac{\beta_{i,2}}{\beta_\infty^*} - \frac{\kappa^2}{\sigma_{\omega,2}\sqrt{\beta_\infty^*}} \quad (61)$$

$$\kappa = 0.41, \beta_{i,1} = 0.075, \beta_{i,2} = 0.0828, \beta_\infty^* = 0.09 \quad (62)$$

The dissipation of turbulence kinetic energy is defined as:

$$Y_k = \rho\beta^*k\omega \quad (63)$$

The dissipation of ω is given by:

$$Y_\omega = \rho\beta_i\omega^2 \quad (64)$$

where

$$\beta_i = F_1\beta_{\infty,1} + (1 - F_1)\beta_{\infty,2} \quad (65)$$

2.4.3.3 SST k - ω model

The SST k - ω model includes all the refinements of the BSL k - ω model, and in addition accounts for the transport of the turbulence shear stress in the definition of the turbulent viscosity. These features make the SST k - ω model [194] more accurate and reliable for a wider class of flows than the standard and the BSL k - ω models.

In the SST k - ω model, the turbulent viscosity is modeled as:

$$\mu_t = \frac{\rho k}{\omega} \frac{1}{\max\left[\frac{1}{\alpha^*}, \frac{SF_2}{\alpha_1\bar{\omega}}\right]} \quad (66)$$

where

$$F_2 = \tanh(\phi_2^2) \quad (67)$$

$$\phi_2 = \max\left[2\frac{\sqrt{k}}{0.09\omega y}, \frac{500\mu}{\rho y^2\omega}\right] \quad (68)$$

The production of k for the SST k - ω model is given by:

$$G_k^* = \min[G_k, 10\rho\beta^*k\omega] \quad (69)$$

where the model constants are [194]:

$$\alpha_1 = 0.31, \sigma_{k,1} = 1.176 \quad (70)$$

2.4.4 Transitional models

2.4.4.1 Three equations k - kl - ω model

The k - kl - ω model, is a recent transitional eddy viscosity model developed by Walters and Cokljat [195]. It includes transport equations for turbulent kinetic energy (k_T), laminar kinetic energy (k_L), and the inverse turbulent time scale (ω).

In the k - kl - ω model, the Boussinesq hypothesis is rewritten as follows:

$$-\overline{u'_i u'_j} = \nu_{TOT} \left(\frac{\partial \overline{u}_i}{\partial x_j} + \frac{\partial \overline{u}_j}{\partial x_i} \right) - \frac{2}{3} K_{TOT} \sigma_{ij} \quad (71)$$

where

$$\nu_{TOT} = \nu_{T,S} + \nu_{T,1} \quad (72)$$

$$k_{TOT} = k_T + k_L \quad (73)$$

$$\nu_{T,S} = f_\nu f_{INT} C_\mu \sqrt{k_{T,S}} \lambda_{eff} \quad (74)$$

$$C_\mu = \frac{1}{A_0 + A_s(S/\omega)} \quad (75)$$

$$f_\nu = 1 - \exp\left(-\frac{\sqrt{Re_{T,S}}}{A_\nu}\right) \quad (76)$$

A damping function defining the turbulent production due to intermittency is given by:

$$f_{INT} = \min\left[\frac{k_L}{C_{INT} k_{TOT}}, 1\right] \quad (77)$$

$$Re_{T,S} = \frac{f_W^2 k_T}{\nu \omega} \quad (78)$$

The effective length λ_{eff} is defined as:

$$\lambda_{eff} = \min(C_\lambda d, \lambda_T) \quad (79)$$

where λ_T is the turbulent length scale defined as:

$$\lambda_T = \frac{\sqrt{k}}{\omega} \quad (80)$$

The small scale energy $k_{T,S}$ is given by:

$$k_{T,S} = f_{SS} f_W k_T \quad (81)$$

$$f_W = \frac{\lambda_{eff}}{\lambda_T} \quad (82)$$

$$f_{SS} = \exp \left[- \left(\frac{C_{SS} \nu \Omega}{k_T} \right)^2 \right] \quad (83)$$

$$\nu_{T,1} = \text{MIN} \left\{ \nu_{T,1}^*, \frac{0.5(k_L + k_{T,1})}{S} \right\} \quad (84)$$

$$\nu_{T,1}^* = f_{\tau,1} C_{11} \left(\frac{\Omega \lambda_{eff}^2}{\nu} \right) \sqrt{k_{T,1} \lambda_{eff}} + \beta_{TS} C_{12} \phi_{NAT} d^2 \Omega \quad (85)$$

The time-scale-based damping function is:

$$f_{\tau,1} = 1 - \exp \left[-C_{\tau,1} \frac{k_{T,1}}{\lambda_{eff}^2 \Omega^2} \right] \quad (86)$$

$$\beta_{TS} = 1 - \exp \left[- \frac{\text{MAX}(\phi_{NAT} - C_{TS,crit}, 0)^2}{A_{TS}} \right] \quad (87)$$

$$\phi_{NAT} = \frac{d^2 \Omega}{\nu} \quad (88)$$

where

$$k_{T,1} = k_T - k_{T,S} \quad (89)$$

The laminar kinetic energy (k_T), the turbulent kinetic energy (k_L) and the inverse turbulent time scale (ω) are obtained from the following transport equations:

$$\frac{Dk_T}{Dt} = P_{k_T} + R + R_{NAT} - \omega k_T - D_T + \frac{\partial}{\partial x_j} \left[\left(\nu + \frac{\alpha_T}{\sigma_k} \right) \frac{\partial k_T}{\partial x_j} \right] \quad (90)$$

$$\frac{Dk_L}{Dt} = P_{k_L} + R + R_{NAT} - D_L + \frac{\partial}{\partial x_j} \left[\nu \frac{\partial k_L}{\partial x_j} \right] \quad (91)$$

$$\begin{aligned} \frac{D\omega}{Dt} = & C_{\omega 1} \frac{\omega}{k_T} P_{k_T} + \left(\frac{C_{\omega} R}{f_W} - 1 \right) \frac{\omega}{k_T} (R + R_{NAT}) - C_{\omega 2} \omega^2 + C_{\omega 3} f_{\omega} \alpha_T f_W^2 \frac{\sqrt{k_T}}{d^3} \\ & + \frac{\partial}{\partial x_j} \left[\left(\nu + \frac{\alpha_T}{\sigma_{\omega}} \right) \frac{\partial \omega}{\partial x_j} \right] \end{aligned} \quad (92)$$

The turbulence production term generated by turbulent fluctuations is given by:

$$P_{k_L} = \nu_{T,S} S^2 \quad (93)$$

$$P_{k_L} = \nu_{T,1} S^2 \quad (94)$$

The near-wall dissipation D_T and D_L are given respectively by:

$$D_T = 2\nu \frac{\partial \sqrt{k_T}}{\partial x_j} \frac{\partial \sqrt{k_T}}{\partial x_j} \quad (95)$$

$$D_L = 2\nu \frac{\partial \sqrt{k_L}}{\partial x_j} \frac{\partial \sqrt{k_L}}{\partial x_j} \quad (96)$$

In the transport equations (90-92), R represents the averaged effect of the breakdown of streamwise fluctuations into turbulence during bypass transition:

$$R = \frac{C_R \beta_{BP} k_L \omega}{f_W} \quad (97)$$

where

$$\beta_{BP} = 1 - \exp\left(-\frac{\phi_{BP}}{A_{BP}}\right) \quad (98)$$

$$\phi_{BP} = \text{MAX}\left[\left(\frac{k_T}{\nu \Omega} - C_{BP,crit}\right), 0\right] \quad (99)$$

The breakdown to turbulence due to instabilities is considered to be a natural transition production term, given by:

$$R_{NAT} = C_{R,NAT} \beta_{NAT} k_L \Omega \quad (100)$$

$$\beta_{NAT} = 1 - \exp\left[\frac{-\text{MAX}(\phi_{NAT} - C_{NAT,crit}/f_{NAT,crit}, 0)}{A_{NAT}}\right] \quad (101)$$

$$f_{NAT,crit} = 1 - \exp\left(-C_{NC} \sqrt{\frac{k_L d}{\nu}}\right) \quad (102)$$

The damping function is defined as:

$$f_\omega = 1 - \exp\left[-0.41 \left(\frac{\lambda_{eff}}{\lambda_T}\right)^4\right] \quad (103)$$

The turbulent scalar diffusivity is defined as:

$$\alpha_T = f_\nu C_{\mu,std} \sqrt{k_{T,S}} \lambda_{eff} \quad (104)$$

The model constants for the k - kl - ω transition model are listed below:

$$\begin{aligned}
 A_0 = 4.04, A_s = 2.12, A_\nu = 6.75, A_{BP} = 0.6, A_{NAT} = 200, A_{TS} = 200, C_{BP,crit} & \quad (105) \\
 = 1.2, C_{NC} = 0.1, C_{NAT,crit} = 1250, C_{INT} = 0.75, C_{TS,crit} \\
 = 1000, C_{R,NAT} = 0.02, C_{11} = 3.4 \times 10^{-6}, C_{12} = 1.0 \times 10^{-10}, \\
 C_R = 0.12, C_{\alpha,\theta} = 0.035, C_{SS} = 1.5, C_{\tau,1} = 4360, C_{\omega_1} \\
 = 0.44, C_{\omega_2} = 0.92, C_{\omega_3} = 0.3, C_{\omega_R} = 1.5, C_\lambda = 2.495, C_{\mu,std} \\
 = 0.09, \sigma_k = 1, \sigma_\omega = 1.17
 \end{aligned}$$

2.4.4.2 Four equations γ - Re_θ model

The γ - Re_θ model [196, 203, 204] (also known as the transition SST model) is based on the coupling of the SST transport equations with two other transport equations, one for the intermittency and one for the transition onset criteria, in terms of momentum-thickness Reynolds number.

The γ - Re_θ model computes the eddy viscosity as:

$$\mu_t = \frac{\rho k}{\omega} \quad (106)$$

The transport equation for the intermittency γ is defined by:

$$\frac{\partial(\rho\gamma)}{\partial t} + \frac{\partial(\rho U_j \gamma)}{\partial x_j} = P_{\gamma 1} - E_{\gamma 1} + P_{\gamma 2} - E_{\gamma 2} + \frac{\partial}{\partial x_j} \left[\left(\mu + \frac{\mu_t}{\sigma_\gamma} \right) \frac{\partial \gamma}{\partial x_j} \right] \quad (107)$$

where

$$P_{\gamma 1} = C_{a1} F_{length} \rho S [\gamma F_{onset}]^{C_{\gamma 3}} \quad (108)$$

$$E_{\gamma 1} = C_{e1} P_{\gamma 1} \gamma \quad (109)$$

$$P_{\gamma 2} = C_{a2} \rho \Omega \gamma F_{turb} \quad (110)$$

$$E_{\gamma 2} = C_{e2} P_{\gamma 2} \gamma \quad (111)$$

where $\Omega = (2\Omega_{ij}\Omega_{ij})^{1/2}$ is the absolute value of vorticity.

The transition onset is controlled by the following functions:

$$Re_V = \frac{\rho y^2 S}{\mu} \quad (112)$$

$$R_T = \frac{\rho k}{\mu \omega} \quad (113)$$

$$F_{onset1} = \frac{Re_V}{2193Re_{\theta c}} \quad (114)$$

$$F_{onset2} = MIN[MAX(F_{onset1}, F_{onset1}^4), 2] \quad (115)$$

$$F_{onset3} = MAX \left[1 - \left(\frac{Re_T}{25} \right)^3, 0 \right] \quad (116)$$

$$F_{onset} = MAX(F_{onset2} - F_{onset3}, 0) \quad (117)$$

$$F_{turb} = exp \left(- \left(\frac{R_T}{4} \right)^4 \right) \quad (118)$$

The transport equation for the transition momentum thickness Reynolds number is:

$$\frac{\partial(\rho R\tilde{e}_{\theta t})}{\partial t} + \frac{\partial(\rho U_j R\tilde{e}_{\theta t})}{\partial x_j} = P_{\theta t} + \frac{\partial}{\partial x_j} \left[\sigma_{\theta t} (\mu + \mu_t) \frac{\partial R\tilde{e}_{\theta t}}{\partial x_j} \right] \quad (119)$$

where the source term $P_{\theta t}$ is defined as follows:

$$P_{\theta t} = C_{\theta t} \frac{\rho}{t} (Re_{\theta t} - R\tilde{e}_{\theta t})(1 - F_{\theta t}) \quad (120)$$

$$t = \frac{500\mu}{\rho U^2} \quad (121)$$

$$F_{\theta t} = MIN \left[MAX \left(F_{wake} exp \left(- \left(\frac{\gamma}{\delta} \right)^4 \right), 1 - \left(\frac{\gamma - 1/50}{1 - 1/50} \right)^2, 1 \right) \right] \quad (122)$$

$$\theta_{BL} = \frac{R\tilde{e}_{\theta t} \mu}{\rho U} \quad (123)$$

$$\delta_{BL} = \frac{15}{2} \theta_{BL} \quad (124)$$

$$\delta = \frac{50\Omega y}{U} \delta_{BL} \quad (125)$$

$$Re_w = \frac{\rho \omega y^2}{\mu} \quad (126)$$

$$F_{wake} = exp \left(- \left(\frac{Re_w}{10^5} \right) \right) \quad (127)$$

$$F_{length} = \left\{ \begin{array}{ll} [\alpha_1 + \alpha_2 R\tilde{e}_{\theta t} + \alpha_3 R\tilde{e}_{\theta t}^2], & R\tilde{e}_{\theta t} < 400 \\ [\alpha_4 + \alpha_5 R\tilde{e}_{\theta t} + \alpha_6 R\tilde{e}_{\theta t}^2 + \alpha_7 R\tilde{e}_{\theta t}^3], & 400 \leq R\tilde{e}_{\theta t} < 596 \\ [\alpha_8 + (R\tilde{e}_{\theta t} - \alpha_9) \cdot \alpha_{10}], & 596 \leq R\tilde{e}_{\theta t} < 1200 \\ [\alpha_{11}], & R\tilde{e}_{\theta t} \geq 1200 \end{array} \right\} \quad (128)$$

where

$$\begin{aligned}
 \alpha_1 &= 398.189 \times 10^{-1}, \alpha_2 = -119.270 \times 10^4, \alpha_3 = -132.567 \times 10^{-6}, \alpha_4 \\
 &= 263.404, \alpha_5 = -123.939 \times 10^{-2}, \alpha_6 = 194.548 \times 10^{-5}, \alpha_7 \\
 &= -101.695 \times 10^{-8}, \alpha_8 = 0.5, \alpha_9 = -596, \alpha_{10} = 3 \times 10^{-4}, \alpha_{11} \\
 &= 0.3188
 \end{aligned} \tag{129}$$

$$Re_{\theta t} = \begin{cases} \left[1173.51 - 589.428Tu + \frac{0.2196}{Tu^2} \right] F(\lambda_\theta), & Tu \leq 1.3 \\ 331.50[Tu - 0.5658]^{-0.671} F(\lambda_\theta), & Tu > 1.3 \end{cases} \tag{130}$$

$$F(\lambda_\theta) = \begin{cases} 1 - [-12.986\lambda_\theta - 123.66\lambda_\theta^2 - 405.689\lambda_\theta^3] e^{(-\frac{Tu}{1.5})^{1.5}}, & \lambda_\theta \leq 0 \\ 1 + 0.275[1 - e^{(-35\lambda_\theta)}] e^{(-\frac{Tu}{0.5})}, & \lambda_\theta > 0 \end{cases} \tag{131}$$

This empirical correlation is a function of the local turbulence intensity Tu and the Thwaites' pressure gradient coefficient λ_θ :

$$Tu = \frac{100}{U} \sqrt{\frac{2}{3}} k \tag{132}$$

$$\lambda_\theta = \left(\frac{\theta^2}{\nu} \right) \frac{dU}{dS} \tag{133}$$

where $Re_{\theta c}$ is given as:

$$Re_{\theta c} = \begin{cases} [R\tilde{e}_{\theta t} + b_1 + b_2 R\tilde{e}_{\theta t} + b_3 R\tilde{e}_{\theta t}^2 + b_4 R\tilde{e}_{\theta t}^3 + b_5 R\tilde{e}_{\theta t}^4], & R\tilde{e}_{\theta t} \leq 1870 \\ [R\tilde{e}_{\theta t} - (b_6 + (R\tilde{e}_{\theta t} + b_7) \times b_8)], & R\tilde{e}_{\theta t} > 1870 \end{cases} \tag{134}$$

where

$$\begin{aligned}
 b_1 &= 396.035 \cdot 10^{-2}, b_2 = -120.656 \cdot 10^{-4}, b_3 = 868.230 \cdot 10^{-6}, b_4 \\
 &= -696.506 \cdot 10^{-9}, b_5 = 174.105 \cdot 10^{-12}, b_6 = 593.11, b_7 \\
 &= 1870.0, b_8 = 0.482
 \end{aligned} \tag{135}$$

The γ - Re_θ model interacts with the SST model by modification of the k as follows:

$$\frac{\partial(\rho k)}{\partial t} + \frac{\partial(\rho k u_i)}{\partial x_i} = \frac{\partial}{\partial x_j} \left[\left(\mu + \frac{\mu_t}{\sigma_k} \right) \frac{\partial k}{\partial x_j} \right] + C_k^* - Y_k^* + S_k \tag{136}$$

$$C_k^* = \gamma_{eff} G_k \tag{137}$$

$$Y_k^* = MIN[MAX(\gamma_{eff}, 0.1), 1.0] Y_k \tag{138}$$

$$\gamma_{eff} = MAX[\gamma, \gamma_{sep}] \tag{139}$$

$$\gamma_{sep} = MIN[C_{s1} MAX[(Re_v/3.235 Re_{\theta c}) - 1, 0] F_{reattch}, 2] F_{\theta t} \tag{140}$$

$$F_{reattach} = \exp\left(-\left(\frac{R_T}{20}\right)^4\right) \quad (141)$$

The constants of the γ - Re_θ model are:

$$\begin{aligned} C_{a1} = 2, C_{e1} = 1, C_{a2} = 0.06, C_{e2} = 50, c_{\gamma3} = 0.5, \sigma_\gamma = 1.0, c_{\theta t} = 0.03, \sigma_{\theta t} \\ = 2.0, C_{s1} = 2.0 \end{aligned} \quad (142)$$

2.4.5 Reynolds stresses models

Abandoning the isotropic eddy-viscosity hypothesis, the RSM closes the Reynolds-averaged Navier-Stokes equations by solving transport equations for the Reynolds stresses, together with an equation for the dissipation rate. The exact form of the Reynolds stress transport equations may be derived by taking moments of the exact momentum equation. This is a process wherein the exact momentum equations for the fluctuations are multiplied by the fluctuating velocities and averaged, the product then being Reynolds-averaged.

The exact transport equations for the transport of the Reynolds stresses ($\overline{\rho u'_i u'_j}$) may be written as follows [197, 199, 205]:

$$\begin{aligned} & \underbrace{\frac{\partial}{\partial t}(\overline{\rho u'_i u'_j})}_{\text{Local Time Derivative}} + \underbrace{\frac{\partial}{\partial x_k}(\overline{\rho u'_k u'_i u'_j})}_{C_{ij} \equiv \text{Convection}} \\ &= - \underbrace{\frac{\partial}{\partial x_k} [\overline{\rho u'_i u'_j u'_k} + p'(\delta_{kj} u'_i + \delta_{ik} u'_j)]}_{D_{T,ij} \equiv \text{Turbulence Diffusion}} \\ &+ \underbrace{\frac{\partial}{\partial x_k} \left[\mu \frac{\partial}{\partial x_k} (\overline{u'_i u'_j}) \right]}_{D_{L,ij} \equiv \text{Molecular Diffusion}} - \underbrace{\rho \left(\overline{u'_i u'_k} \frac{\partial u'_j}{\partial x_k} + \overline{u'_j u'_k} \frac{\partial u'_i}{\partial x_k} \right)}_{P_{ij} \equiv \text{Stress Production}} - \underbrace{\rho \beta (\overline{g_i u'_j \theta} + \overline{g_j u'_i \theta})}_{G_{ij} \equiv \text{Buoyancy Production}} \\ &+ \underbrace{p' \left(\frac{\partial u'_i}{\partial x_j} + \frac{\partial u'_j}{\partial x_i} \right)}_{\phi_{ij} \equiv \text{Pressure Strain}} - \underbrace{2\mu \left(\frac{\partial u'_i}{\partial x_k} + \frac{\partial u'_j}{\partial x_k} \right)}_{\epsilon_{ij} \equiv \text{Dissipation}} - \underbrace{2\rho \Omega_k (\overline{u'_j u'_m} \epsilon_{ikm} + \overline{u'_i u'_m} \epsilon_{jkm})}_{F_{ij} \equiv \text{Production by System Rotation}} \end{aligned} \quad (143)$$

Of the various terms in these exact equations C_{ij} , $D_{L,ij}$, P_{ij} and F_{ij} do not require any modeling. However, $D_{T,ij}$, G_{ij} , ϕ_{ij} and ϵ_{ij} need to be modeled to close the equations.

Several types of RSM models are available. In this work, the Linear Pressure-Strain (RSM-LPS) model [197-200] has been used.

2.5 Eulerian-Lagrangian approach

The Eulerian-Lagrangian approach used in this study will be described in the following sections. In this approach, the fluid phase is treated as a continuum by solving the Navier-Stokes equations, while the dispersed phase is solved by tracking a large number of particles through the calculated flow field.

2.5.1 Particles motion equation

The trajectory of a discrete phase particle is predicted by integrating the force balance on the particle, which is written in a Lagrangian reference frame. This force balance equates the particle inertia with the forces acting on the particle, and can be written as [173, 206, 207]:

$$\frac{d\vec{u}_p}{dt} = \underbrace{F_D(\vec{u} - \vec{u}_p)}_{\text{Drag force}} + \underbrace{\frac{\vec{g}(\rho_p - \rho)}{\rho_p}}_{\text{Gravity force}} + \underbrace{\vec{F}}_{\text{Other forces}} \quad (144)$$

where \vec{u} is the fluid phase velocity, \vec{u}_p is the particle velocity, ρ is the fluid density, ρ_p is the density of the particle and $F_D(\vec{u} - \vec{u}_p)$ is the drag force per unit particle mass. where

$$F_D = \frac{18\mu C_D Re}{\rho_p d_p^2 24} \quad (145)$$

where μ denotes the molecular viscosity of the fluid, d_p is the particle diameter, C_D is the drag coefficient and Re is the dispersed phase Reynolds number (or relative Reynolds number), which is defined as:

$$Re \equiv \frac{\rho d_p |u_p - u|}{\mu} \quad (146)$$

2.5.2 Drag force model

For calculating the drag coefficient of the sand particles, several correlations are available in the literature. In this study, we assume that the sand particles are smooth and have a spherical shape. In this case, the correlation proposed by Morsi and Alexander [208] (for smooth spherical particles) can be used. This empirical correlation can be written as a function of dispersed phase Reynolds number as:

$$C_D = a_1 + \frac{a_2}{Re} + \frac{a_3}{Re^2} \quad (147)$$

where a_1 , a_2 , and a_3 are constants [208].

2.5.3 Modeling particles rotation

For modeling the rotation of the particles on the fluid, an additional force has been used. For rotation defined about the (z) axis, the forces on the particles in the Cartesian (x) and (y) directions can be written respectively as [176]:

$$\left(1 - \frac{\rho}{\rho_p}\right) \Omega^2 x + 2\Omega \left(u_{p,y} - \frac{\rho}{\rho_p} u_y\right) \quad (148)$$

$$\left(1 - \frac{\rho}{\rho_p}\right) \Omega^2 y + 2\Omega \left(u_{p,x} - \frac{\rho}{\rho_p} u_x\right) \quad (149)$$

where $u_{p,y}$ and u_y are the particle and fluid velocities in the Cartesian y direction, $u_{p,x}$ and u_x are the particle and fluid velocities in the Cartesian x direction, and Ω is the rotational speed.

2.5.4 Other forces

In the literature, the Saffman's lift force, or lift due to shear, can also be included in the particles force balance. The lift force evaluated in this study is based on the work of Li et al. [209] and Saffman [210]. This lift force is given by:

$$\vec{F} = \frac{2K v^{1/2} \rho d_{ij}}{\rho_p d_p (d_{lk} d_{kl})^{1/4}} (\vec{u} - \vec{u}_p) \quad (150)$$

where K is a constant ($= 2.594$) and d_{ij} is the deformation tensor.

Chapter 3

Numerical method

3.1 Selected wind turbine model

The acceptance, validation and development of numerical tools for wind turbines have all depended, in large part, on the availability of good experimental data under controlled conditions. The NREL/NASA AMES wind tunnel experiment in 1999 [211, 212] may be the most well known experiment of recent decades.

The experimental measurements conducted by NREL [213] focused on aerodynamic loads on the rotor, disregarding wake behaviour; given the absence of detailed flow measurements using advanced techniques such as laser Doppler anemometry (LDA) and particle image velocimetry (PIV), this led the Energy Research Centre of the Netherlands (ECN) and its partners to perform highly successful aerodynamic experiments in Europe's largest wind tunnel, under a program called the MEXICO project (Model rotor EXperiments In COntrolled conditions) [214, 215].

These MEXICO experiments were carried out in the large-scale, low-speed facility (LLF) at the German Dutch wind tunnels (DNW), a high-quality wind tunnel with a 9.5 x 9.5 m² open test section. The first series of experiments were performed in December 2006 [5, 214, 216]. Between June 20 and July 4, 2014, the New MEXICO measurements followed up the first test campaign, using the same model [215, 217].

In addition to detailed rotor load measurements on the wind turbine blades and detailed PIV measurements in the wake contained in both the MEXICO and the New MEXICO measurements, another unique feature of the New MEXICO experiment was the availability of both natural and tripped flow conditions: these allowed for an investigation into the effect of laminar/turbulent transition [75].

Another advantage of using the MEXICO model is the fact that these measurements were performed in the open test section of the wind tunnel at DNW, at very low turbulence intensity [215]; this rendered the effect of tunnel geometry negligible, as had already been demonstrated in a previous study [23]. The results can thus be generalized for cases under real atmospheric conditions and for full-scale wind turbine applications.

3.1.1 New MEXICO measurements

The New MEXICO experiments tested three different wind speeds: low wind speed ($U_\infty = 10$ m/s), design condition ($U_\infty = 15$ m/s) and separated flow condition ($U_\infty = 24$ m/s) in the both yawed and no-yawed inflow conditions. In this thesis, only the no-yawed case has been considered.

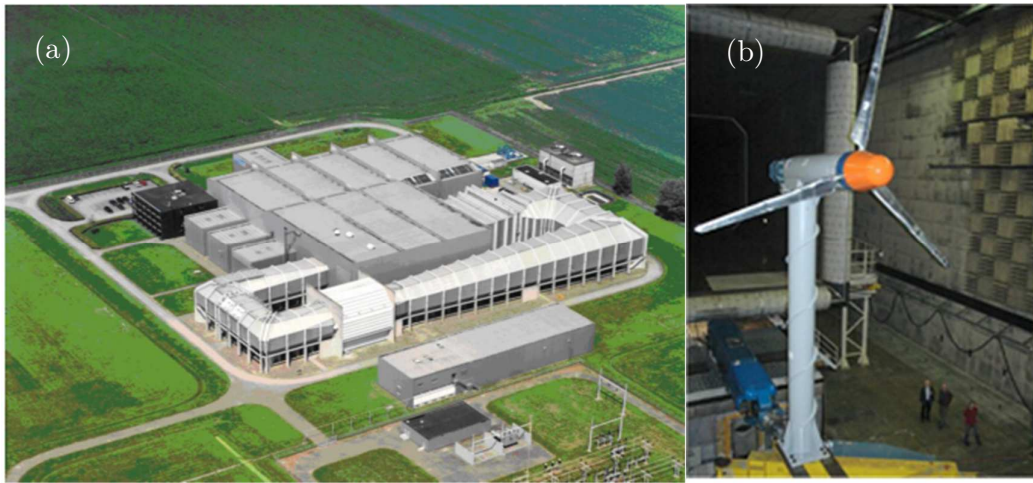


Figure 20: (a) The German Dutch wind tunnels (DNW), and (b) The MEXICO wind turbine model. Reproduced from [5].

The pressure distribution at five spanwise positions representing: 25%, 35%, 60%, 82% and 92% of the blade span was measured using about 150 dynamic pressure sensors. The pressure sensors are distributed on the three blades (Figure 21): Blade 1 (25% and 35% span), blade 2 (60% span), and blade 3 (82% and 92% span).

In addition to the pressure measurements, the axial, radial and tangential velocities in the three flow directions (x , y and z) at the near wake were measured at the horizontal plane (9 o'clock position plan) using PIV stereos. The axial transverses which cover a distance about 10 m from upstream to downstream were measured in two positions: inboard part ($y=0.5$ m) and outboard part ($y=1.5$ m). The radial transverses which cover about 3 m have been measured in two positions: upstream ($x=-0.3$ m) and

downstream ($x=0.3$ m) [5, 214-218]. An overview of a detailed MEXICO wind turbine within the framework of New MEXICO measurements is shown in Table 3.

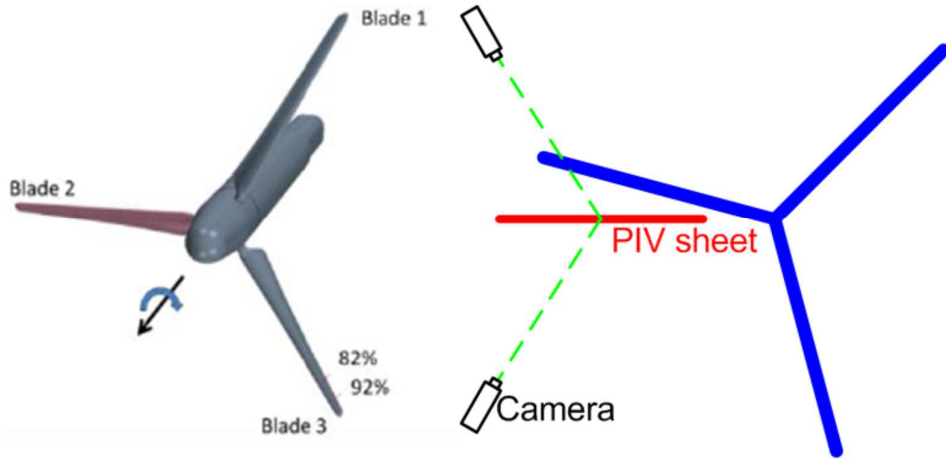


Figure 21: MEXICO experiments: pressure sensors distribution and PIV sheet position with cameras. Reproduced from [4, 218].

Table 3: General information about MEXICO wind turbine model.

Rotation direction	Clockwise
Power regulation	Not present, speed control by motor/generator
Number of blades	3
Rotational speed	425.1 (rpm)
Rotor diameter	4.5 (m)
Blade material	Aluminum 7075-T651 Alloy
Global pitch angle	-2.3 (°)
Tower height	5.12 (m)

3.1.2 MEXICO blade

The MEXICO rotor is a three-bladed model of 4.5 m diameter equipped with a pitch actuator and speed controller. The MEXICO blade is aerodynamically complicated, when compared with other blade models such as NREL blades; the MEXICO blade is composed of three different families of aerodynamic profiles [215, 218]:

- (i) The DU91-W2-250 airfoil, developed at Delft University of Technology, is applied to the root of the blade, from 20 to 45.6% span.
- (ii) The RISØ-A1-21 airfoil, developed at the National Laboratory of Denmark, is applied from 54.4% to 65.6% in mid span.

- (iii) The NACA 64-418 airfoil, designed by the National Advisory Committee for Aeronautics at NASA, is applied in the outer part from 74.4% span.

The distribution of twist and chord along the MEXICO blade span is shown in Figure 22 (a). From this figure, we see that twist can reach (16.4°) as the maximum value in the root part of the blade. The blade's configuration is shown in Figure 22 (b). For more information on tunnel geometry and turbine details, see [5, 214-218].

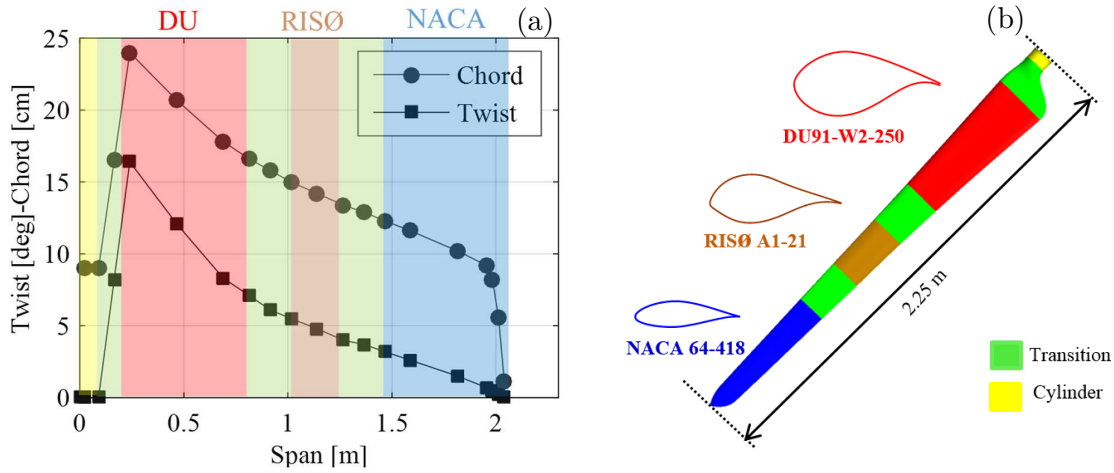


Figure 22: (a) Twist/chord distribution along the blade span, and (b) The MEXICO blade airfoil configuration.

3.2 Geometry design

The 3D geometry of the MEXICO blade was generated based on three datasets of 2D airfoil coordinates: (DU91-W2-250, RISØ-A1-21 and NACA 64-418) as well as on the detailed blade geometry (given in Appendix A) using SolidWorks Software (see Figure 23 and 24).

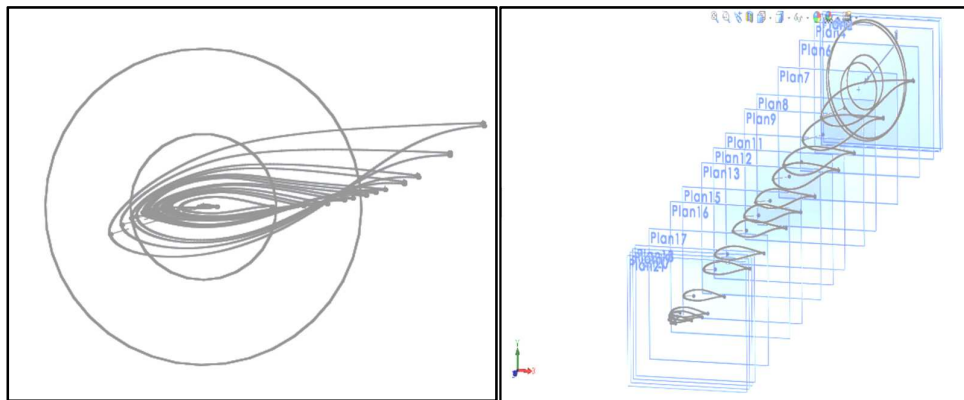


Figure 23: Aerofoil profiles of the blade in SolidWorks.

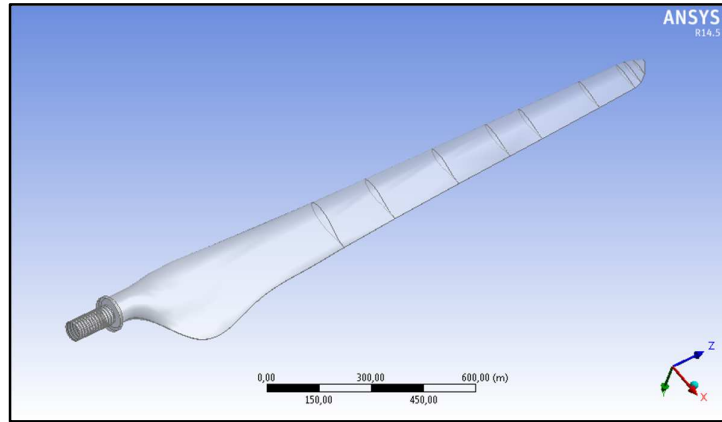


Figure 24: Three-dimensional geometry of the MEXICO blade model.

3.3 Computational domain

It was not necessary to take the full geometry of a wind turbine (tower and nacelle) into account in CFD simulations under no-yawed flow conditions, according to [3, 54, 63, 133], and, in order to reduce computational time due to the symmetry flow field around the MEXICO rotor, the computational domain was constructed only on one blade, representing one-third of the full rotor geometry exploiting the 120° symmetry of the computational domain.

The inlet boundary of the computational domain was located five blade radii upstream, and the outlet was located ten blade radii downstream (Figure 25). The radius of the computational domain was five blade radii. A small zone close to the blade with a diameter of two blade radii and a length of one blade radii was designed (Figure 26) with two goals in mind: separating the rotating part into stationary parts, and refining the grid in the near-blade region.

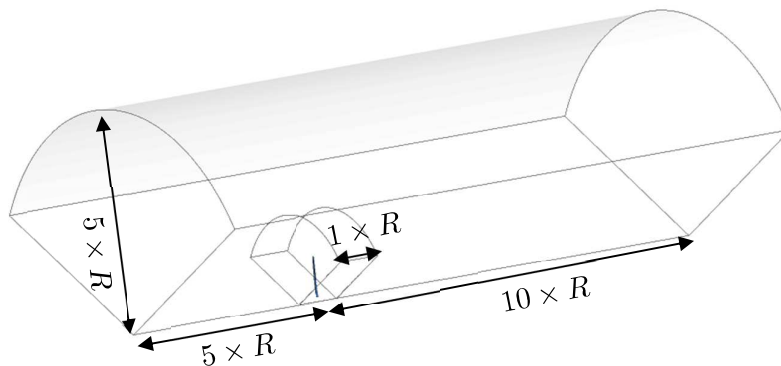


Figure 25: 3D computational domain and dimensions.

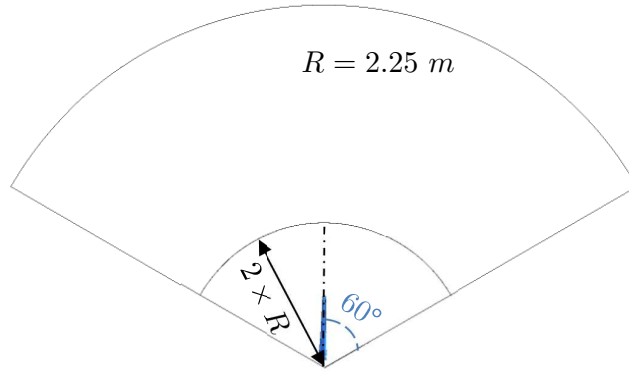


Figure 26: Cross-section of the computational domain.

3.4 Computational mesh

In each CFD simulation, it is crucial to begin by studying mesh independence, in order to find a type of mesh, where the results not be altered by the refinement of the mesh. In this study, the ANSYS Mesh CFD software (v 17.2) was used for generating the mesh. In this software, different types of meshes and techniques are available. In the following sections, the techniques used and the mesh sensitivity test will be presented.

3.4.1 Mesh strategy

In the CFD computation of wind turbine aerodynamics, the flow domain entails rotating blades and the stationary outer boundaries. The rotation of a wind turbine can be treated by either the multiple reference frame (MRF) approach or a moving mesh technique. The MRF method, often referred to as a frozen-rotor approach, is a steady-state approximation that includes various additional rotational terms in the governing equations expressed in the rotating zone. It is appropriate especially for RANS simulations [3]. The moving mesh approach is more computationally expensive [219]. In this work, the MRF approach has been used.

The mesh strategy can be classified into sliding mesh technique and overset (also known as Chimera or composite) grid method [220]. Figure 27 illustrates the difference between these techniques. The Chimera grid approach entails a rotating cylinder overlapped on a stationary mesh, whereas the sliding mesh employs a rotating cylindrical mesh sliding along the interface separating the dynamic from stationary subdomains. Each approach has strength and weakness. The Chimera mesh is easier to create but computationally more demanding in comparison with sliding mesh. The

sliding mesh methodology is moderately more popular [3, 27], thus, it has been used in this work.

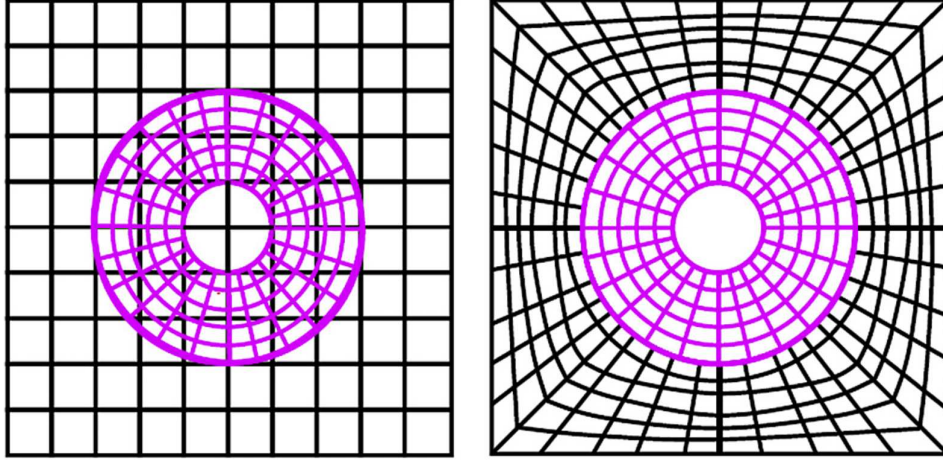


Figure 27: The representative diagram of (left) overset grid, and (right) sliding mesh technique. Reproduced from [3, 219].

3.4.1 Prismatic layers

Using an unstructured flow solver with tetrahedral cells, the grid generation process is less cumbersome. But the problem of resolving very thin boundary layers using tetrahedral cells is well known [10, 27], and it may be necessary to combine the solver with some kind of prismatic grids near the blade surface to avoid this problem.

For generating prismatic layers, two parameters are needed to define, the first element height and the mesh growth rate.

In this work, the first element height has been estimated using the inverse y^+ relationship as:

$$y_p = \frac{y^+ \mu}{U_\tau \rho} \quad (151)$$

where y_p is the first element height close to the blade wall and U_τ is the friction velocity defined by:

$$U_\tau = \sqrt{\frac{\tau_w}{\rho}} \quad (152)$$

where τ_w is the wall shear stress defined as:

$$\tau_w = \frac{1}{2} C_f \rho U_\infty^2 \quad (153)$$

where C_f is the skin friction, which it has been estimated in this work using Schlichting correlation [221]:

$$C_f = [2 \log_{10}(Re) - 0.65]^{-2.3} \text{ for } Re < 10^9 \quad (154)$$

where Re is the Reynolds number, based on the blade radius R :

$$Re = \frac{\rho U_\infty R}{\mu} \quad (155)$$

In this study, the value of 1.2 was used for the mesh growth rate. This value was chosen from experiences by comparing different values ranging from 1.05 to 1.3.

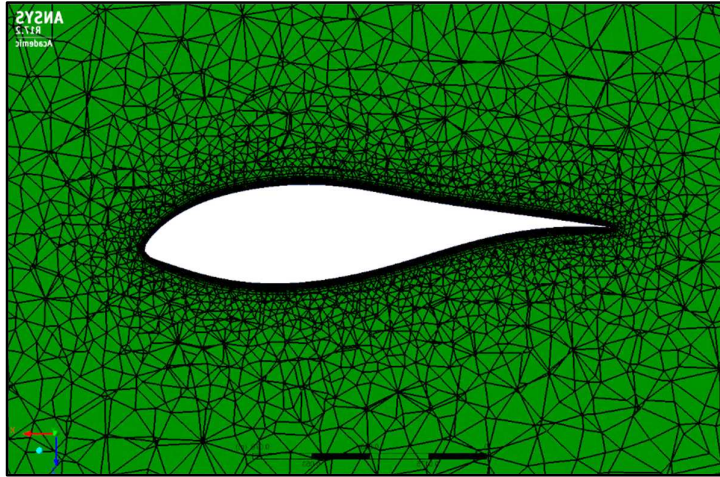


Figure 28: Section view of the mesh at 60 % of the blade span.

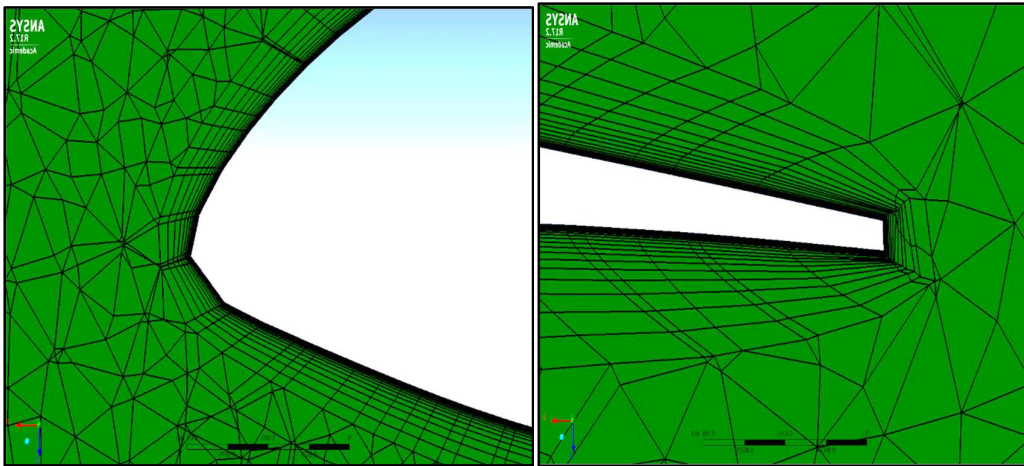


Figure 29: Details of the prismatic layers in proximity of the leading edge (left) and trailing edge (right).

3.4.2 Mesh sensitivity test

In this study, three cases of tetrahedral mesh representing coarse, medium and fine mesh have been tested (Table 4). The mesh sensitivity test has been investigated only for low Reynolds models at medium wind speed ($U_{\infty}=15$ m/s), thereafter, the selected parameters have been applied for the high Reynolds mesh. The maximum and the minimum of cells size values for the stationary domain were fixed respectively at 0.2 m and 10^{-3} m. The blade surface has been divided into 10^5 elements for all mesh tests (Figure 30).

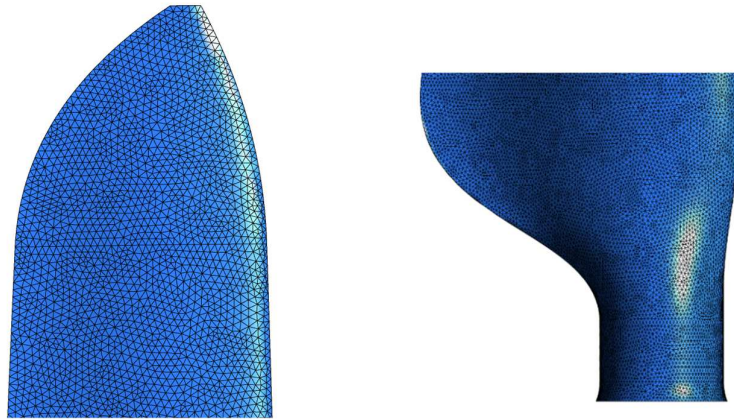


Figure 30: Details of the mesh on the blade surface at (left) tip region and (right) root region.

Table 5 presents the comparison of the power and the relative error for the three mesh cases. Figure 31 shows the comparison of normal force distribution along the blade for the three meshes. According to the table and the figure, it is clear that the medium mesh gives results closer to the fine mesh: the difference between the errors is less than 1% (see Table 5). Therefore, the medium mesh has been selected for low Reynolds models in this work.

Table 4: The three tested meshes.

	Fine	Medium	Coarse
Maximum size of rotating zone elements (m)	9.5×10^{-3}	2×10^{-2}	3.5×10^{-2}
Nodes number	12,305786	5,191504	2,314206
Elements number	63,728406	21,902364	6,295597

Table 5: Mesh sensitivity study.

Mesh case	Node Number ($\times 10^6$)	Power (kw)	Error (%)
Coarse	2.314206	12.121	14.10
Medium	5.191504	15.066	06.76
Fine	12.305786	14.912	05.67

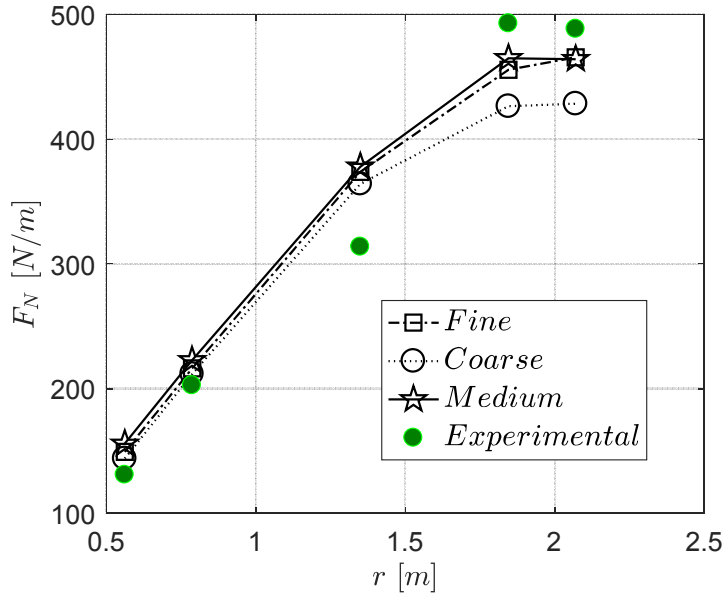


Figure 31: Low Reynolds mesh sensitivity test, comparison of normal forces along the blade for ($U_\infty = 15$ m/s) using three mesh cases.

3.4.3 Selected mesh information

The mesh selected for low Reynolds models contained approximately 5.1 million mesh elements in the one-third computational domain. The height of the first-floor mesh element was approximately 10^{-6} m, ensuring that y^+ would remain below 1 on the blade surface (see Table 6). The mesh selected for high Reynolds models contained approximately 4.1 million mesh elements. The height of the first-floor mesh element was approximately 4×10^{-5} m, which ensured that y^+ was close to 30-200 on the blade surface for applying the logarithmic wall function in this region (Figure 32 and 33).

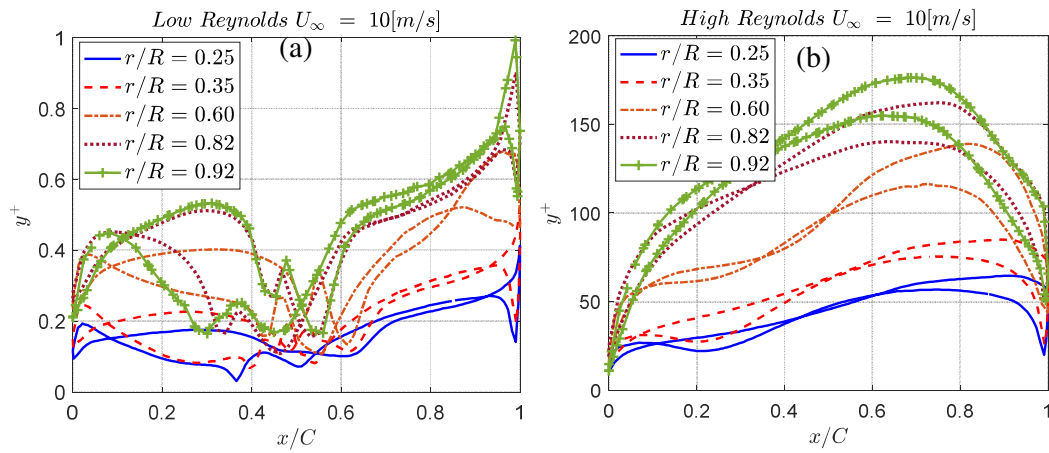


Figure 32: Distribution of y^+ at five blade sections for; (a) low Reynolds mesh and (b) high Reynolds mesh respectively.

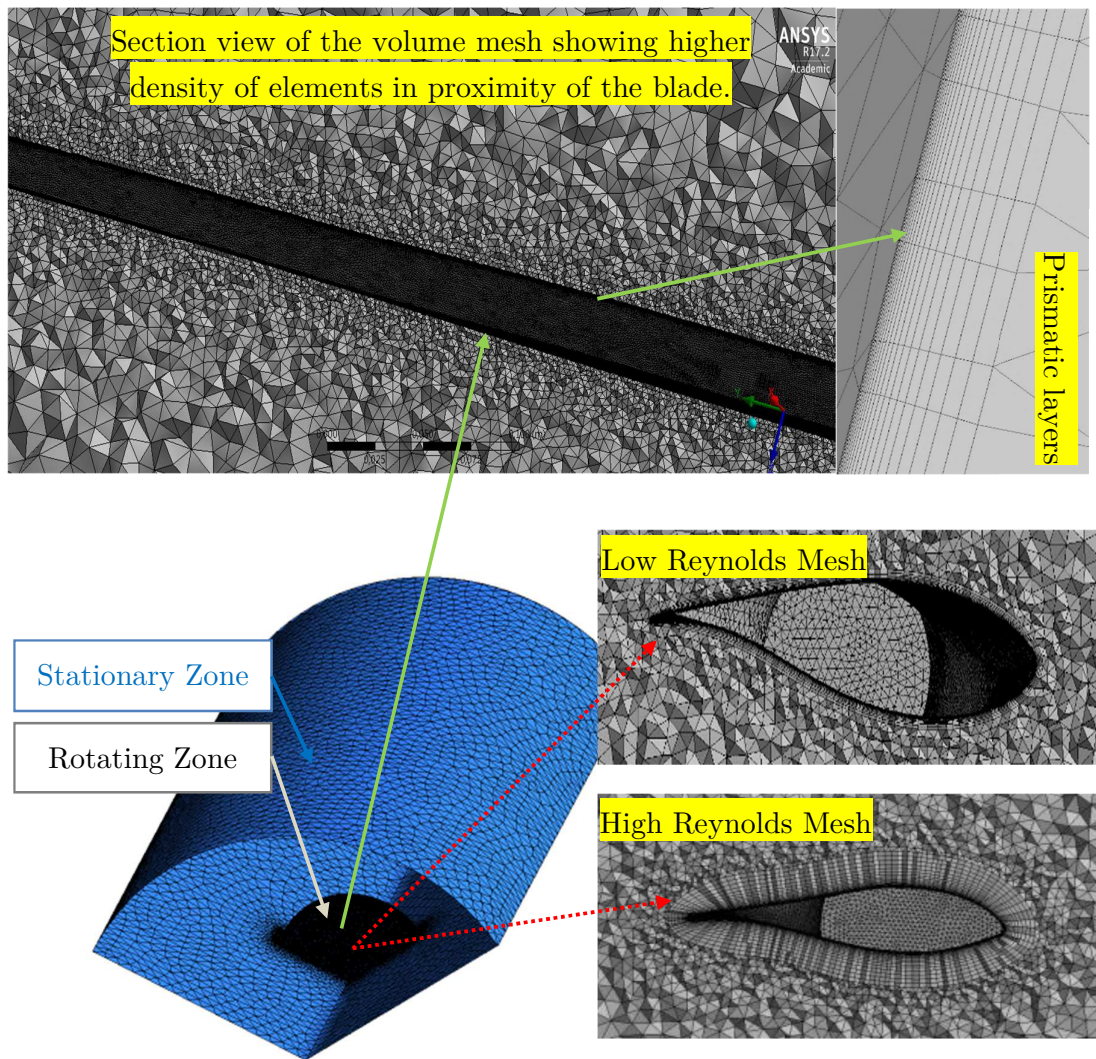


Figure 33: Details of the mesh for high and low Reynolds models.

Table 6: Detail information for low Reynolds mesh

Part	Elements	Nodes
Stationary part	-	249274
Rotating part	-	4,942230
Blade surface	-	107380
Interfaces	-	26748
Other surfaces	-	40048
Prismatic layers	-	2,077468
Total	21,902364	5,191504

3.5 Boundary conditions

Figure 34 shows the boundary conditions list used in this study.

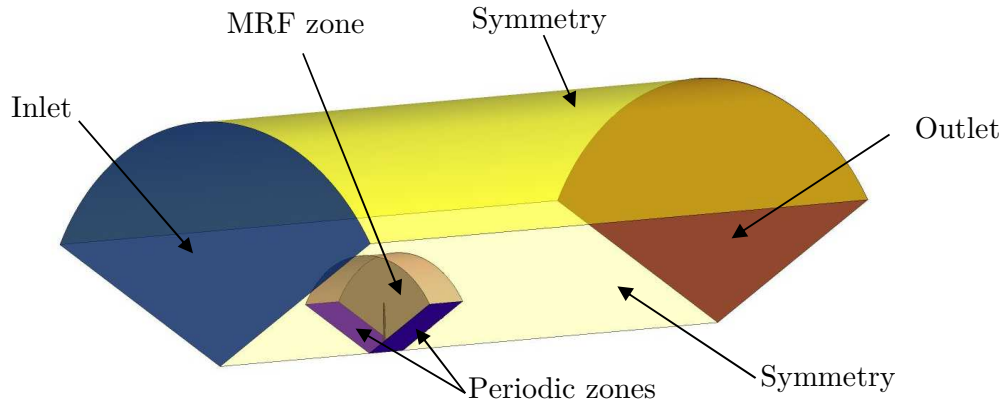


Figure 34: Boundary conditions.

3.5.1 Inlet

When treating numerically the turbulent flow around HAWTs, many boundary conditions must be defined at the inlet of the computational domain. Since the variables of the problem are the velocities and the pressure in each point of the mesh. These variables are needed to define at the inlet of the computational domain.

3.5.1.1 Velocity

In this study, a constant uniform velocity corresponding to each studied case was specified in the inlet boundary using the Cartesian coordinates system.

3.5.1.2 Pressure

In the solver, for the incompressible flows, all the pressure values to be defined in the boundary conditions (or calculated by the Navier-Stokes equations) are represented by the gauge pressure, which is the difference between the absolute pressure and the operating pressure. Therefore, in this study, the obvious choice was to put the value equal to zero so that the pressure at the inlet would be equal to the atmospheric operating pressure (operating pressure corresponding to each case was used).

3.5.1.3 Turbulence quantities

In this study, theoretical/empirical correlations have been used to estimate the turbulence quantities in the inlet boundary for each turbulence model. These correlations are related to more convenient quantities such as: turbulence intensity (I) and turbulence length scale (L), where the turbulence intensity was defined as a low value $I_\infty = 0.2\%$ [215]. The turbulence length scale can be estimated from the boundary layer thickness, δ_{99} , by: $0.4 \times \delta_{99}$, as reported in the reference [173].

For the Spalart-Allmaras model, the turbulent viscosity $\tilde{\nu}$ can be estimated as [190]:

$$\tilde{\nu}_\infty = \sqrt{\frac{3}{2}} U_\infty I_\infty L \quad (156)$$

For the k - ϵ models, the turbulent kinetic energy and its dissipation rate are respectively calculated as follows [201, 222]:

$$k_\infty = \frac{3}{2} (U_\infty I_\infty)^2 \quad (157)$$

$$\epsilon_\infty = \frac{C_\mu^{3/4} k_\infty^{3/2}}{L} \quad (158)$$

For the k - ω models, the k is calculated by the same manner as in the k - ϵ models, and the specified dissipation rate ω was estimated by:

$$\omega_\infty = \frac{k_\infty^{1/2}}{C_\mu^{3/4} L} \quad (159)$$

For the k - kl - ω transitional model, the k and ω are calculated by equation (157) and equation (159) respectively. For the laminar kinetic energy kl , a recommended value of $10^{-6} (m^2/s^2)$ for external flows has been used [173].

For the transitional γ - Re_θ model, the intermittency the intermittency is equal to one at the inlet according to the reference [203, 204].

For the RSM model, the Reynolds stresses tensor is defined by [173, 199]:

$$\overline{u_i'^2} = \frac{2}{3}k \quad i = 1,2,3 \quad (160)$$

and

$$\overline{u_i' u_j'} = 0.0 \quad (161)$$

3.5.2 Outlet

In the outlet boundary, static pressure was imposed and was equal to the ambient pressure of the wind tunnel corresponding to each case. All other flow quantities are extrapolated from the interior.

3.5.3 Near wall treatment

3.5.3.1 Velocity

Turbulent flows are significantly affected by the presence of walls. Numerous experiments have shown that the near-wall region can be largely subdivided into three layers [223, 224]. In the innermost layer, called the “viscous sublayer”, the flow is almost laminar, and the (molecular) viscosity plays a dominant role in momentum and heat or mass transfer. In the outer layer, called the fully-turbulent layer, turbulence plays a major role. Finally, there is an interim region between the viscous sublayer and the fully turbulent layer where the effects of molecular viscosity and turbulence are equally important. Figure 35 illustrates these subdivisions of the near-wall region, plotted in semi-log coordinates.

Traditionally, there are two approaches to applying RANS turbulence models in cases of flow around wind turbine blades: either via full near-wall resolution (low Reynolds models) using a sufficient fine mesh in the near wall to capture the boundary layer and the point of separation, or via a wall function approach that avoids near-wall (viscous sublayer and buffer layer) resolution. This technique is called the high Reynolds model approach, and its main advantage is that it reduces calculation time by reducing computational mesh size [7, 70].

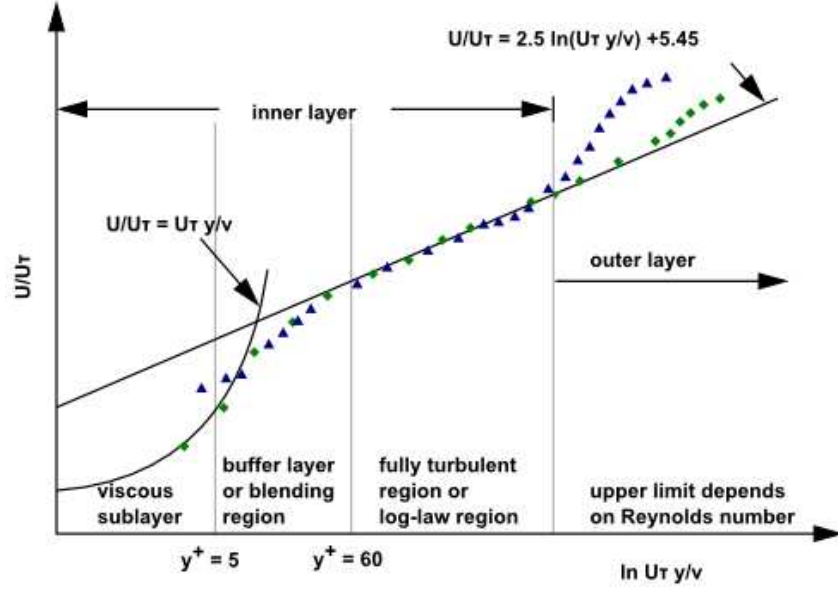


Figure 35: Law of the wall and concept of the logarithmic wall function [176].

In this work, the non-slip condition ($U_p = 0$) has been applied for low Reynolds models and the standard wall function (Equation 162) has been used for high Reynolds models:

$$\frac{U_p C_\mu^{1/4} k_p^{1/2}}{\tau_w \rho} = \frac{1}{\kappa} \ln \left(E \frac{\rho C_\mu^{1/4} k_p^{1/2} y_p}{\mu} \right) \quad (162)$$

where U_p and y_p are the velocity and the height at the near-wall node (P). k_p denotes the turbulent kinetic energy at the near-wall node.

3.5.3.2 Turbulence quantities

The turbulent kinetic energy k at the wall is calculated from:

$$\frac{\partial k}{\partial n} = 0 \quad (163)$$

where n is the local coordinate normal to the wall.

The dissipation rate ϵ at the wall is given by:

$$\epsilon_p = \frac{C_\mu^{3/4} k_p^{3/2}}{\kappa y_p} \quad (164)$$

The specific dissipation rate ω is:

$$\omega_p = \frac{6\rho(U_\tau^2)}{\beta_i(y^{+2})} \quad (165)$$

For the k - kl - ω model, both laminar and turbulent kinetic energy are zero at the wall ($k_p = kl_p = 0$), and the boundary condition for ω is:

$$\frac{\partial \omega}{\partial n} = 0 \tag{166}$$

3.5.4 Periodic conditions

Since the wind turbine rotor rotates at a constant angular velocity thus presenting a periodically repeating nature; the software allows applying periodic boundary conditions to specific surfaces as shown in Figure 36 giving the great advantage of reducing the size of the computational domain.

Using the periodic conditions, all the flow variables are calculated as follows:

$$\vec{\phi}(r_i, \theta) = \vec{\phi}(r_i, \theta_1 - 120^\circ n); \quad n = 1, 2, 3 \tag{167}$$

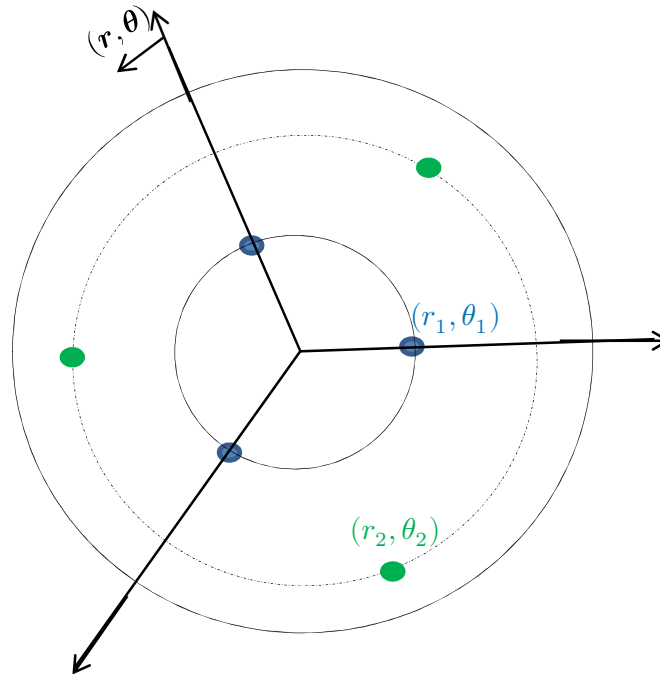


Figure 36: The periodic conditions.

3.5.5 Symmetry

The “Symmetry” boundary condition assumes a zero flux of all quantities across a symmetry boundary. There is no convective flux across a symmetry plane: the normal velocity component at the symmetry plane is thus zero. There is no diffusion flux across a symmetry plane: the normal gradients of all flow variables are thus zero at the

symmetry plane. The symmetry boundary condition can therefore be summarized as follows [176]:

- (i) zero normal velocity at a symmetry plane ($u_{normal} = 0$);
- (ii) zero normal gradients of all variables at a symmetry plane ($\frac{\partial}{\partial n}(u, p, k, \dots) = 0$).

3.5.6 Interfaces

In this study, an interface technique was applied to separate rotating parts from stationary parts. Because the velocities in both the rotating and stationary parts were stored in the absolute frame, velocities were determined in the interface between two domains based on absolute velocity; scalar quantities such as density and pressure were calculated locally, from adjacent cells.

3.5.7 Moving Reference Frame (MRF)

The Multiple Reference Frame (MRF) model [225] is the simplest model used for modeling flow field over rotating objects; this steady-state approach is based on the additional terms in the momentum equations, which lead to an increase in acceleration of fluid resulting from the blades' rotation [7].

The axis of rotation, as illustrated in Figure 37, is defined by a unit direction vector \vec{a} such that:

$$\vec{\omega} = \omega \vec{a} \tag{168}$$

The fluid velocities can be transformed from the stationary frame to the rotating frame using the following relation:

$$\vec{V}_r = \vec{V} - \vec{U}_r \tag{169}$$

where

$$\vec{U}_r = \vec{V}_t + \vec{\omega} \times \vec{r} \tag{170}$$

Based on the absolute velocity formulation, the governing equations of fluid flow (Navier-Stokes) within the framework of MRF can be written as follows:

$$\nabla \cdot \rho \vec{V}_r = 0 \tag{171}$$

$$\nabla \cdot (\rho \vec{V}_r \vec{V}) + \rho [\vec{\omega} \times \vec{V}] = -\nabla p + \nabla \bar{\tau} \quad (172)$$

where $[\vec{\omega} \times \vec{V}]$ represents the Coriolis and centripetal accelerations.

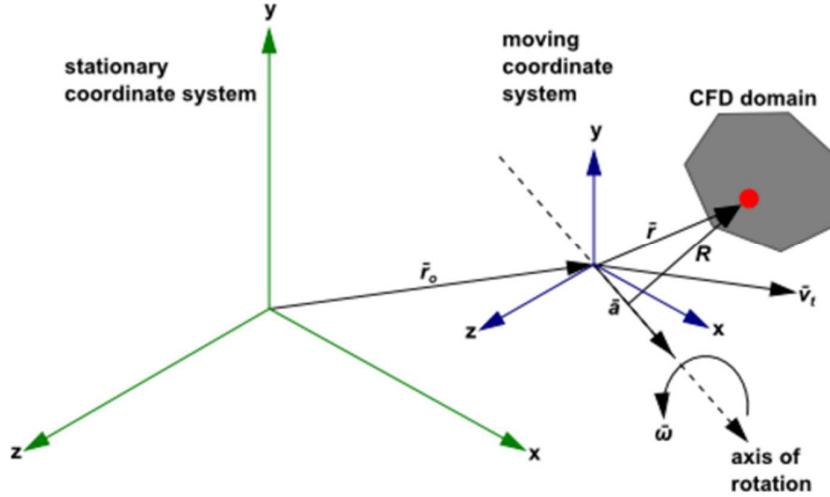


Figure 37: Stationary and Moving Reference Frame (MRF) [173].

3.6 Numerical resolution

This section focuses on two points used in the numerical methodology: (i) the numerical method used to solve the particles motion equations, and (ii) the methodology used for coupling between the two phases: continuous and dispersed phase.

3.6.1.1 Integration of particle motion equation

The particle motion equation presented in the end of previous chapter (Equation 144) can be cast into the following general form:

$$\frac{\partial u_p}{\partial t} = F_D(u - u_p) + F_A \quad (173)$$

where the term F_A includes accelerations due to all other forces except drag force.

This ordinary differential equation can be solved for constant values of u , F_D and F_A using four different methods as follows:

- (i) The equation (173) can be solved by analytical integration. For the particle velocity at the new location u_p^{n+1} we get:

$$u_p^{n+1} = u^n + \exp(-F_D \Delta t) (u_p^n - u^n) - (F_A/F_D)(\exp(-F_D \Delta t) - 1) \quad (174)$$

where u_p^n is the old particle location and u^n is the old mean fluid velocity.

(ii) The equation (173) can be solved using numerical discretization schemes as:

$$u_p^{n+1} = \frac{u_p^n + \Delta t(F_A + F_D u^n)}{1 + F_D \Delta t} \quad (175)$$

(iii) The equation (173) can be solved using a trapezoidal discretization as:

$$\frac{u_p^{n+1} - u_p^n}{\Delta t} = F_D(u^* - u_p^*) \quad (176)$$

The average values u^* and u_p^* are calculated from:

$$u_p^* = \frac{1}{2}(u_p^n + u_p^{n+1}) \quad (177)$$

$$u^* = \frac{1}{2}(u^n + u^{n+1}) \quad (178)$$

$$u^{n+1} = u^n + \Delta t u_p^* \cdot \nabla u^n \quad (179)$$

Finally, the particle velocity at the new location u_p^{n+1} is calculated by:

$$u_p^{n+1} = \frac{u_p^n \left(1 - \frac{1}{2} F_D \Delta t\right) + F_D \Delta t \left(u^n + \frac{1}{2} \Delta t u_p^n \cdot \nabla u^n\right) + \Delta t F_A^n}{1 + \frac{1}{2} F_D \Delta t} \quad (180)$$

(iv) The equation (173) can be solved using a modified Runge-Kutta scheme [226].

In this scheme, the ordinary differential equations can be considered as vectors, where the left-hand side is the derivative \vec{y}' and the right-hand side is an arbitrary function $\vec{f}(t, \vec{y})$.

$$\vec{y}' = \vec{f}(t, \vec{y}) \quad (181)$$

$$\vec{y}^{n+1} = \vec{y}^n + c_1 \vec{k}_1 + c_2 \vec{k}_2 + c_3 \vec{k}_3 + c_4 \vec{k}_4 + c_5 \vec{k}_5 + c_6 \vec{k}_6 \quad (182)$$

with

$$\vec{k}_1 = \Delta t \vec{f}(t, \vec{y}^n) \quad (183)$$

$$\vec{k}_2 = \Delta t \vec{f}(t + a_2 \Delta t, \vec{y}^n + b_{21} \vec{k}_1) \quad (184)$$

$$\vec{k}_3 = \Delta t \vec{f}(t + a_3 \Delta t, \vec{y}^n + b_{31} \vec{k}_1 + b_{32} \vec{k}_2) \quad (185)$$

$$\vec{k}_4 = \Delta t \vec{f}(t + a_4 \Delta t, \vec{y}^n + b_{41} \vec{k}_1 + b_{42} \vec{k}_2 + b_{43} \vec{k}_3) \quad (186)$$

$$\vec{k}_5 = \Delta t \vec{f}(t + a_5 \Delta t, \vec{y}^n + b_{51} \vec{k}_1 + b_{52} \vec{k}_2 + b_{53} \vec{k}_3 + b_{54} \vec{k}_4) \quad (187)$$

$$\vec{k}_6 = \Delta t \vec{f}(t + a_6 \Delta t, \vec{y}^n + b_{61} \vec{k}_1 + b_{62} \vec{k}_2 + b_{63} \vec{k}_3 + b_{64} \vec{k}_4 + b_{65} \vec{k}_5) \quad (188)$$

The coefficients $a_2 \dots a_6$, $b_{21} \dots b_{65}$, and $c_1 \dots c_6$ are taken from Cash and Karp [226].

In this study, the comparison between these four methods was performed. It has been shown that two methods gave very similar results (Trapezoidal and Runge-Kutta). The Runge-Kutta gives the solutions in less calculation time. The both analytic and implicit schemes were not converged especially for high concentrations. Therefore, the Runge-Kutta scheme has been used in this work.

3.6.1.2 Coupling between phases

The Eulerian-Lagrangian model used for its original formulation was developed to predict particle trajectories from the characteristics of the fluid phase. It is clear in the particles motion equation (173) that the fluid velocity is included in the particle balance equation, so that the continuous phase can influence the discrete phase. This type of coupling is called *one-way coupling*. In this approach, the discrete phase does not influence the continuous phase. However, in this study, it is interesting to see the influence of the continuous phase by the particles. For this reason, we included the influence of the particles represented by the sum of force change as a source term in the continuous phase. This type of coupling is called *two-way coupling*, see Figure 38. Here, the model developed by Crowe et al [227] has been used for coupling between the phases. This model is implemented in the new versions of the solver.

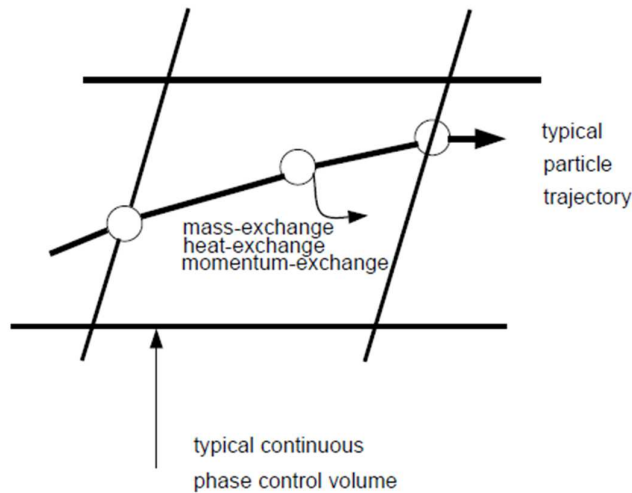


Figure 38: Momentum Transfer between the discrete and continuous phases.

The momentum transfer from the continuous phase to the discrete phase is calculated by examining the change in momentum of a particle as it passes through each control volume. This momentum change is computed as [173, 227]:

$$F = \sum \left(\frac{18\mu C_D Re}{24\rho_p d_p^2} (u - u_p) + \frac{\vec{g}(\rho_p - \rho)}{\rho_p} + F_{MRF} \right) \dot{m}_p \Delta t \quad (189)$$

where \dot{m}_p is the mass flow rate of the particles and Δt is the time step.

This momentum exchange appears as a momentum sink in the continuous phase momentum balance in any subsequent calculations of the continuous phase flow field.

The procedure of the coupling used, in this study, can be summarized as follows:

1. Solve the continuous phase flow field (prior to introduction of the discrete phase).
2. Introduce the discrete phase by calculating the particle trajectories for each discrete phase injection.
3. Recalculate the continuous phase flow, using the interphase exchange of momentum and mass determined during the previous particle calculation.
4. Recalculate the discrete phase trajectories in the modified continuous phase flow field.
5. Repeat the previous two steps until a converged solution is achieved in which both the continuous phase flow field and the discrete phase particle trajectories are unchanged with each additional calculation.

3.7 High Performance Computing (HPC)

Computational Fluid Dynamics (CFD) problems are among the most demanding scientific computing problems in terms of the computational resources they require. Today, with the development of computing resources, it is possible to use multicore computers exploiting the so-called parallel processing to perform the CFD simulations using high performance computing supercomputers (or clusters) [228]. This technique can reduce the computational time importantly compared with single computer computing and it allows to treating a more complex phenomenon.

In this technique, the computational domain is divided into a number of smaller subdomains. Each subdomain is treated by a separate processor (also known as cores

or CPU), and finally, the solutions of the full domain can get by a connection with processors. In the literature, there are two fundamental types of parallel processing: (i) a single computer with multiple internal processors, named as a shared-memory parallel processing; (ii) a set of computers interconnected through a network, named as a distributed memory parallel processing [229].

In this work, all the simulations have been performed using the Guillimin cluster, which is one of the largest high-performance computing supercomputers in Canada, (Figure 39). This cluster is installed in McGill HPC (McGill University's center for High-Performance Computing). It comprises more than 21000 processing cores running on the latest Intel Sandy Bridge and Westmere processors.

Because the server is based on Linux environment and it is not possible to execute the interface of the CFD solver, text command files based on Linux batch have been developed to launch and control the simulations in the server. The geometry and the mesh of computational domain were performed using a parallel PC with 64 GB RAM and 6 x 3.31 GHz CPU. Finally, the results were treated using CFD-Post processing for the contours and the MATLAB software for curves.



Figure 39: High performance computing Guillimin cluster [230].

Chapter 4

Results and discussion: Comparison between different turbulence models

In this chapter, the results of the CFD simulations will be presented. This study's main contribution is in establishing which RANS models can produce quantitatively reliable numerical predictions of turbulent flow around wind turbine rotors. The CFD results under wide range of flow conditions varied from attached to separated flow are compared with the experimental data (New MEXICO measurements) and they have been analyzed with respect to different parameters: the pressure on different spanwise sections, aerodynamic forces, torque, thrust and the mechanical power. In addition, different velocities in the near wake have been investigated. Ten different RANS turbulence models were investigated: Spalart-Allmaras [190]; Standard $k-\epsilon$ [191]; $k-\epsilon$ RNG [192]; $k-\epsilon$ Realizable [193]; Standard $k-\omega$ [186]; $k-\omega$ BSL [194]; $k-\omega$ SST [194]; $k-kl-\omega$ [195]; $\gamma_{\text{Re}\theta}$ [196] and *RSM-LPS* [197].

4.1 Operating conditions

In this study, steady simulations were carried out based on the numerical resolution of the Navier-Stokes equations using a finite-volume method based on a cell-centered scheme using the ANSYS Fluent 17.2 CFD solver. The simulations cover three no-yawed flow conditions, where flow over the MEXICO rotor varies from fully attached to massively separated. The operating flow conditions for the three cases investigated in this study are shown in Table 7. It should be mentioned here that both standard $k-\omega$ and $k-\omega$ BSL models are given overpredictions (in which the error exceeded 80% for all cases, see [Appendix B](#)), therefore, their results are not presented in this section.

Table 7: Operating conditions of the new MEXICO measurements.

<i>Case</i>	<i>TSR</i>	U_{∞} (m/s)	ρ (kg/m ³)	p_{∞} (pa)
1	10	10.05	1.197	101398
2	6.7	15.06	1.191	101345
3	4	24.05	1.195	101407

4.2 Attached and separated flow

Figure 40 shows the streamlines in the suction side of the blade, simulated at three cases ($U_{\infty}=10, 15$ and 24 m/s) using the $k-\epsilon$ (RNG) turbulence model. At the first wind speed, ($U_{\infty}=10$ m/s), we see that the flow is attached to the whole blade at this low velocity; however, a slight radial component appearing at the root of the blade is noticeable, likely due to vortex shedding in this region (Figure 41). In the second case, ($U_{\infty}=15$ m/s), this separated component increased somewhat in the root part of the blade, especially along its leading edge; the flow remained attached in the blade. At the wind speed of 24 m/s, separations of flow appeared on the suction side of the entire blade, from its leading to its trailing edges, unlike what we observed in the first and second cases, where the separation zones did not exceed the $0.25xR$ blade span. The separation zone rose higher than the $0.92xR$ region in the third case, reflecting an increased wind speed effect on boundary layer separation.

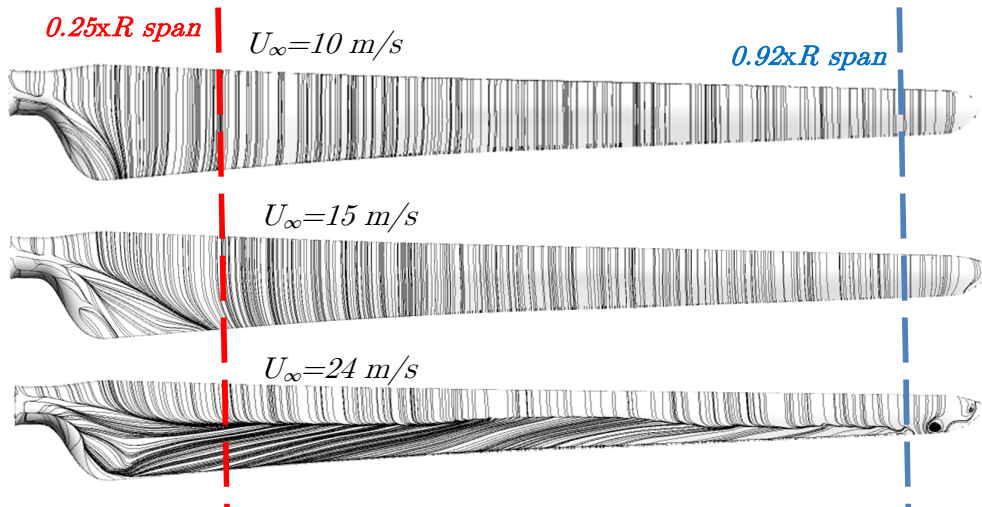


Figure 40: Limiting streamlines on the suction side of the MEXICO blade showing the attached and separated flow for three studied cases.

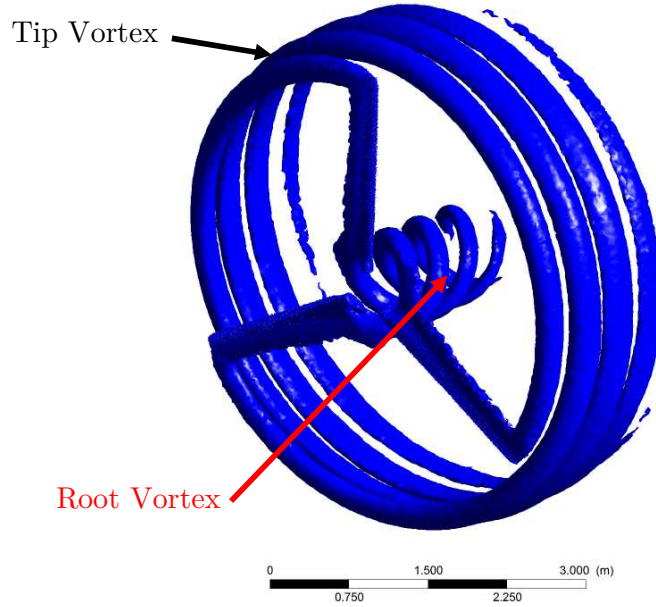


Figure 41: Development of the vortex in the downstream behind the rotor.

4.3 Pressure distribution

The pressure distribution in the blade surface is an important factor in the aerodynamics of wind turbines. Because all the rotor performances (normal and tangential forces, thrust, torque and power) are calculated by the integration of the pressure distribution along the blade surface. In the aerodynamics of wind turbines, the pressure distribution is usually represented by the pressure coefficient, which is calculated as follows:

$$C_p = \frac{p - p_\infty}{0.5\rho(U_\infty^2 + (\Omega r)^2)} \quad (190)$$

where: p and p_∞ are the static pressure at the blade surface and the static pressure in the freestream, ρ is the fluid density, U_∞ is the freestream wind speed, Ω is the rotor rotational speed and r is the local radius of the blade.

Distribution of measured and calculated local surface pressure coefficients surrounding the five spanwise sections of the blade were compared, as shown in Figures 43, 44, and 45. For the first case investigated (Figure 34), $U_\infty=10$ m/s which was categorized as having low wind speed. Flow was mostly attached and pressure distribution for all the turbulence models showed very good agreement, with the exception of the inboard sections at low wind speed, where we know from [75, 215] that the pressure sensors'

range is insufficient for resolving the actual physics. This reflects the ability of both low and high Reynolds RANS turbulence models to predict attached flows.

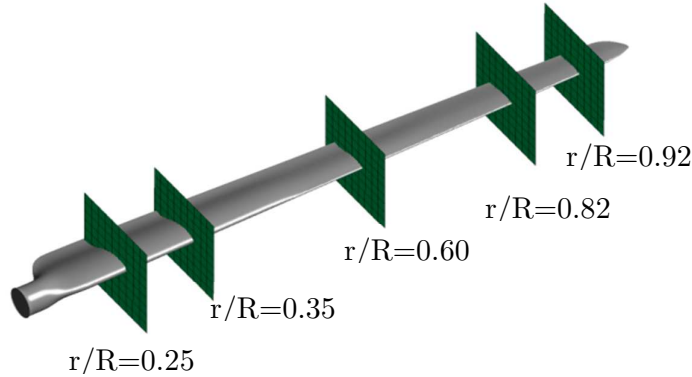


Figure 42: Five spanwise sections of the MEXICO blade.

In the second case investigated, $U_\infty=15$ m/s, which has been categorized as the onset of stall (Figure 44). The difference between the models begins to appear. Good agreement with the experimental data was observed for all turbulence models on the root part of the blade (when $r/R < 0.6$), with the exception the standard $k-\epsilon$ model which underestimated the pressure in the extrados parts especially close to the leading edge of the DU profiles. On the outer part of the blade ($r/R \geq 0.6$) underestimations of different low and high Reynolds models ($RSM, \gamma_{Re_\theta}, k-\omega$ SST, standard $k-\epsilon$) were observed on the extrados where the flow is mostly separated. However, different models are given good agreement with the experimental (such as, $k-\epsilon$ realizable, $k-\epsilon$ RNG, $k-kl-\omega$ and Spalart-Allmaras models).

Figure 45 shows the pressure coefficient distributions in the last case investigated, $U_\infty=24$ m/s; these were classified as separated flow conditions. The difference between the models increases from root to tip of the blade. For the first blade sections ($r/R = 0.25-0.35$), good agreements were observed for the most turbulence models. However, from the section $r/R = 0.6$, the difficulty of capturing the separation for different models (especially for $RSM, \gamma_{Re_\theta}, k-\omega$ SST, standard $k-\epsilon$ models) are very clear in the extrados surfaces (especially at the root of the blade at RISØ and NACA regions). It has been shown that the RSM high Reynolds model gives poor predictions in all cases. The most accurate results are given by the transitional $k-kl-\omega$ model. This reflects the ability of this transitional model to well predict the separated flows at higher wind speeds.

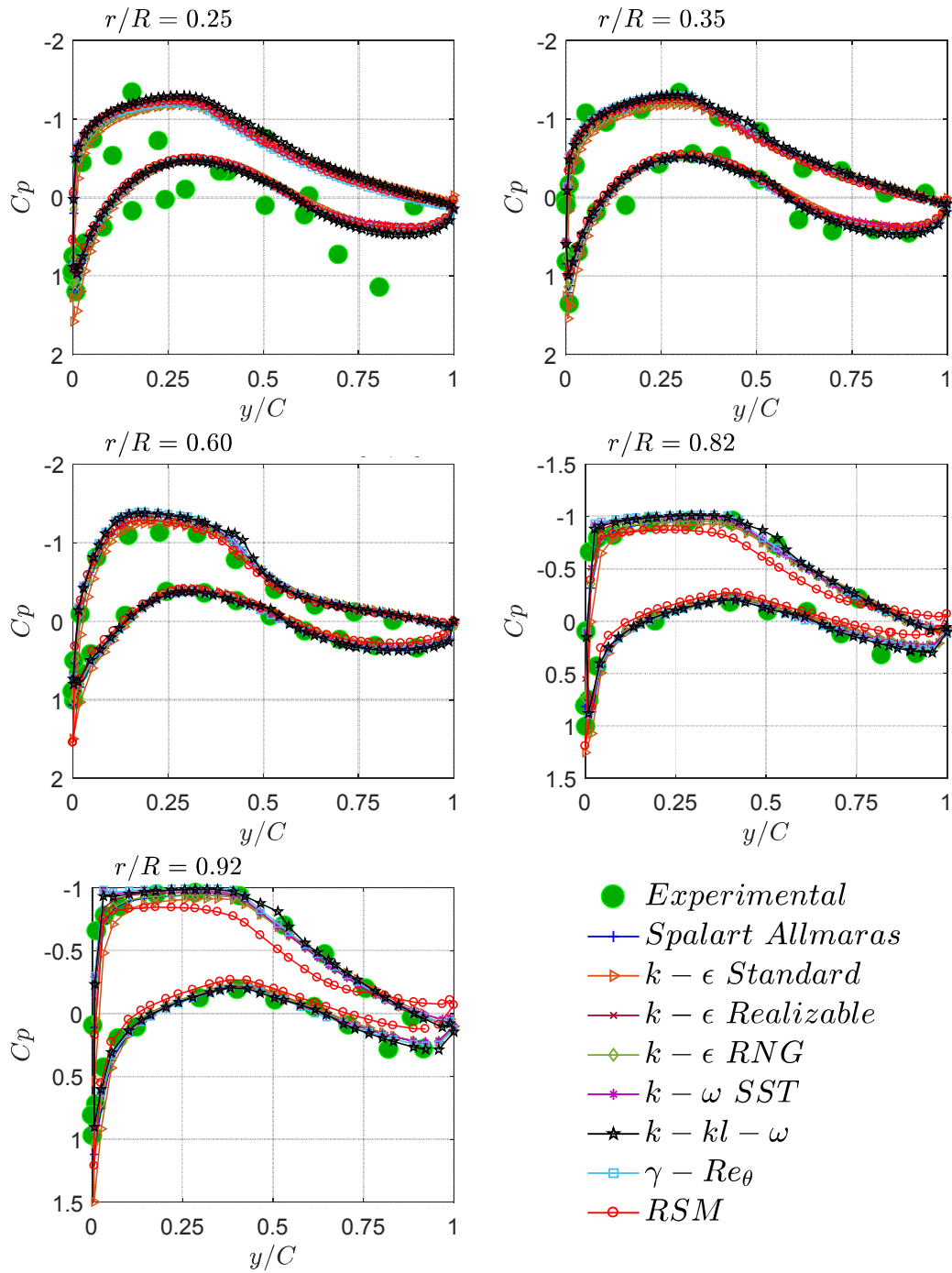


Figure 43: Comparison between CFD results and experimental pressure coefficient distributions at five spanwise sections, case 1 ($U_\infty=10$ m/s).

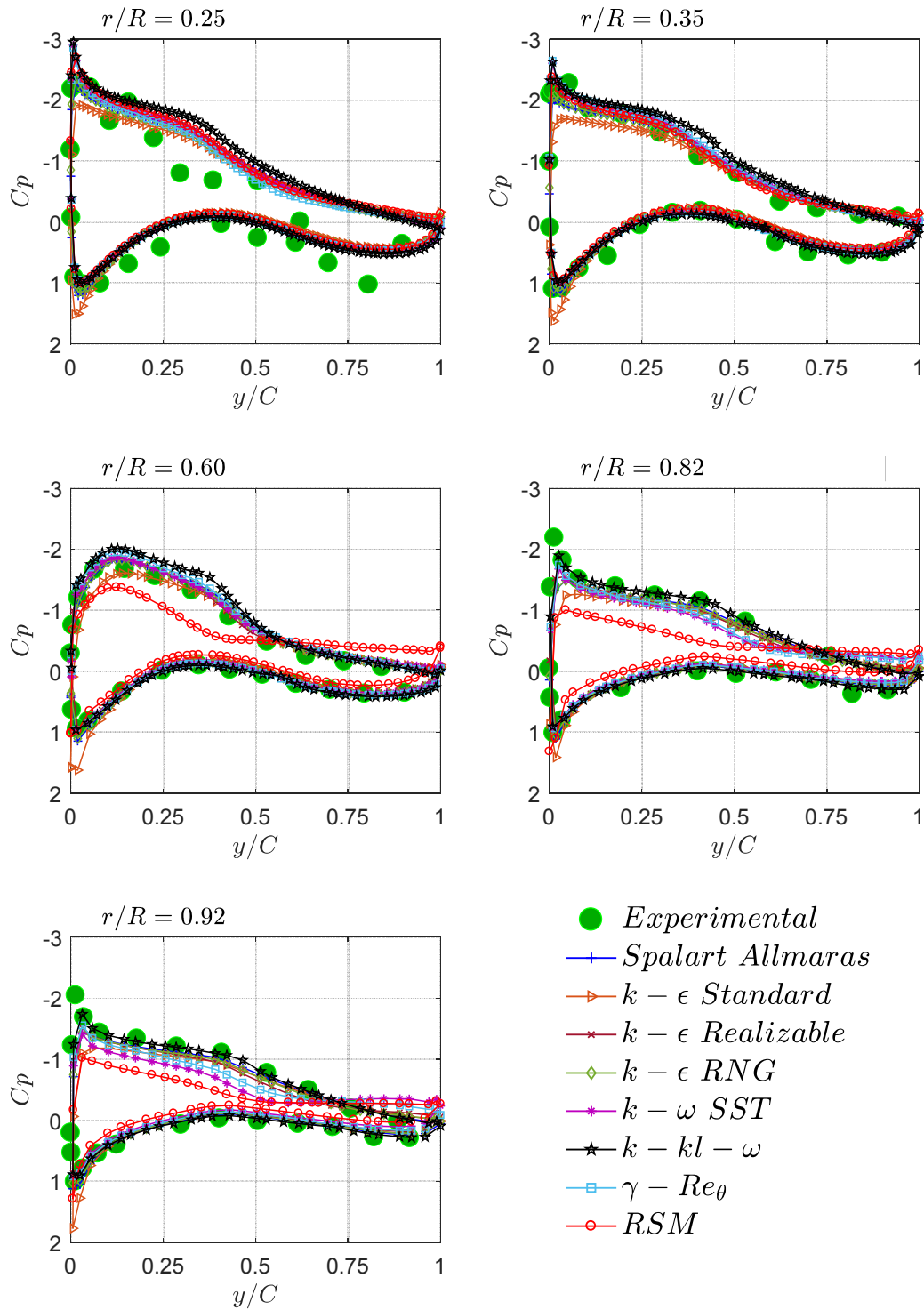


Figure 44: Comparison between CFD results and experimental pressure coefficient distributions at five spanwise sections, case 2 ($U_\infty=15$ m/s).

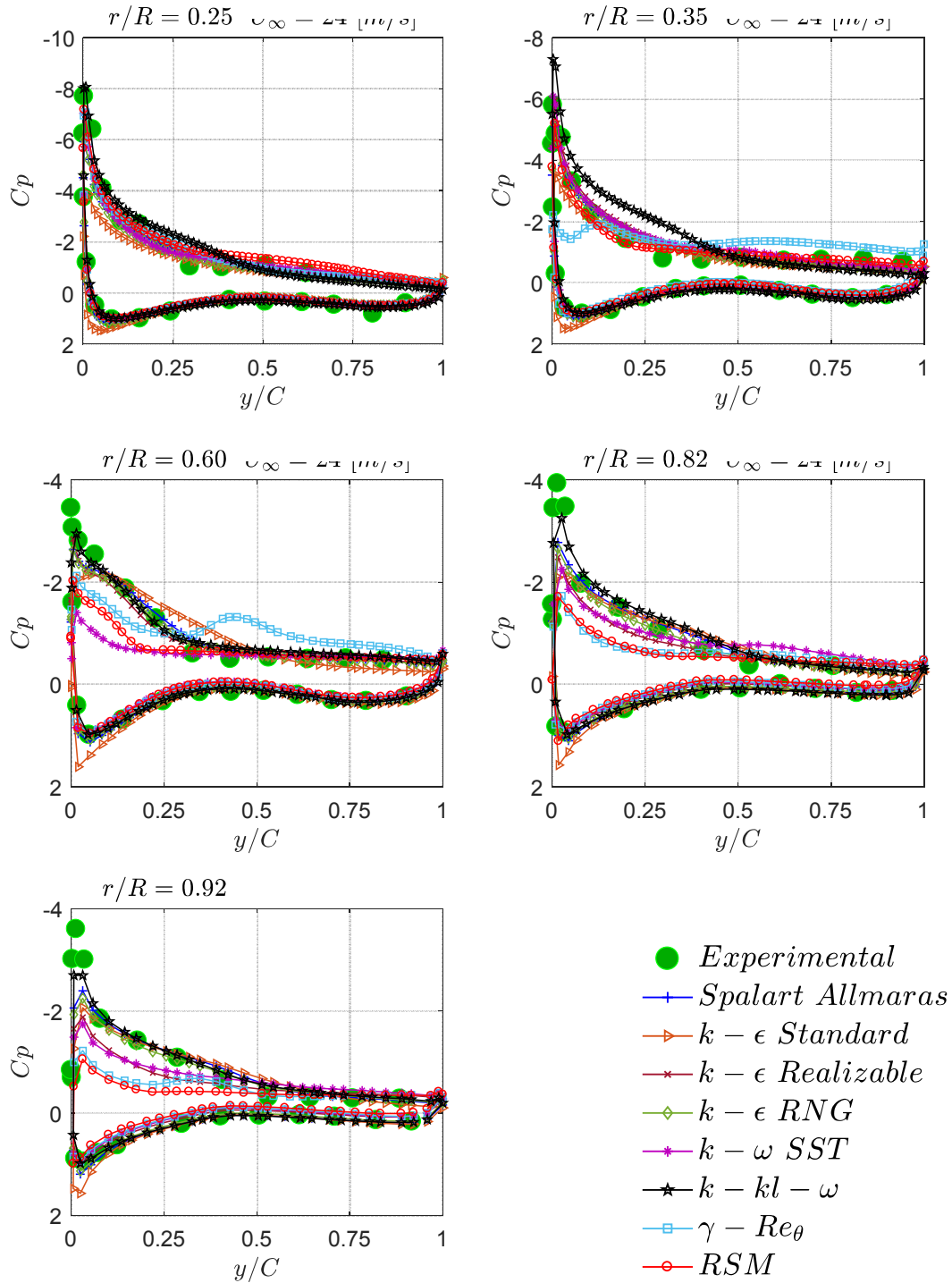


Figure 45: Comparison between CFD results and experimental pressure coefficient distributions at five spanwise sections, case 3 ($U_\infty=24$ m/s).

4.4 Flow visualisation

4.4.1 Flow path-lines

In order to further understand the characteristics of the flow at different wind speeds, Figure 46 shows the flow path-lines and the static pressure contours, at five radial span sections of the blade, simulated using the transitional $k-kl-\omega$ turbulence model. It can be seen that, from Figure 46, the angle of attack increases in each case from tip to root of the blade due to the augmentation of twist angle. This angle increases also due to the augmentation of incoming wind speed. It can be seen also from the Figure 46 that a strong separation appears at high wind speed ($U_\infty=24$ m/s) in upper sections of airfoils (extrados), especially at the trailing edge of airfoils, where the flow remains attached in the lower surface (intrados) of the blade. This explains why most of turbulence models were well predicted the pressure in the lower surface and the great difference between models at the upper surface of the blade; the prediction of the RANS models decreases with the increase of the flow separation.

4.4.2 Pressure contours

Looking now at the pressure coefficient contours presented in Figure 46, it can be seen that the pressure coefficient on the lower surface (intrados) is higher than the pressure coefficient on the upper surface (extrados) for all cases. This difference of pressure can generate a force in the normal direction of the blade surface, which leads to the drag force on the wind turbine and also, due to the blade angle of attack, a force in the circumferential direction, which causes to the blade rotation and power generation. This difference of pressure is directly related to the angle of attack; the difference in pressure increases very rapidly, going from the root towards the tip of the blade due to the increase of the angle of attack. In addition, at the same suction of the blade, the pressure difference increases with the increase of wind speed.

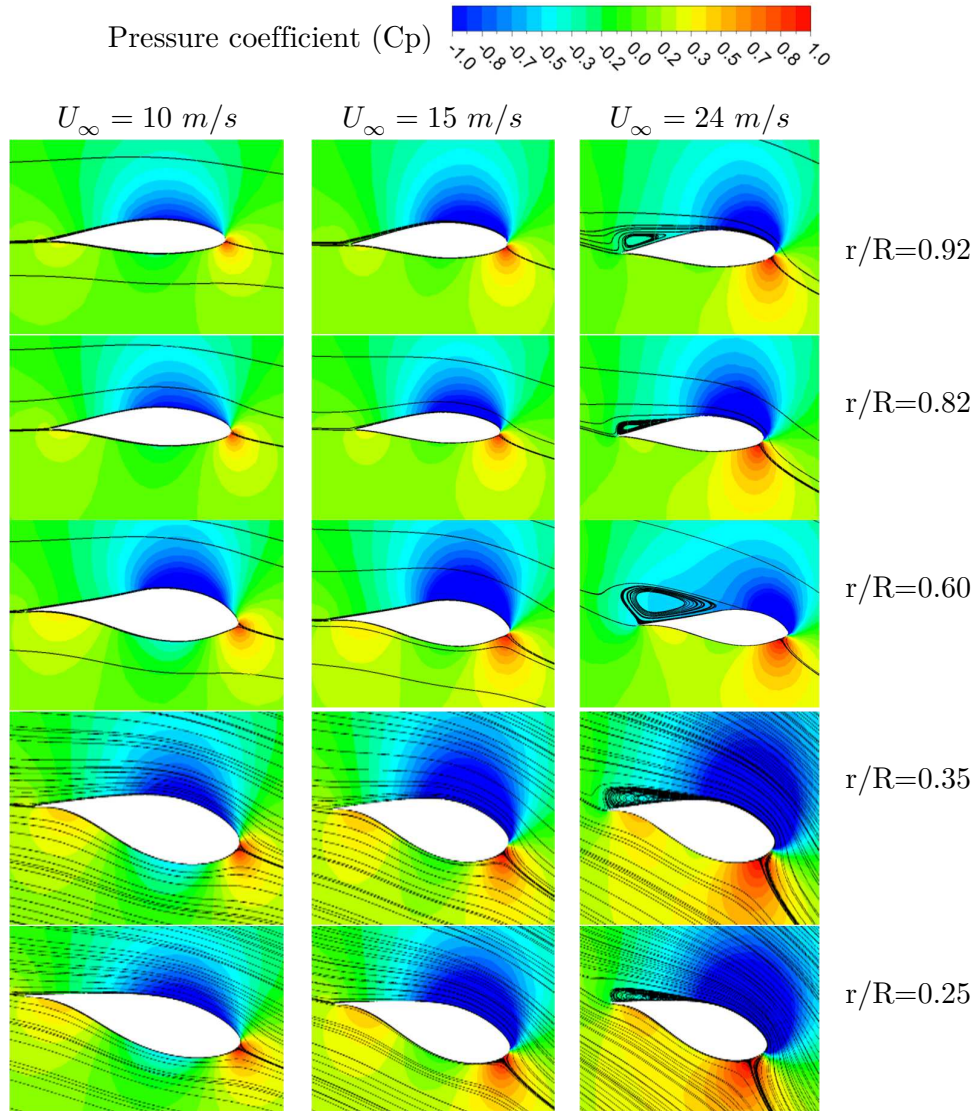


Figure 46: Pressure coefficient contours and streamlines at five span-wise sections normal to the blade surface.

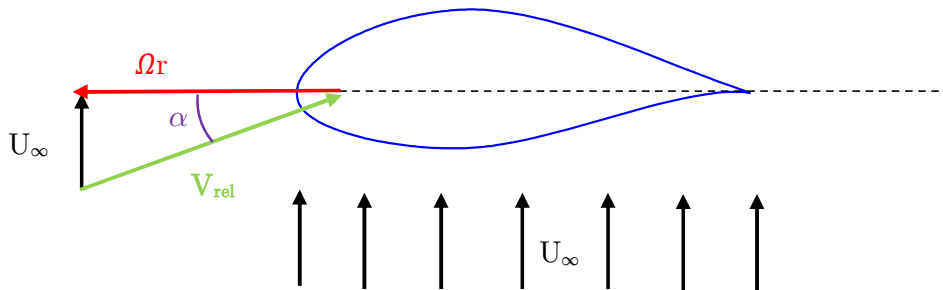


Figure 47: Schematic of velocities and angle of attack on a blade airfoil.

4.5 Aerodynamic loads

To examine the ability of turbulence models on predicting the aerodynamic performance of the rotor, the CFD computations of low and high Reynolds models were compared to the measured data, with respect to integral loads. The loads, in both the experiment and in computations, were derived from the five sectional pressure distributions by integration (as presented in Figure 42).

Because viscous friction contributions are not available in the experiment, friction is not included in the load determination from the CFD computations; in this case, the normal and tangential forces are calculated respectively from pressure on the upper and lower airfoil surface by:

$$F_N = - \int_{LE}^{TE} P_u dx_u + \int_{LE}^{TE} P_l dx_l \quad (191)$$

$$F_T = \int_{LE}^{TE} P_u dy_u - \int_{LE}^{TE} P_l dy_l \quad (192)$$

4.5.1 Normal force

The comparison of the distribution of averaged normal and tangential forces along the blade is presented in Figure 48. Looking firstly at the normal forces, we can see that the normal force, in the experimental, increases from the root to the tip of the blade by a linear relation. This increase is due to the fast variation of airfoil characteristics (shape, twist and chord). In addition, the normal forces also increase with the increase of wind speed due to the augmentation of pressure difference between upper and lower sections of the blade as shown numerically in Figure 46.

The comparison of normal forces between the turbulence models presented in Figure 48 shows that for low wind speed, where the flow is attached, good quantitative agreements for all models have been found. The most accurate models for this wind speed are the low Reynolds models: $k-\omega$ SST, γ_{Re_0} and $k-kl-\omega$.

The Spalart-Allmaras model and the all tested models of the $k-\epsilon$ have given good agreement with the measurements. However, a slight deviation at the tip of the blade was observed. It has also been shown that the *RSM* high Reynolds turbulence model gives an underprediction at the tip part of the blade.

With the increase in the wind speed, the difference between turbulence models began to appear. At the medium wind speed ($U_\infty=15$ m/s), most turbulence models give great deviation from the medium of the blade up to the tip ($r/R \geq 0.6$). However, at the root part of the blade, all turbulence models give a good prediction. The most accurate model that gave a good agreement with the experimental at the root as well as at the tip parts is the transitional $k-kl-\omega$ low Reynolds model.

At high wind speed, ($U_\infty=24$ m/s), where the flow is mostly separated, the difference between the models is increased. In this wind speed, four turbulence models gave a good prediction: the Spalart–Allmaras, the $k-\epsilon$ RNG, the standard $k-\epsilon$ and the transitional $k-kl-\omega$ models.

4.5.2 Tangential force

Looking now at the tangential forces that are the most important forces of the wind turbine. The tangential forces are the most difficult to predict them. From the Figure 48, we can see that the variation of the tangential force increases along the blade with a non-linear relationship.

At low wind speed, the curve shape of all models was in good agreement with the experimental, with the exception of the standard $k-\epsilon$ model, which know an under-prediction in the medium of the blade. At this low wind speed, good quantitative results were found for all turbulence models. However, a slight underprediction was observed for the Spalart–Allmaras and for the *RSM* models. In addition, an overestimation for different turbulence models (such as Realizable $k-\epsilon$, $k-kl-\omega$, γ_{Re_0} models) was found at the tip of the blade.

● *Experimental*
 + *Spalart Allmaras*
 ▷ *k - ε Standard*
 × *k - ε Realizable*
◇ *k - ε RNG*
 * *k - ω SST*
 ★ *k - kl - ω*
 □ *γ - Re_θ*
 ○ *RSM*

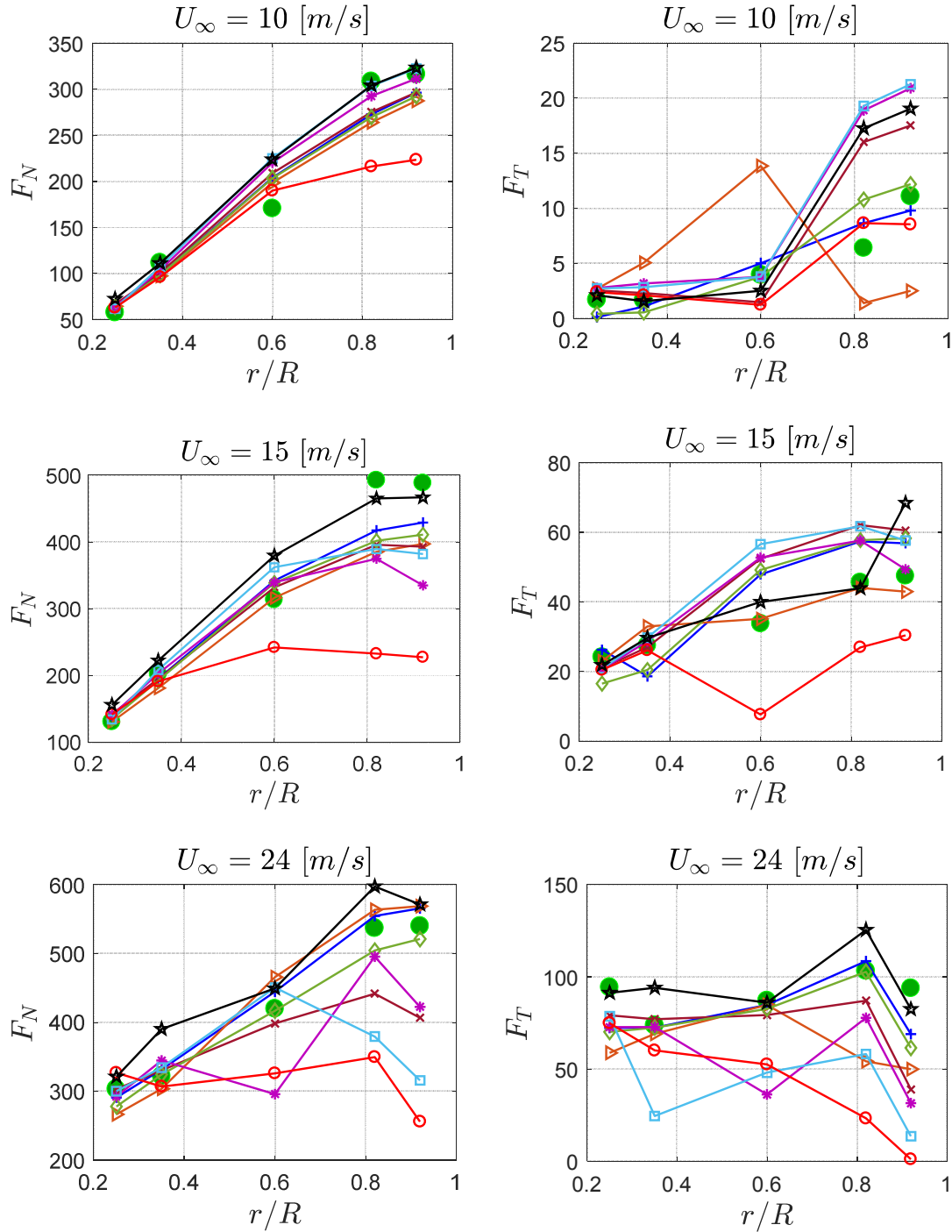


Figure 48: Normal and tangential forces distribution along the blade for different free stream velocities.

4.6 Rotor performances

In order to evaluate the prediction of the different turbulence models on the aerodynamic performance of the rotor, the thrust, torque and mechanical power are calculated and compared with the experimental data. The thrust is calculated by integration of the normal forces along the blade, the torques are calculated by integration of tangential force along the blade. The multiplication of the torque by the rotational speed gives the power. The performances are integrated using a trapezoid method. The integration was based on a simple linear variation between the sections assuming zero value at the root and at the tip of the blade.

The power coefficient, which represents the normalized power by $(0.5\rho\pi R^2 U_\infty^3)$, as a function of the tip speed ratio is presented in Figure 49. To see the accuracy of the studied models, Table 8 shows the relative error of the power (or torque) and the thrust calculated from the experimental data as a function of the corresponding time for a one CPU. It has been shown that the most accurate turbulence model is the $k-kl-\omega$ model which has given reliable results for all cases, where the maximum error does not exceed the 5% in all simulated cases. For low and medium wind speeds, series of models gave reasonable results (such as $k-\epsilon$ RNG, $\gamma-Re_\theta$ and $k-\omega$ SST) where the maximum error varied between 4-20%. For high wind speed, it has been shown that the Spalart-Allmaras model which is specifically designated for high velocities gives reliable results.

The investigation of the computational time presented in the Figures 50-51 reveals that the tested turbulence models based on the Boussinesq assumption (Eddy Viscosity Modes, EVM) consume almost the same computational time, except the $k-kl-\omega$ transitional turbulence model which need three times (compared by other EVM models). However, this computational time is considered reasonable if we see the the accuracy of this model.

It has also been found that the RSM-PSL tested model gives the poor results and it consumed an important time represented 15 times (compared by EVM models) in all cases. This may be due to the numerical discretization of momentum equation which is discretized using first-order upwind scheme due to the convergence problem, or may be the problem due to the nature of formulation of the RSM with wall corrections.

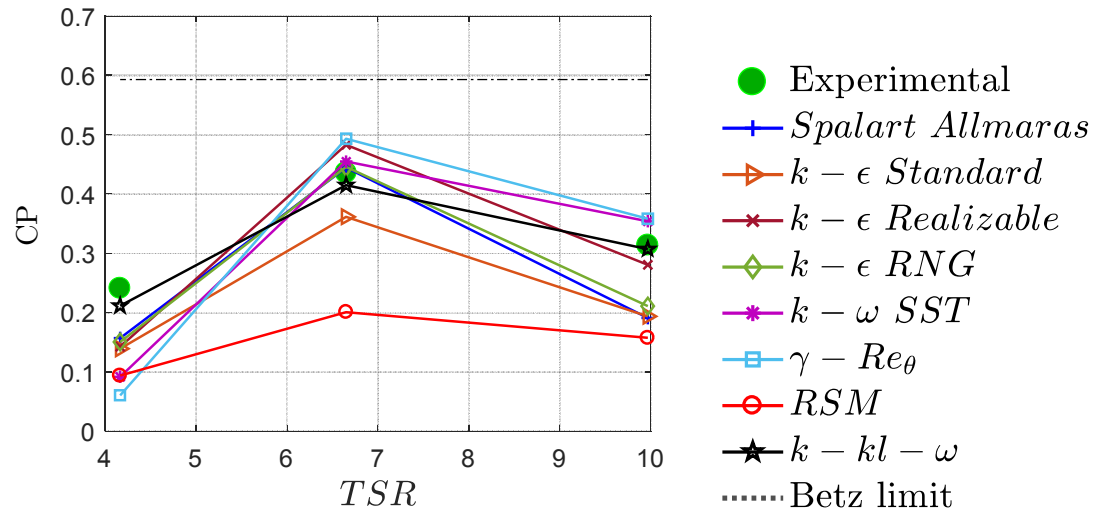


Figure 49: Comparison between CFD, experimental and theoretical results of the distribution of power coefficient as a function of tip speed ratio.

Table 8: Thrust and power relative errors vs computational time per one CPU.

Turbulence model	Computational Time (hour) per 1CPU			Relative Error (%) Thrust			Relative Error (%) Power		
	$U_\infty=10$ (m/s)	$U_\infty=15$ (m/s)	$U_\infty=24$ (m/s)	$U_\infty=10$ (m/s)	$U_\infty=15$ (m/s)	$U_\infty=24$ (m/s)	$U_\infty=10$ (m/s)	$U_\infty=15$ (m/s)	$U_\infty=24$ (m/s)
Spalart-Allmaras	38.48	36.24	34.32	12.0816	14.8609	8.6530	39.1461	2.0713	16.2124
Standard $k-\epsilon$	34.68	29.32	26.20	14.4581	21.1895	8.5305	38.1861	16.9697	36.3669
$k-\epsilon$ RNG	27.08	23.76	36.48	10.7153	17.8885	19.9885	10.5090	10.8601	27.8550
$k-\epsilon$ Realizable	25.17	22.21	29.96	12.7332	16.8295	14.4586	32.7600	2.2257	19.9583
$k-\omega$ SST	20.48	18.20	31.72	6.1126	19.1624	23.9360	12.8833	4.3389	45.7984
$k-kl-\omega$	172.08	131.28	120.56	2.7333	5.1414	2.4324	2.1045	4.8173	4.1586
γ_{Re_0}	22.00	27.64	20.00	3.3959	14.8865	20.4991	14.2040	13.1897	56.6020
<i>RSM – LPS</i>	755.48	525.8	431.8	23.5569	40.7006	33.0840	49.7778	53.8683	62.9100

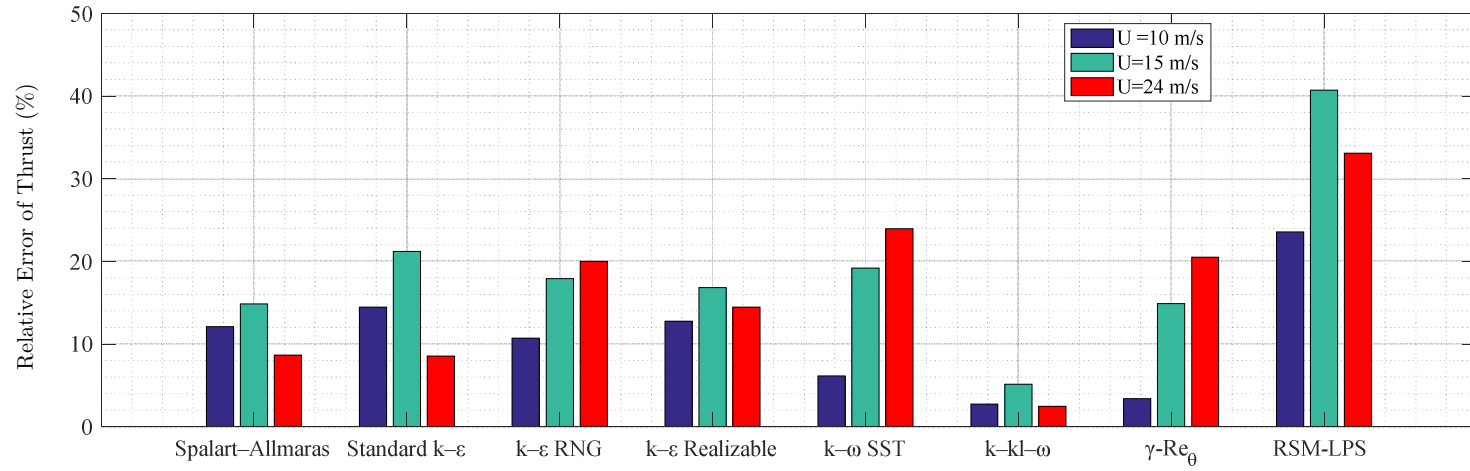


Figure 50: The relative error based on the thrust for different turbulence models.

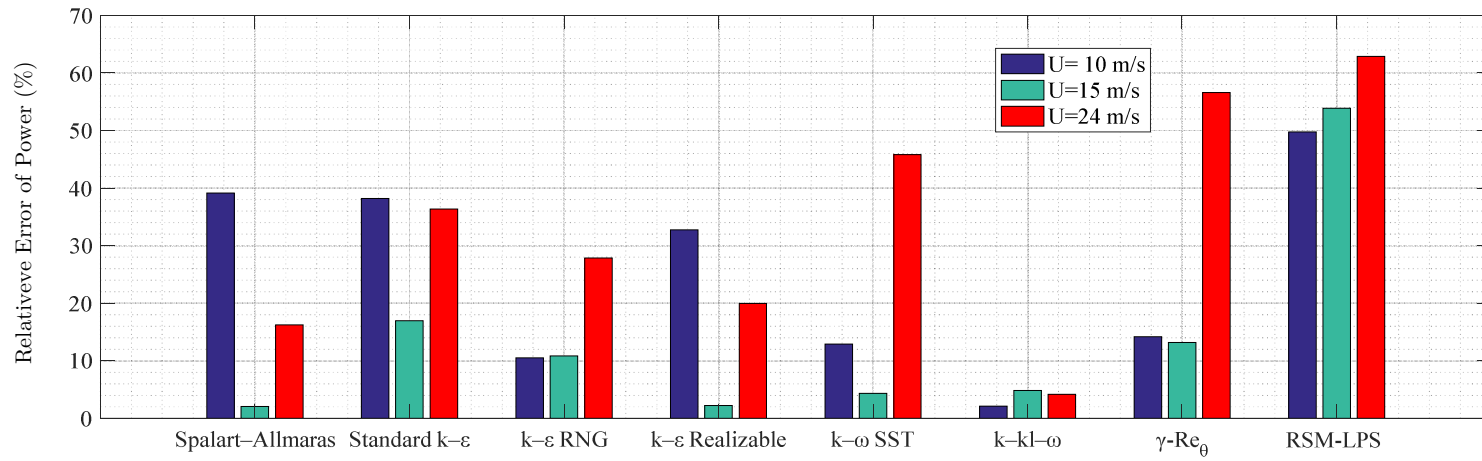


Figure 51: The relative error based on the power for different turbulence models.

4.7 Wake behavior

The components of the velocities represented in this section respect the MEXICO experimental components, the axial velocity (U) reported along (x) axis direction pointing in the flow direction, the radial velocity (V) along the (y) axis perpendicular to the flow direction and tangential velocity (W) along the (z) axis pointing vertically up. The axial velocities were extracted from inboard ($x=-0.5$ m) and outboard ($x=-1.5$ m) traverses positions at the 9 o'clock position plane, and the radial velocities were extracted from upstream ($y=-0.3$ m) and downstream ($y=+0.3$ m) traverses of the rotor, see Figure 52. The objective of this section is to evaluate the accuracy of studied turbulence models on the predicting the velocities in the near wake.

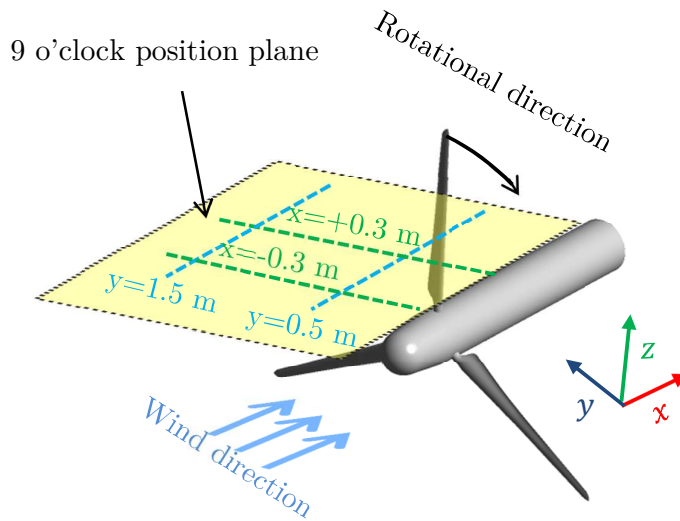


Figure 52: An overview of the line positions in which the velocities were measured in the new MEXICO measurements; (this figure does not respect the actual dimensions).

4.7.1 Axial velocity profile

Figures 53-54 represent the variations of three velocity components U , V and W in the inboard and outboard traverses. Looking firstly at the axial velocity profiles in the outboard of the blade ($y=1.5$ m). The PIV results revealed that the axial velocity profile (U) at each case starts with a constant value (free stream wind speed), and then it decreases rapidly on the level of the rotor due to the rotating of blades until it reaches a fixed value downstream of the rotor, where the velocity profile is stabilized.

The prediction of this velocity induction is very important factor especially for studying the interaction between turbines installed in wind farms. Because the wind speed in the experimental was incoming of the axial direction, the radial (v) and tangential (w)

velocity profiles start with zero value in the upstream of the rotor. Then, as a result of the variation in the fluid velocity due to the blades rotation, the radial and tangential velocities begin to gradually appear for taking a maximum variation at the level of the rotor. This variation disappeared progressively until it re-stabilized at zero value behind the rotor in the far wake.

The axial velocity profiles in the inboard ($y=0.5$ m) of the blade only at the wind speed of 15 m/s was presented in Figure 53; other wind speeds are not available in the new MEXICO experiments. In this region (inboard section), the flow is more complicated due to the developments of the root vorticities due to the great nacelle geometry of the MEXICO rotor.

The comparison between selected turbulence models reveals that all the models give good prediction and the same results for three velocities components in upstream before the interaction of the rotor. After the interaction, over-estimations with varying degrees were observed for all turbulence models, with the exception of the $k-k_l-\omega$ model which gives good predictions. However, the comparison shows reasonable agreements for different models (such, Spalart-Allmaras, $k-\epsilon$ RNG, $k-\epsilon$ Realizable, $k-\omega$ SST, $\gamma-Re_\theta$) especially for the axial velocity (U).

The oscillations appear in PIV results are due to the vorticities developments in the tip and in the root of the rotor, this phenomenon is complicated and it is difficult to predict it numerically using RANS/URANS approaches, as reported in several previous studies [231].

4.7.2 Radial velocity profile

The comparison of axial (U), radial (V) and tangential (W) velocities at the upstream ($x=-0.3$ m) and at the downstream ($x=+0.3$ m) radial traverses for three studied cases is presented in Figures 55-59.

Looking firstly at the upstream profiles. In the far forward of the rotor, the flow starts uniform in the axial direction without any radial or tangential components, while when it reaches the cone-shaped hub, due to the conservation of mass, the flow is forced to change its direction, which leads to an increase of radial velocity and a decrease in axial velocity.

The comparison shows that for the profiles in downstream ($x=+0.3$ m) at low wind speed, good agreements with PIV measurements for all models were observed. However,

a slight overestimation in the tip part at the NACA zone of the blade was observed. For the upstream ($x=-0.3$ m) radial traverses, overestimations at different degrees were observed for all turbulence models, except the transition $k-k_l-\omega$ turbulence model which well predicted the velocities.

With the increase of the wind speed, the difference increases between the models. However, series of models (such as $k-k_l-\omega$, Spalart-Allmaras, $k-\epsilon$ RNG, $k-\epsilon$ Realizable, $k-\omega$ SST, γ_{Re_0} models) are in better prediction than other models, where the maximum error does not exceed the 15% in all cases.

Figure 58 shows the mean axial downstream velocity contours behind the rotor for both high and low Reynolds models, for a wind speed of 10 m/s. The results show that the velocity intensity between the two formulations was almost the same in this case, where flow was mostly attached. However, in the case of high wind speed ($U_\infty = 24$ m/s), (Figure 58), we see that the mean velocity intensity for the low Reynolds models was higher than for the high Reynolds models, and that explains the overprediction of downstream velocity which was noticed in Fig. 54. It was therefore concluded that modeling along the near wall influenced the distribution of velocity behind the rotor, and correction of the wall can reduce the overprediction of velocity.

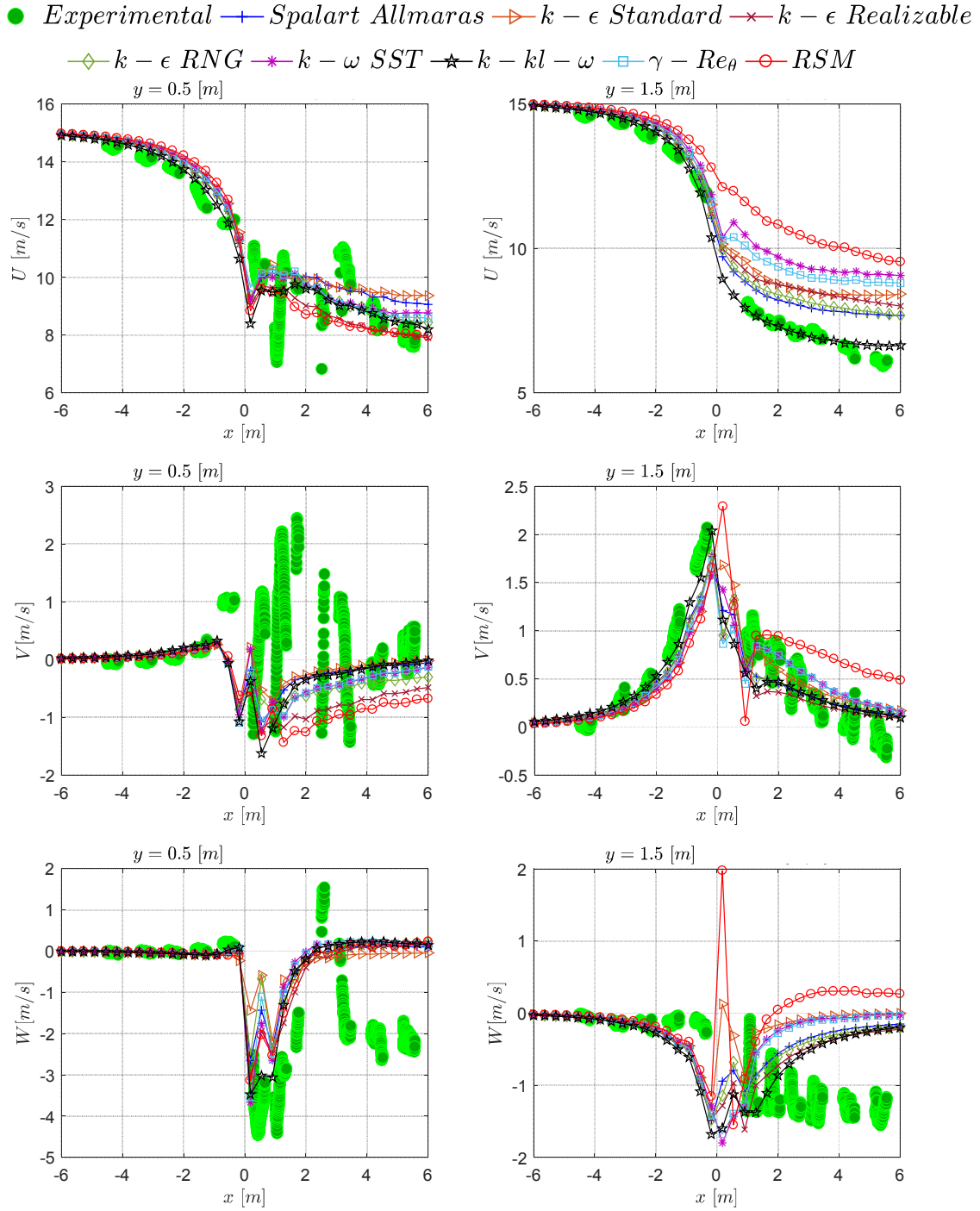


Figure 53: Comparison of axial (U) radial (V) and tangential (W) velocities in the inboard ($y = 0.5 m$) and outboard ($y = 1.5$) traverses for $U_\infty=15 m/s$.

● *Experimental* + *Spalart Allmaras* ▷ *k - ε Standard* × *k - ε Realizable*
◇ *k - ε RNG* * *k - ω SST* ★ *k - kl - ω* □ *γ - Re_θ* ○ *RSM*

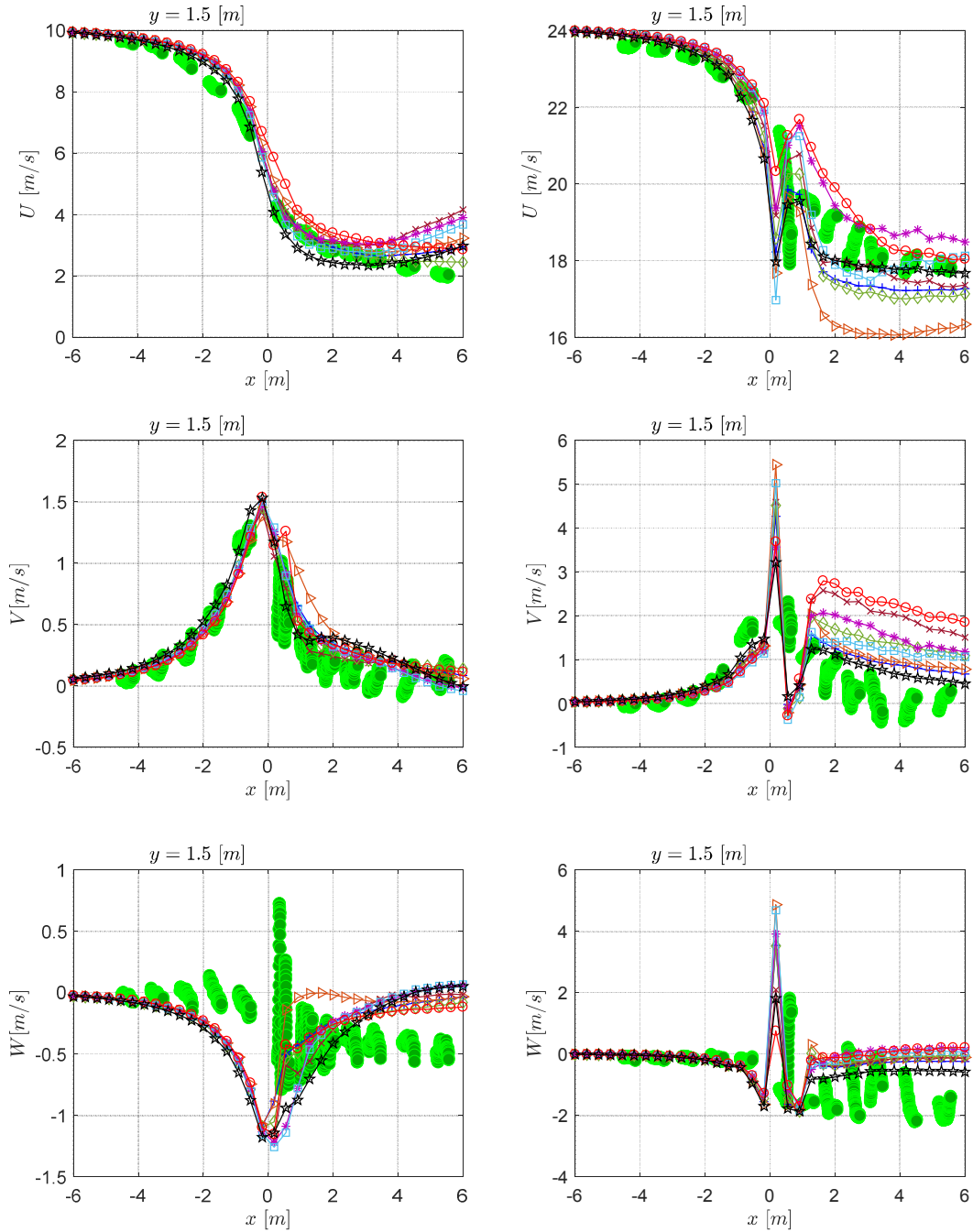


Figure 54: Comparison of axial (U) radial (V) and tangential (W) velocities at the outboard ($y = 1.5$ m) traverses for $U_\infty = 10$ m/s and $U_\infty = 24$ m/s respectively.

● *Experimental* —+— *Spalart Allmaras* —▷— *k - ε Standard* —×— *k - ε Realizable*
 —◇— *k - ε RNG* —*— *k - ω SST* —★— *k - kl - ω* —□— *γ - Re_θ* —○— *RSM*

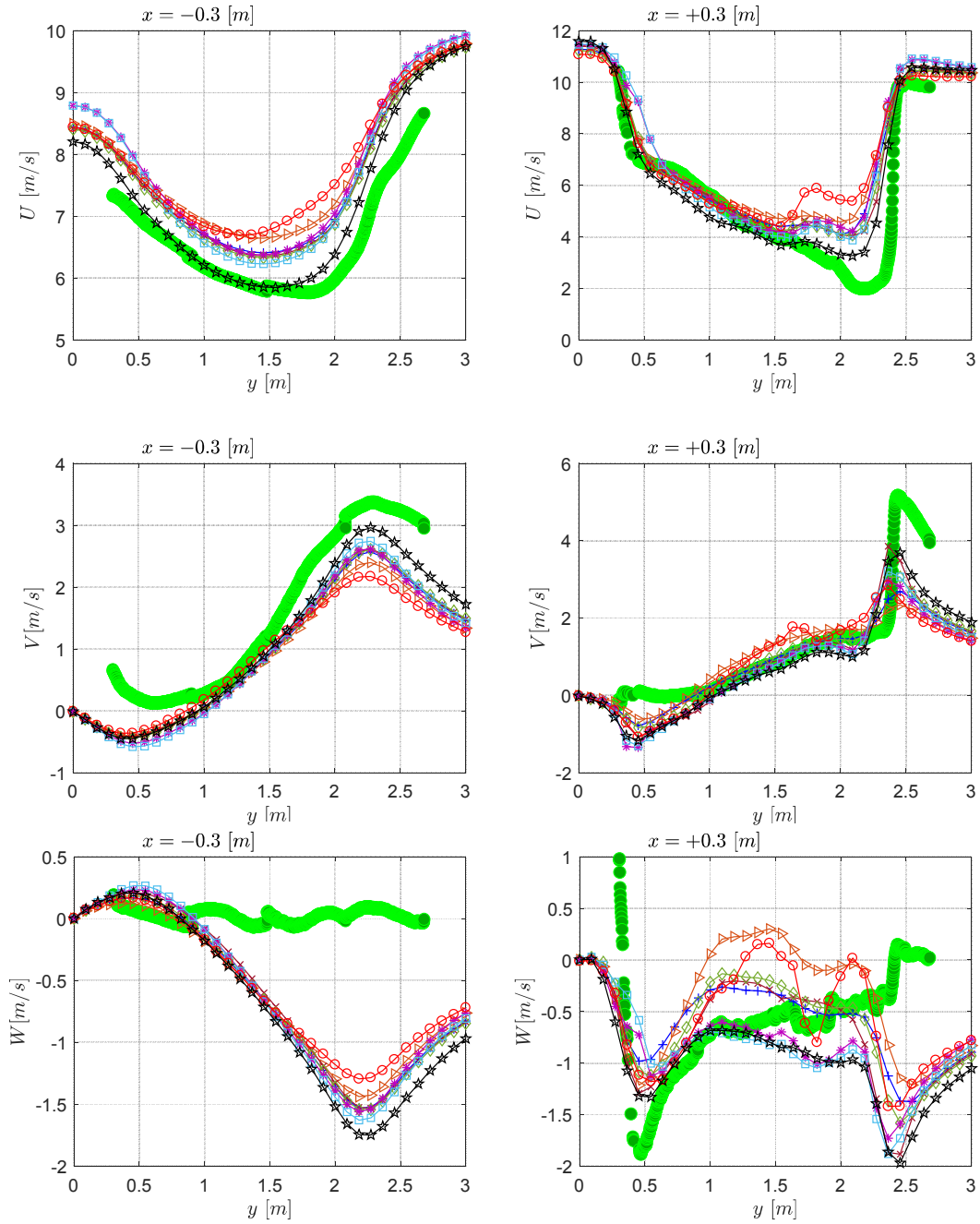


Figure 55: Comparison of axial (U) radial (V) and tangential (W) velocities at the upstream ($x = -0.3 \text{ m}$) and downstream ($x = +0.3 \text{ m}$) traverses for $U_\infty = 10 \text{ m/s}$.

● *Experimental* —+— *Spalart Allmaras* —▷— *k - ε Standard* —×— *k - ε Realizable*
 —◇— *k - ε RNG* —*— *k - ω SST* —★— *k - kl - ω* —□— *γ - Re_θ* —○— *RSM*

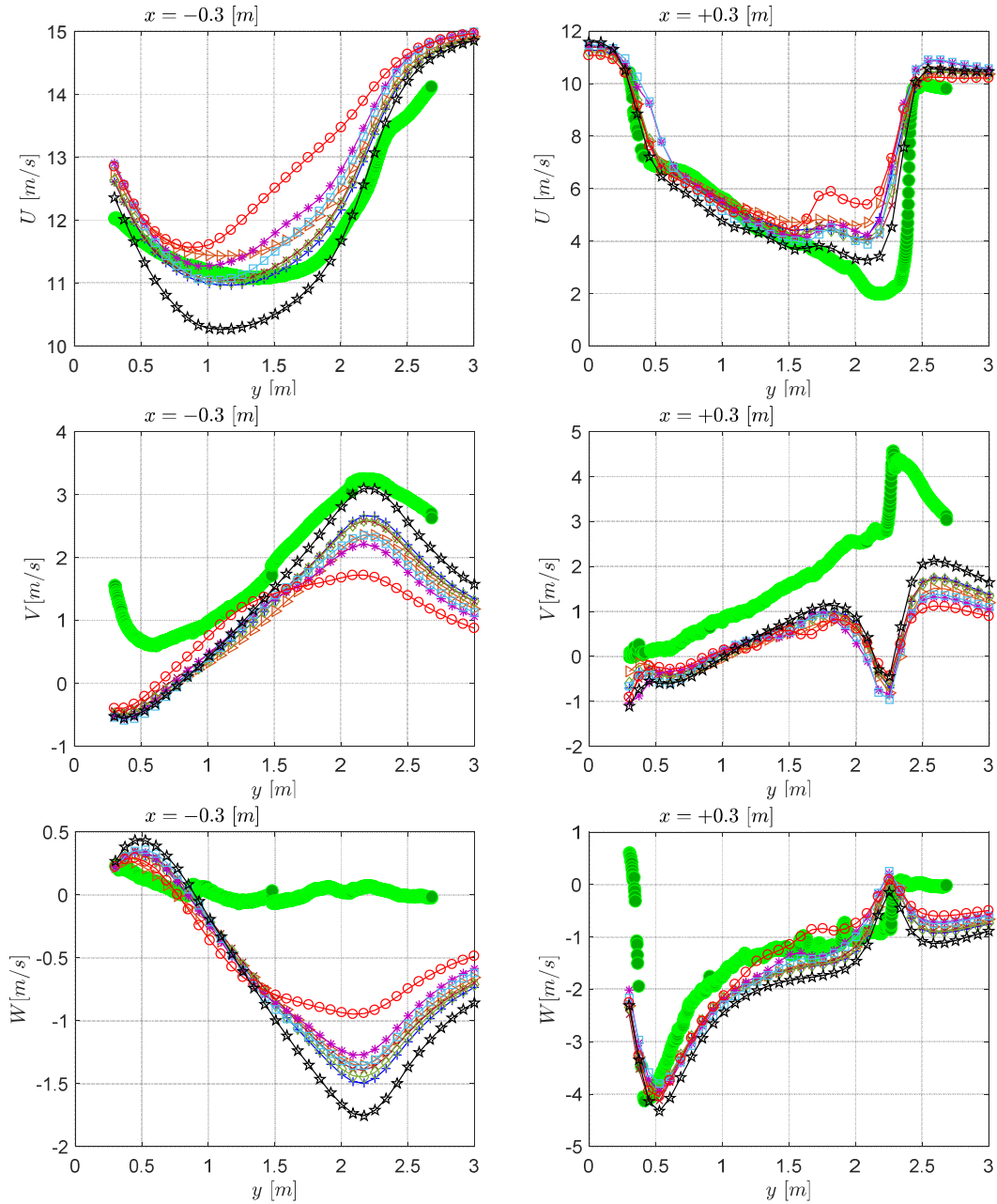


Figure 56: Comparison of axial (U) radial (V) and tangential (W) velocities at the upstream ($x = -0.3$ m) and downstream ($x = +0.3$ m) traverses for $U_\infty=15$ m/s.

● *Experimental* —+— *Spalart Allmaras* —▷— *k - ε Standard* —×— *k - ε Realizable*
 —◇— *k - ε RNG* —*— *k - ω SST* —★— *k - kl - ω* —□— *γ - Re_θ* —○— *RSM*

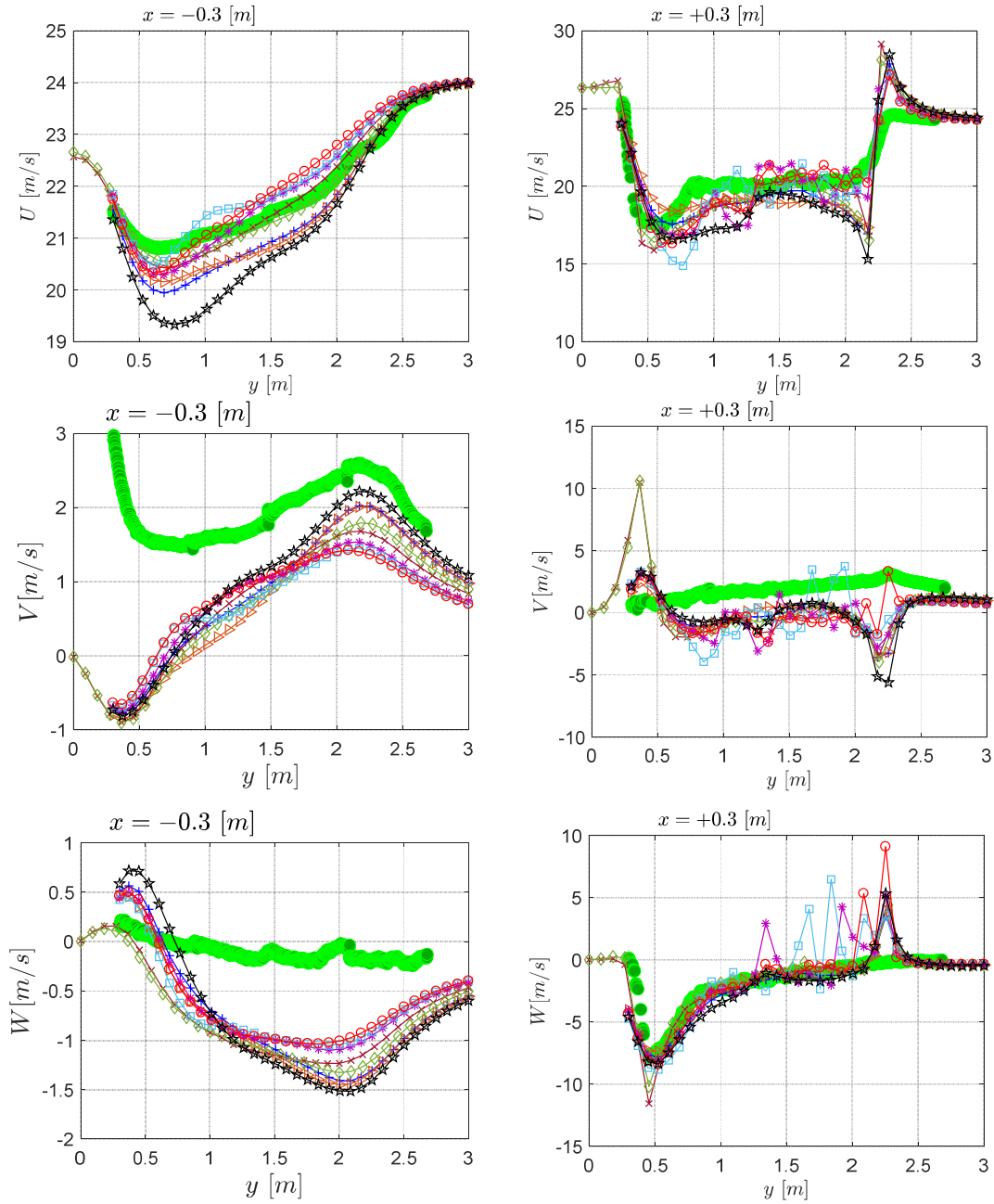


Figure 57: Comparison of axial (U) radial (V) and tangential (W) velocities at the upstream ($x = -0.3$ m) and downstream ($x = +0.3$ m) traverses for $U_\infty=24$ m/s.

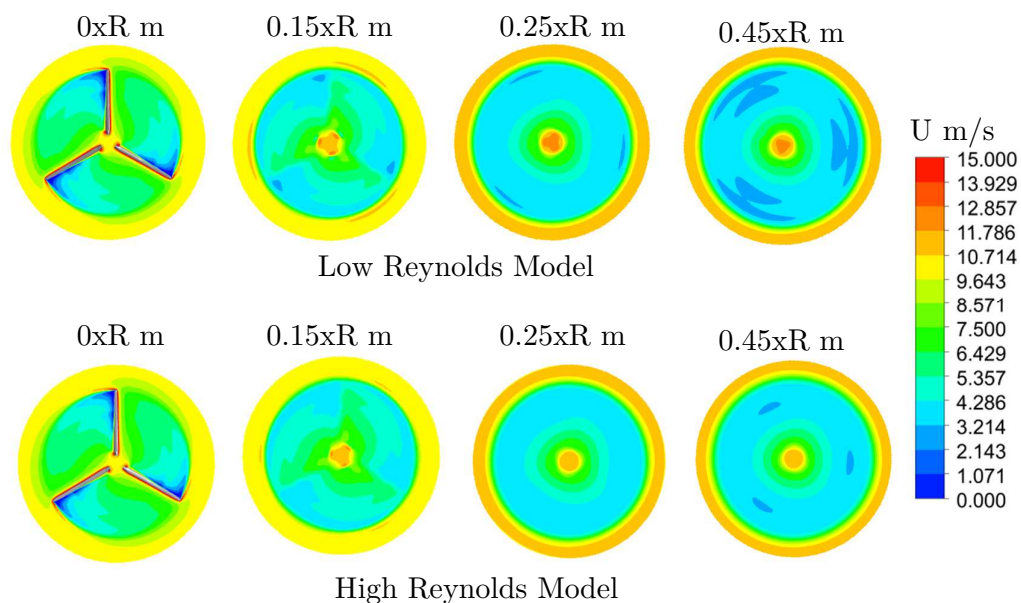


Figure 58: Velocity contours behind the blade, comparison of low and high Reynolds models for low wind speed ($U_\infty = 10$ m/s).

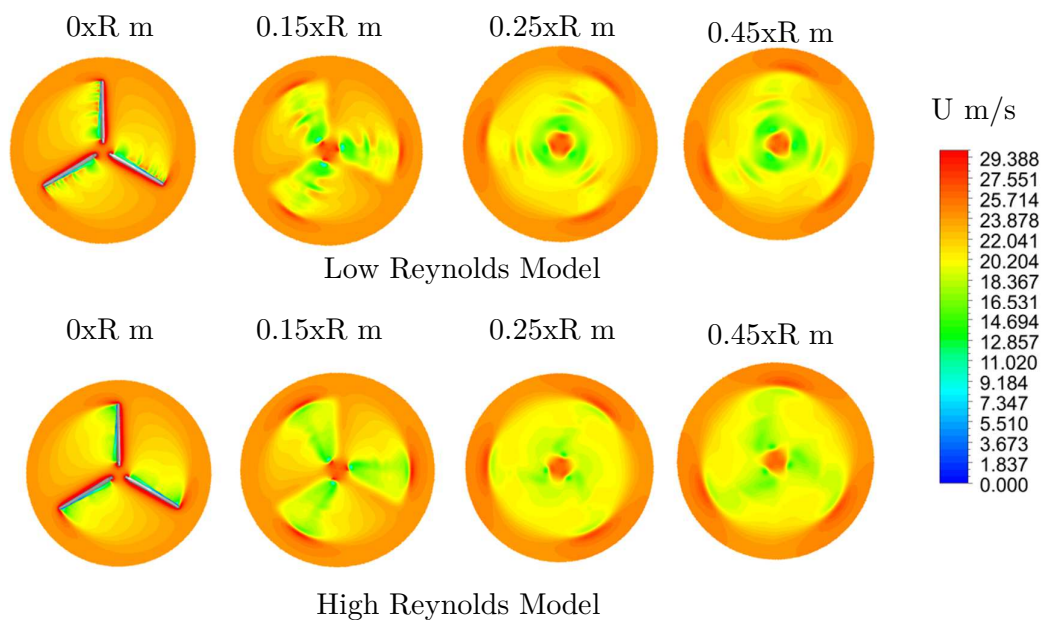


Figure 59: Velocity contours behind the blade, comparison of low and high Reynolds models for high wind speed ($U_\infty = 24$ m/s).

Chapter 5

Results and discussion: Impact of sand particles on the HAWTs performance

In this chapter, the results of the Eulerian-Lagrangian model will be presented. A parametric study includes different parameters (such as sand volume fraction, sand concentration and sand particles diameter) will be analyzed. The impact of sand on the HAWTs performance will be investigated numerically.

5.1 Simplifying assumptions

In this study, the following hypotheses are proposed to simplify the calculation:

- The particles are homogeneous and have a constant diameter;
- The velocity of the fluid and the sand are constant (average velocity);
- The particles velocity is equal to the velocity of the air;
- The concentration of particles in the continuous phase is constant (average concentration);
- Heat transfer and thermal effect are neglected;

- The collision between the particles and the wall of the blade is considered as an elastic collision;
- The collision between the particles themselves is neglected.

5.2 Initial and boundary conditions

In this section, we will present the initial and boundary conditions used in this work. Firstly, the estimation of the concentration of particles in the air will be presented. Then, the characteristics chosen for the flow with particles will be described. Finally, the essential boundary conditions at the inlet and on the wall will be discussed.

5.2.1 Particles volume fraction

The particles volume fraction α_s can be calculated as a function of the particles flow rate, particles velocity and particles density as [174, 232]:

$$\alpha_{s_{inlet}} = \frac{\dot{m}_p}{\rho_p u_p S_{inlet}} \quad (193)$$

where \dot{m}_p denotes the sand mass flux (kg/s), u_p is the mean particle velocity and S_{inlet} is the inlet surface of the computational domain.

In this study, five particles volume fraction values varied from $\alpha_{s_{inlet}} = [10^{-4} - 10^{-2}]$ have been simulated. These values were selected according to references [170, 232], which they showed that the sand has a few volume fraction around of these values in desert areas.

5.2.2 Characteristics of the sand-air flow

In this study, because the purpose was to study the local region of Adrar, the characteristics of sand in this region have been used in the simulations. particles density in Adrar region is $\rho_p = 2240 \text{ kg/m}^3$ according to Benhammou et al. [233].

Since the particles diameter in the studied region is unknown, therefore, five different sand particles diameters have been considered representing the fine and medium sand ($d_p = 100, 200, 300, 400 \text{ and } 500 \mu\text{m}$). These values were selected according to the International Scale for the identification and classification of soils, ISO [234].

The annual average velocity at Adrar region at the height of 10 meters is about 6.30 (m/s) [235]. However, wind turbines in the Kaberten farm are installed with a tower height of 55 metres.

The velocity profile as a function of the height can be defined using a power law as [236, 237]:

$$\frac{u(h)}{u_0} = \left(\frac{h}{h_0}\right)^\alpha \quad (194)$$

where $u(h)$ is the wind speed at the required height h , and u_0 is the wind speed measured at the reference height h_0 .

and α is the surface roughness coefficient.

In the Adrar zone, surface roughness coefficient (α) is 0.29 according to the reference [236, 237]. Therefore, using the relation (194), the wind speed at the rotor level can be estimated as $U_\infty = 10$ m/s.

5.2.3 Particles injection

There are different ways in the solver to inject the particles into the computational domain:

- **Single injection:** a particle stream is injected from a single point.
- **Group injection:** particle streams are injected along a line, see Figure 60(a).
- **Cone injection:** particle streams are injected in a 3D conical pattern, see Figure 60(b).
- **Surface injection:** particle streams are injected from a surface (one from each face). This type of injection has been used in this study, where the injection surface is the inlet of the computational domain, see Figure 61.

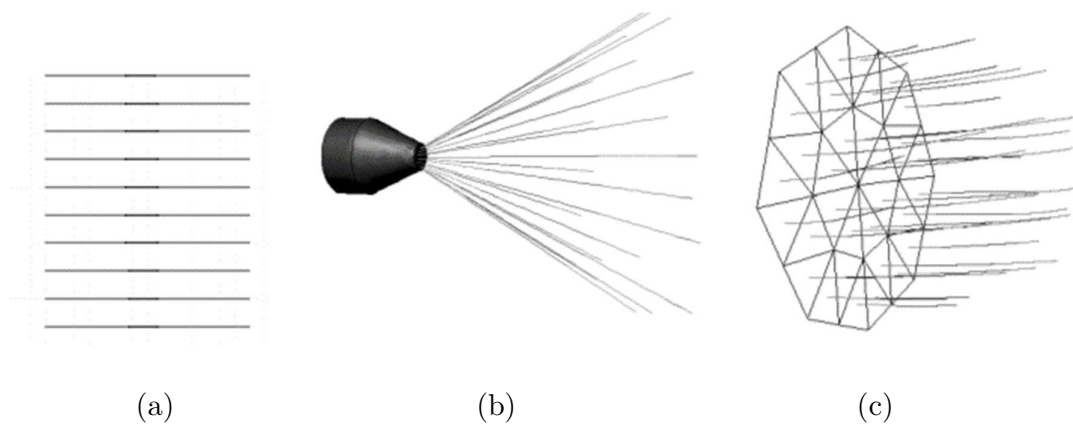


Figure 60: Types of particles injections; (a) group injection, (b) 3D cone injection, (c) injection from a surface.

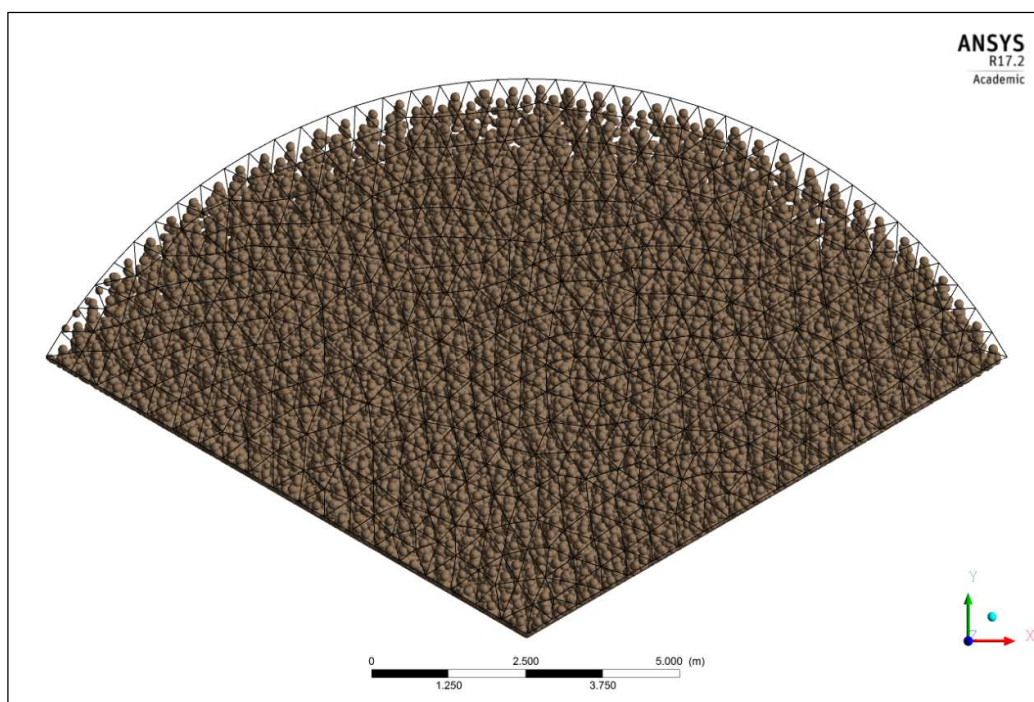


Figure 61: Particles injection into the inlet surface of the computational domain.

5.2.4 Wall-Particle Reflection

In the wall boundary, the particle rebounds off with a change in its momentum as defined by the coefficient of restitution presented in Figure 62. In this study, this rebound is assumed as an elastic collision, that means that the particle retains all of its normal or tangential momentum after the rebound.

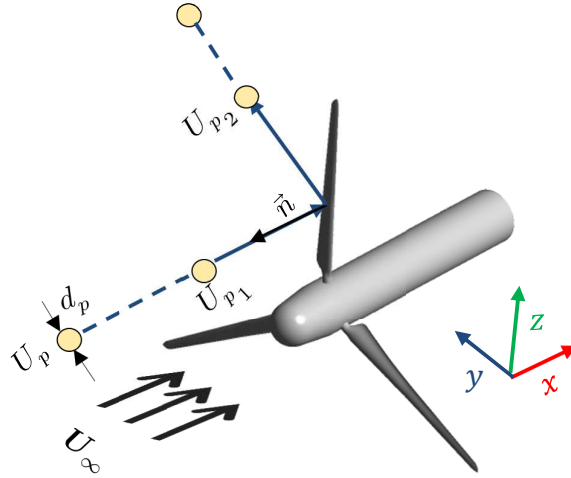


Figure 62: Sketch of the reflection of sand particles on the blade surface.

The normal coefficient of restitution defines the amount of momentum in the direction normal to the wall that is retained by the particle after the collision with the boundary [238]. The normal coefficient of restitution e_n is defined as:

$$e_n = \frac{u_{p2,n}}{u_{p1,n}} \quad (195)$$

where $u_{p1,n}$ is the particle velocity normal to the wall before collision, and $u_{p2,n}$ is the particle velocity normal to the wall after collision.

Similarly, the tangential coefficient of restitution e_t defines the amount of momentum in the direction tangential to the wall that is retained by the particle.

In this study, to achieve the elastic collision assumption between particles and the blade surface, the normal and tangential coefficient of restitution should be equal to 1.

5.3 Numerical setup

In this study, for the fluid, the k - kl - ω turbulence model was used to close the RANS equations for all simulations. The discrete phase motion equation for each particle has been solved numerically based on the Runge-Kutta method using a low time step of order $\Delta t = 10^{-6}$ to improve the accuracy of results. The maximum number of steps to compute a single particle trajectory is $N_{\max} = 10^7$ steps. The limit on the number of integration time steps eliminates the possibility of a particle being caught in a recirculating region of the continuous phase flow field and being tracked infinitely.

The calculation begun by solving the fluid flow field without particles. Using this flow field, particles trajectories are calculated. The momentum source terms for each cell throughout the flow field then are determined. The fluid flow field is solved again, incorporating these source terms. The new fluid flow field is used to establish new particles trajectories, which constitute the effect of the fluid phase on the particles. Calculating new source terms and incorporating them into the fluid flow field equations constitutes the effect of the particles on the fluid phase, thereby completing the cycle of mutual interaction or “two-way” coupling. After several iterations, the flow field equations are satisfied to within a predetermined value and the solution which accounts for the mutual interaction of the particles and fluid is obtained. A 3D view of particles tracking from $time = 0.5$ to 2 (s) is presented in Figure 64.

In the beginning of the calculation, we tried to establish the effect of the existing forces in the particles motion equation. It has been shown that three forces cannot be neglected: the drag, gravity and MRF force. This latter which applied for modeling the particles that pass through the rotating part of the computational domain, while the particles away from the blade do not rotate and its trajectories are continuous (Figure 63). It has been also found that lift forces did not represent any effect on the solutions, so they are neglected in this study.

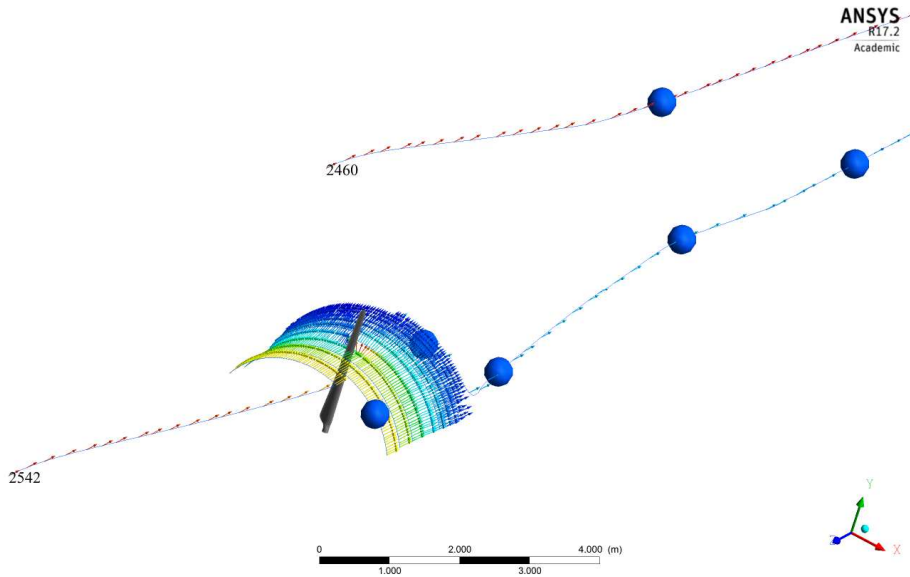


Figure 63: Trajectory of particles close to the blade and those far from the blade.

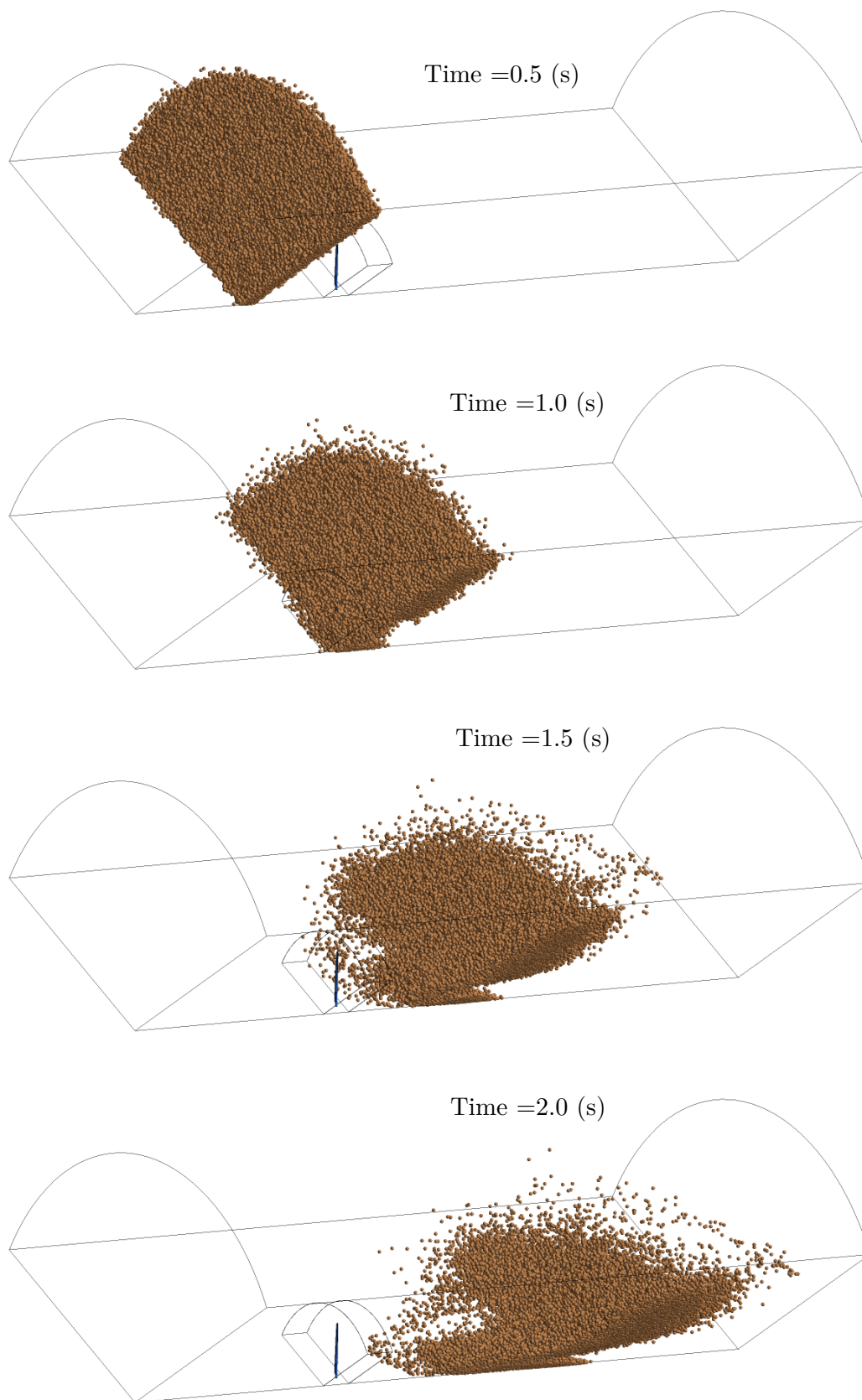


Figure 64: Lagrangian tracking of sand particles around the blade.

In this study, an intended external routine has been implemented in the solver for identifying the impacts of the sand particles by computing the forces on the blade surface. In this routine, the torque is calculated based on the integration of pressure and shear stress surrounding at five-span sections of the blade: 25%, 35%, 60%, 82% and 92% respectively. The integration was based on a simple linear variation between the sections assuming zero value at the root and tip of the blade.

The analysis of the results was based on the mean volume fraction and the mean mass concentration, which were calculated respectively by:

$$\bar{\alpha}_s = \frac{\int_{i=1}^{N_{cell}} (\alpha_s \cdot v)_i}{V_{tot}} \quad (196)$$

$$\bar{c} = \frac{\int_{i=1}^{N_{cell}} (c \cdot v)_i}{V_{tot}} \quad (197)$$

where $\bar{\alpha}_s$ and \bar{c} are the mean particles volume fraction and the mean particles concentration respectively. v , c and α_s are cell volume, particles concentration and particles volume fraction of i^{th} cell respectively, and V_{tot} is the total cell volume of the computational domain.

The mean volume fraction and mean concentrations calculated for five studied cases are respectively: $\bar{\alpha}_s = [0.0001 - 0.0004 - 0.0009 - 0.0013 - 0.0015]$ and $\bar{c} = [0.3152 - 0.9455 - 1.8910 - 2.8365 - 3.1517]$ (kg/m^3).

The general effects of sand particles on the performances of the rotor will be presented in the following sections.

5.4 Impact of particles concentration

The curves of the calculated rotor torque as a function of five mean volume fractions varied from 10^{-4} to 1.5×10^{-3} , and their corresponding sand mass concentration ranging from 0.31 to 3.15 [kg/m^3], for five different particles diameter $d_p = 0.1, 0.2, 0.3, 0.4$ and 0.5 [mm], are shown in Figure 65.

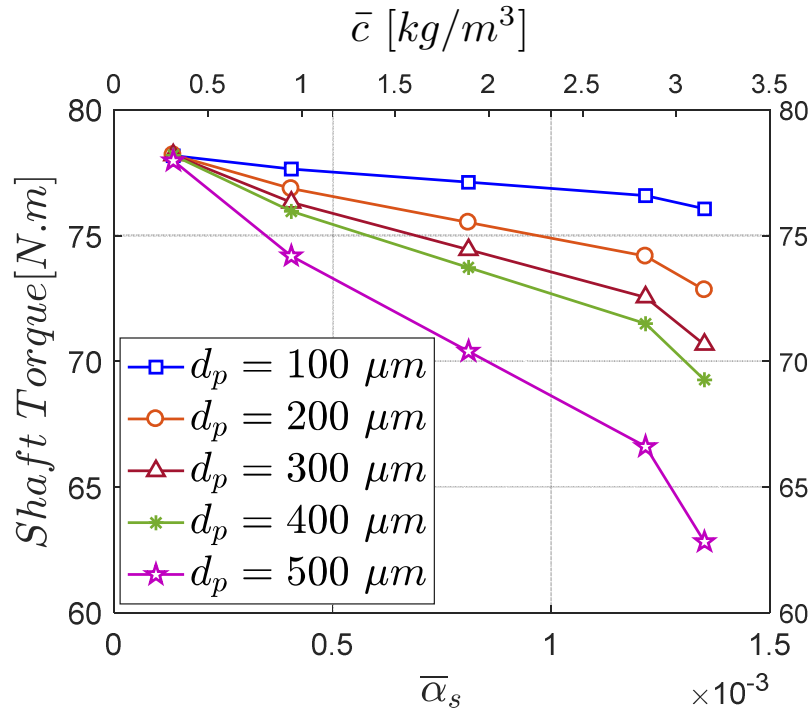


Figure 65: Variation of the rotor torque as a function of particles concentration for different particles diameter.

From the figure 65, we can see the significant influence of sand particles on the rotor torque. For the five-studied size of the sand particle diameter, the aerodynamic torque is degraded with the increase of the particle volume fraction and particle concentration. To properly analyze the influence of the sand particles concentration we take a single case (as an example, the case of $d_p = 500 \mu m$), while the influence of particles diameter will be discussed in the section that follows. It appears from the curve of $d_p = 500 \mu m$ that the decrease in torque with concentration follows a semi-linear relationship. The slope of this curve increases with the increase of particles concentration. For the smaller values of the volume fraction and concentration ($\bar{\alpha}_s = 10^{-4}$, $\bar{c} = 0.3152 \text{ kg/m}^3$), the rotor lost a slight value represents 0.28 Nm of its total torque.

With the increase of the sand concentration, the loss of rotor performance becomes more important, the rotor lost about 4, 7 and 11 N.m with the concentration of $\bar{\alpha}_s = 4 \times 10^{-4}$, $\bar{\alpha}_s = 9 \times 10^{-4}$ and 1.3×10^{-3} respectively. The great rotor loss was noticed for the large values of the concentrations, for $\bar{\alpha}_s = 1.5 \times 10^{-3}$, $\bar{c} = 3.1517 \text{ kg/m}^3$, the loss, in this case, is 15.4292 N.m, which represented a great mechanical power of 686.75 watts.

5.5 Impact of particles size

To well examine the effect of sand wind on the performance of HAWTs, the variation of the power loss for different particles sizes was presented in Figure 66. It is clear from the figure that the power loss is a function of the particle size and this loss for higher particles diameters and for higher concentrations can reach up to 20%. The loss of the power decreases with the decrease of particles diameter. For the volume fraction of $\bar{\alpha}_s = 1.5 \times 10^{-3}$, the loss of the power was 2.8%, 6.9%, 9.7%, 11.5% and 19.7% for the particle size of 0.1, 0.2, 0.3, 0.4 and 0.5 mm respectively.

For further understand the effect of the sand particles on the performances of the rotor, the distribution of the pressure coefficient at the first spanwise section of the blade ($r/R=0.25$) for a high concentration ($\bar{\alpha}_s = 1.5 \times 10^{-3}, \bar{c} = 0.3152 \text{ kg/m}^3$) is presented in Figure 67; other spanwise sections are quite similar. It can be seen from this figure that the increase of the particles size can affect the pressure distribution by decreasing it, especially at the extrados part, on the leading edge of the blade airfoils. This decrease in the pressure reflects directly the effect of the sand particles on the flow field.

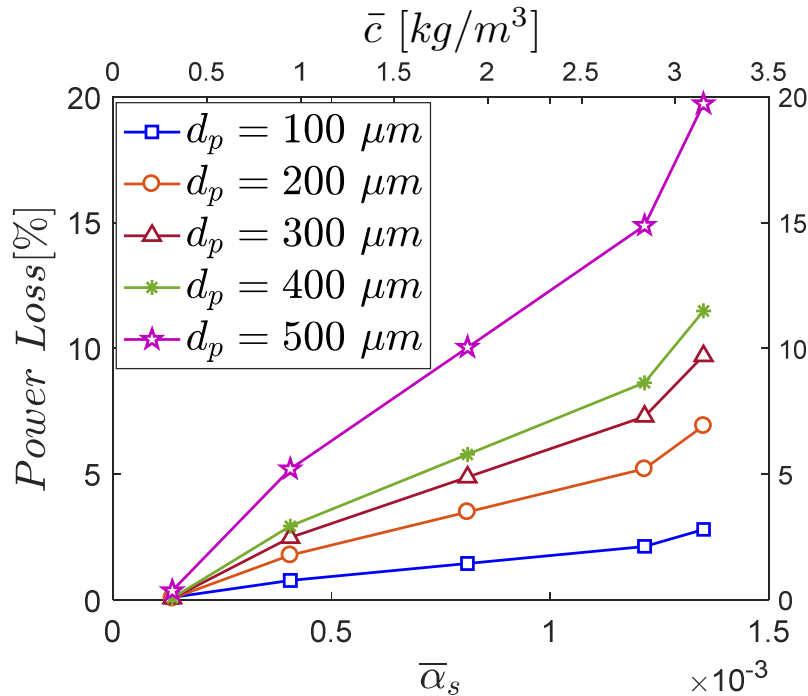


Figure 66: Power loss as a function of particles concentration for different particles diameter.

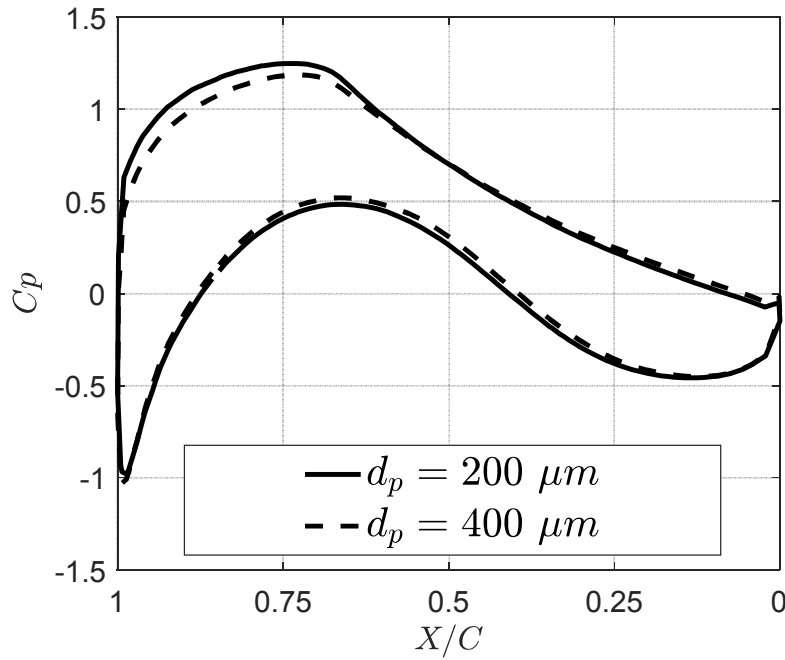


Figure 67: Distribution of the pressure coefficient at $r/R=0.25$ spanwise blade section for different particles diameter, for $\bar{\alpha}_s = 1.5 \times 10^{-3}$.

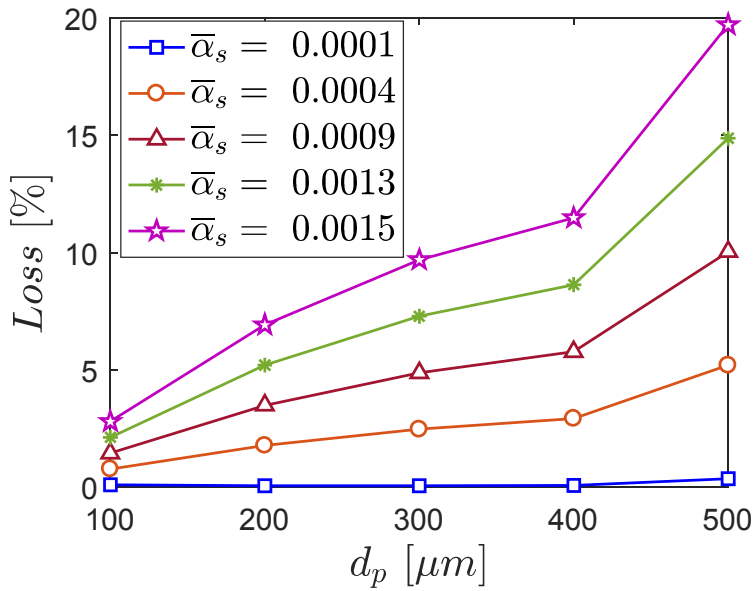


Figure 68: Power/Torque loss as a function of particles diameter for different mean particles volume fractions.

Figure 68 shows the power loss as a function of the particles diameter under different volume fractions. From this figure, it is clear that the curves of the power loss increase

with the increase of particles diameter for all cases. It appears that the evolution of power loss curves is done by a semi-exponential law.

It has been shown that the particles size has a significant impact on the performance of the rotor, especially for the higher volume fractions. For fine particles size of 0.1 mm, the power loss does not exceed the 4% even for the highest concentration. Contrariwise, for the higher particles sizes, the power loss was sensitive even for the smaller volume fractions, with the exception of the first volume fraction of 0.3%, where the loss of the energy is negligible for this low volume fraction for all studied cases.

Conclusions and future works

In this thesis, a 3D CFD code based on the resolution of the stationary averaged incompressible Navier-Stokes equations has been developed to predict the aerodynamic performance and to study the characteristics of the flow around a wind turbine model. Due to the symmetry of the flow, the computational domain was constructed only on one blade, representing one-third of the full rotor geometry. The steady-state MRF approach was used for modeling the rotation of the blade.

The first main goal was to evaluate the capacity of different RANS turbulence models on the predicting of the aerodynamic performance as well as the velocities in the near wake of HAWTs. Ten turbulence models in two near wall formulations; low Reynolds models (Standard $k-\omega$, $k-\omega$ BSL, $k-\omega$ SST, transitional $k-kl-\omega$ and transitional $\gamma-Re_\theta$) and high Reynolds models (Spalart-Allmaras; Standard $k-\epsilon$; $k-\epsilon$ RNG; $k-\epsilon$ Realizable and *RSM-LPS*) have been tested. The New MEXICO measurements have been used to evaluate the selected turbulence models. Three different axial flow conditions have been considered which cover the range of flow varied from fully attached to massively separated. The comparison between numerical and experimental results allowed us to identify the strengths and the weaknesses of the selected turbulence models.

The second main goal was to identify numerically the effect of the sand particles on the aerodynamic performance of wind turbines installed in desert environments. A Lagrangian approach has been used for modeling the sand particles. In this approach, the particles are considered as a discrete phase governed by Newton's second law, where the imposed forces are the gravity and the drag. In the rotating part close to the blade,

an additional force due to the moving frame has been applied to ensure the rotation of the particles. A parametric study takes into account different characteristics of the air-sand flow has been applied for the local conditions of Algeria.

From the work presented in this thesis, the following conclusions can be drawn:

- ❖ It has been shown that the choice of a RANS turbulence model plays a very important role in the numerical prediction of the results.
- ❖ At low wind speeds, a series of models represents fully turbulent models (Spalart–Allmaras; Standard $k-\epsilon$; $k-\epsilon$ RNG; $k-\epsilon$ Realizable, $k-\omega$ SST) and transition models ($k-kl-\omega$, γ_{Re_0}) gives a good predictions and very similar results of the prediction of the rotor performances and the velocities in the near wake. This due to the uncomplicated nature of the flow field over this range of wind speed, where the flow is attached in the whole blade.
- ❖ With the increase of the wind speed, the differences between models appear; the difficulty of predicting the separation phenomenon in most turbulence models becomes very clear. However, a series of models has been well past this difficulty to give reasonable results: high Reynolds models (Spalart–Allmaras, $k-\epsilon$ Realizable) and the $k-kl-\omega$ low Reynolds model.
- ❖ It has also been shown that the inclusion of the transition in the RANS models can improve importantly the results of prediction. And, it has been found that the transitional $k-kl-\omega$ is the better model among all the others, which it gave a good prediction for all cases (attached and separated flow), where the maximum error in all the cases is not exceeded the 5%, that makes it the most appropriate model for this kind of applications (flows around HAWTs).
- ❖ The weakness of the transitional γ_{Re_0} model is may be due to the nature of its transition formulation that is developed using correlations based on the flows over the flat plate. Therefore, more advanced correlations, which must be based on the flow around rotating wind turbines, are required to improve the transition in this model.
- ❖ It has been shown that the standard $k-\omega$ and $k-\omega$ BSL models are not appropriate for studying the HAWTs, since they give an extra over-estimation of the aerodynamic performance and the velocities in the wake, where the error was exceeded the 80%, (see [Appendix B](#)). The main reason of this over-

estimation is that both the standard $k-\omega$ and BSL $k-\omega$ do not account for the transport of the turbulent shear stress. This has led to an over-prediction of their turbulence viscosity.

- ❖ It has also been shown that the Boussinesq hypothesis, which is based on the assumption of the isotropic turbulence, can be considered as a reliable theory for modeling the turbulence of the flows around HAWTs, where several types of EVM models have been given a good prediction.
- ❖ Typically, the models that are based on the an-isotropic assumptions are the most accurate models. However, it has been found that the RSM-PSL model gives the poor results and it consumed the most important time in all cases. This maybe due to the numerical discretization of momentum equation which is discretized using first-order upwind scheme or due to the high Reynolds formulation. Indeed, several types of RSM implemented in the solver have been tested, it has been shown that the RSM models are give convergence problems. consequently, the RSM models are not recommended for simulating the flows around rotating HAWTs.
- ❖ The investigation of the computational time reveals that the most tested EVM turbulence models consume almost the same computational time, with the exception the transitional $k-kl-\omega$ which is required three times compared to others EVM models. However, this computational time is considered as reasonable regarding the accuracy of this model. The RSM is the most expensive model that required an important computational time represents 15 times compared by the other models.
- ❖ Regarding now at the found results concerning the multiphase flow (air-sand) around of HAWTs. Firstly, it has been shown that the sand particles have a significant impact on the rotor performance and it has been confirmed that the sand wind can degrade importantly the output power of the wind turbines.
- ❖ It has been demonstrated that the rotor performance degrades with the increase of particles concentration by a semi-linear way. For considerable concentrations of order 3 kg/m^3 where the particles volume fraction represents 0.15% of the total volume; the power loss can reach up to 20%.

- ❖ It has also been shown that the particles size has a significant influence on the degradation of the performance of the rotor, especially for the higher concentrations and higher volume fractions.
- ❖ For the smaller sand particles size, the power loss was not much affected, even for the highest concentrations. Otherwise, for larger particles, the rotor is more susceptible to degradation even for the smaller concentrations.
- ❖ It has been shown that the increase of the particles size can affect the pressure distribution by decreasing it, especially at the extrados part, on the leading edge of the blade airfoils.

FUTURE WORKS

As a future work related to the effect of sand on the wind turbines, it is recommended to perform an experimental study to confirm the conclusions presented in this study and for further understand the phenomenon of the air-sand around HAWTs.

In fact, the numerical simulation of the multiphase flow (air sand) using E-L approach is complicated and it required important computing resources. For this reason, simpler methodologies are needed, as a future work for example, instead of treating two-phase flow (fluid-particles), we can just simulate the continuous phase (air) and modeling the effects of particles using a modification of the standard wall function. We can achieve this, by adjusting a relationship between the dimensionless sand grain roughness height, k_s^+ , and the variables of the multiphase flow problem (such as, $u_\infty, u_p, \rho_p, d_p, \bar{\alpha}_s, \bar{c}, \Omega$).

Bibliography

- [1] S. GWEC, Global Wind, Global Wind Energy Council (GWEC): Opening up new markets for business, Mongolia, 5 May 2017.
- [2] I.E.A. (IEA), World energy outlook (2017).
- [3] J. Thé, H. Yu, A critical review on the simulations of wind turbine aerodynamics focusing on hybrid RANS-LES methods, *Energy* 138 (2017) 257-289.
- [4] J.G. Shepers, Engineering models in wind energy aerodynamics: Development, implementation and analysis using dedicated aerodynamic measurements, (2012).
- [5] J. Schepers, K. Boorsma, T. Cho, S. Gomez-Iradi, P. Schaffarczyk, A. Jeromin, W. Shen, T. Lutz, K. Meister, B. Stoevesandt, Final report of IEA Task 29, Mexnext (Phase 1): Analysis of Mexico wind tunnel measurements, 2012.
- [6] D.C. Wilcox, Turbulence modeling for CFD, DCW Industries, Inc., California (1993).
- [7] ANSYS Fluent, 17.2 Documentation, 2017.
- [8] F.J. Buendía, A. Viguera-Rodríguez, E. Gómez-Lázaro, J.A. Fuentes, A. Molina-García, Validation of a mechanical model for fault ride-through: Application to a Gamesa G52 commercial wind turbine, *IEEE Transactions on Energy Conversion* 28(3) (2013) 707-715.

BIBLIOGRAPHY

- [9] Ouahiba GUERRI, Compte rendu de la Journée sur l'Énergie Éolienne en Algérie DZ-EOL, Centre de Développement des énergies renouvelables (CDER), Mercredi 25 mars 2015.
- [10] F. Malatesta, CFD Study of a wind turbine Rotor, School of Engineering and Materials Science, Technical report (2012).
- [11] V. Nelson, Wind energy: renewable energy and the environment, CRC press 2013.
- [12] W. Energy, A Vision for Europe in 2030, Advisory Council of the European Wind Energy Technology Platform (2006).
- [13] A.P. Schaffarczyk, Introduction to wind turbine aerodynamics, Springer 2014.
- [14] C.-J. Bai, W.-C. Wang, Review of computational and experimental approaches to analysis of aerodynamic performance in horizontal-axis wind turbines (HAWTs), Renewable and Sustainable Energy Reviews 63 (2016) 506-519.
- [15] R.A. Kishore, S. Priya, Design and experimental verification of a high efficiency small wind energy portable turbine (SWEPT), Journal of Wind Engineering and Industrial Aerodynamics 118 (2013) 12-19.
- [16] M. Ghasemian, Z.N. Ashrafi, A. Sedaghat, A review on computational fluid dynamic simulation techniques for Darrieus vertical axis wind turbines, Energy Conversion and Management 149 (2017) 87-100.
- [17] J.N. Sørensen, General momentum theory for horizontal axis wind turbines, Springer 2016.
- [18] A. Betz, Das Maximum der theoretisch möglichen Ausnützung des Windes durch Windmotoren, Zeitschrift für das gesamte Turbinenwesen 26(307-309) (1920) 8.
- [19] K. Bergey, The lanchester-betz limit, Journal of Energy 3 (1979) 382-384.
- [20] N. Joukowsky, Windmill of the NEJ type, Transactions of the Central Institute for Aero-hydrodynamics of Moscow 1 (1920) 57.
- [21] G.A. Van Kuik, The Lanchester–Betz–Joukowsky limit, Wind Energy 10(3) (2007) 289-291.
- [22] H. Glauert, Airplane propellers, Aerodynamic theory, Springer 1935, pp. 169-360.
- [23] W.Z. Shen, W.J. Zhu, J.N. Sørensen, Actuator line/Navier–Stokes computations for the MEXICO rotor: comparison with detailed measurements, Wind Energy 15(5) (2012) 811-825.
- [24] S. Guntur, N.N. Sørensen, A Detailed Study of the Rotational Augmentation and Dynamic Stall Phenomena for Wind Turbines, DTU Wind Energy. (DTU Wind Energy PhD; No. 0022(EN)), 2013.
- [25] J.N. Sørensen, C.W. Kock, A model for unsteady rotor aerodynamics, Journal of wind engineering and industrial aerodynamics 58(3) (1995) 259-275.

- [26] L. Vermeer, J.N. Sørensen, A. Crespo, Wind turbine wake aerodynamics, *Progress in aerospace sciences* 39(6) (2003) 467-510.
- [27] M.O.L. Hansen, J.N. Sørensen, S. Voutsinas, N. Sørensen, H.A. Madsen, State of the art in wind turbine aerodynamics and aeroelasticity, *Progress in aerospace sciences* 42(4) (2006) 285-330.
- [28] J. Johansen, H.A. Madsen, M. Gaunaa, C. Bak, N.N. Sørensen, Design of a wind turbine rotor for maximum aerodynamic efficiency, *Wind Energy* 12(3) (2009) 261-273.
- [29] J.N. Sørensen, Aerodynamic aspects of wind energy conversion, *Annual Review of Fluid Mechanics* 43 (2011) 427-448.
- [30] M.O. Hansen, *Aerodynamics of wind turbines*, Routledge 2015.
- [31] H. Glauert, *Airplane Propellers in Aerodynamic Theory* (WF Durand, ed.), Division L, Chapter XI, Springer Verlag, Berlin, 1935.
- [32] B. Pedersen, State of the Art of aero-elastic Codes for Wind Turbine Calculations-summary, *Proceedings of the 28 th IEA Meeting of Experts "State of the Art of aero-elastic Codes for Wind Turbine Calculations, 1996*, pp. 207-208.
- [33] T. Burton, N. Jenkins, D. Sharpe, E. Bossanyi, *Aerodynamics of horizontal axis wind turbines*, *Wind Energy Handbook, Second Edition* (2001) 39-136.
- [34] V. Esfahanian, A.S. Pour, I. Harsini, A. Haghani, R. Pasandeh, A. Shahbazi, G. Ahmadi, Numerical analysis of flow field around NREL Phase II wind turbine by a hybrid CFD/BEM method, *Journal of Wind Engineering and Industrial Aerodynamics* 120 (2013) 29-36.
- [35] H. Yang, W. Shen, H. Xu, Z. Hong, C. Liu, Prediction of the wind turbine performance by using BEM with airfoil data extracted from CFD, *Renewable Energy* 70 (2014) 107-115.
- [36] R.L.U. de Freitas Pinto, B.P.F. Gonçalves, A revised theoretical analysis of aerodynamic optimization of horizontal-axis wind turbines based on BEM theory, *Renewable Energy* 105 (2017) 625-636.
- [37] R.E. Wilson, P.B. Lissaman, S.N. Walker, *Aerodynamic performance of wind turbines*, Oregon State University Corvallis, Oregon 1976.
- [38] J.H. Strickland, B. Webster, T. Nguyen, A vortex model of the Darrieus turbine: an analytical and experimental study, *Journal of Fluids Engineering* 101(4) (1979) 500-505.
- [39] R. Bareiß, S. Wagner, The free wake/hybrid wake code ROVLM-A tool for aerodynamic analysis of wind turbines, *Proc. of the European Wind Turbine Conference, 1993*, pp. 424-431.

BIBLIOGRAPHY

- [40] T. Sant, G. van Kuik, G. Van Bussel, Estimating the angle of attack from blade pressure measurements on the NREL phase VI rotor using a free wake vortex model: axial conditions, *Wind Energy* 9(6) (2006) 549-577.
- [41] D. Micallef, M. Kloosterman, C.S. Ferreira, G. Van Bussel, T. Sant, Validating BEM, direct and inverse free wake models with the MEXICO experiment, 48th AIAA Aerospace Sciences Meeting including the New Horizons Forum and Aerospace Exposition, Orlando, USA, 4-7 January 2010; AIAA 2010-462, American Institute of Aeronautics and Astronautics (AIAA), 2010.
- [42] G. Tescione, C.S. Ferreira, G. van Bussel, Analysis of a free vortex wake model for the study of the rotor and near wake flow of a vertical axis wind turbine, *Renewable Energy* 87 (2016) 552-563.
- [43] H.A. Madsen, A CFD analysis of the actuator disc flow compared with momentum theory results, 10th IEA meeting on aerodynamics, Technical University of Denmark. Department of Fluid Mechanics, 1997, pp. 109-124.
- [44] J. Sørensen, W. Shen, X. Munduate, Analysis of wake states by a full-field actuator disc model, *Wind Energy* 1(2) (1998) 73-88.
- [45] C. Masson, A. Smaïli, C. Leclerc, Aerodynamic analysis of HAWTs operating in unsteady conditions, *Wind Energy* 4(1) (2001) 1-22.
- [46] R. Mikkelsen, J.N. Sørensen, W.Z. Shen, Modelling and analysis of the flow field around a coned rotor, *Wind Energy* 4(3) (2001) 121-135.
- [47] W.Z. Shen, J. Sørensen, Numerical modeling of wind turbine wakes, *J. Fluids Eng* 124(2) (2002) 393-399.
- [48] I. Dobrev, F. Massouh, M. Rapin, Actuator surface hybrid model, *Journal of Physics: Conference Series*, IOP Publishing, 2007, p. 012019.
- [49] W.Z. Shen, J.N. Sørensen, J. Zhang, Actuator surface model for wind turbine flow computations, 2007 European Wind Energy Conference and Exhibition, 2007.
- [50] W.Z. Shen, J.H. Zhang, J.N. Sørensen, The actuator surface model: a new Navier–Stokes based model for rotor computations, *Journal of Solar Energy Engineering* 131(1) (2009) 011002.
- [51] N. Troldborg, J.N. Sørensen, R. Mikkelsen, Numerical simulations of wake characteristics of a wind turbine in uniform inflow, *Wind Energy* 13(1) (2010) 86-99.
- [52] N. Troldborg, G.C. Larsen, H.A. Madsen, K.S. Hansen, J.N. Sørensen, R. Mikkelsen, Numerical simulations of wake interaction between two wind turbines at various inflow conditions, *Wind Energy* 14(7) (2011) 859-876.
- [53] J. Johansen, N.N. Sørensen, Aerofoil characteristics from 3D CFD rotor computations, *Wind Energy* 7(4) (2004) 283-294.

BIBLIOGRAPHY

- [54] N. Sorensen, J. Michelsen, S. Schreck, Navier-Stokes predictions of the NREL phase VI rotor in the NASA Ames 80-by-120 wind tunnel, ASME 2002 Wind Energy Symposium, American Society of Mechanical Engineers, 2002, pp. 94-105.
- [55] A. Tadamasa, M. Zangeneh, Numerical prediction of wind turbine noise, *Renewable Energy* 36(7) (2011) 1902-1912.
- [56] G. Yu, X. Shen, X. Zhu, Z. Du, An insight into the separate flow and stall delay for HAWT, *Renewable Energy* 36(1) (2011) 69-76.
- [57] M. Moshfeghi, Y.J. Song, Y.H. Xie, Effects of near-wall grid spacing on SST-K- ω model using NREL Phase VI horizontal axis wind turbine, *Journal of Wind Engineering and Industrial Aerodynamics* 107 (2012) 94-105.
- [58] N.J. Choi, S.H. Nam, J.H. Jeong, K.C. Kim, Numerical study on the horizontal axis turbines arrangement in a wind farm: Effect of separation distance on the turbine aerodynamic power output, *Journal of Wind Engineering and Industrial Aerodynamics* 117 (2013) 11-17.
- [59] C. Lynch, M. Smith, Unstructured overset incompressible computational fluid dynamics for unsteady wind turbine simulations, *Wind Energy* 16(7) (2013) 1033-1048.
- [60] J.-O. Mo, A. Choudhry, M. Arjomandi, R. Kelso, Y.-H. Lee, Effects of wind speed changes on wake instability of a wind turbine in a virtual wind tunnel using large eddy simulation, *Journal of Wind Engineering and Industrial Aerodynamics* 117 (2013) 38-56.
- [61] A.M. AbdelSalam, V. Ramalingam, Wake prediction of horizontal-axis wind turbine using full-rotor modeling, *Journal of Wind Engineering and Industrial Aerodynamics* 124 (2014) 7-19.
- [62] M.A. Elfarra, N. Sezer-Uzol, I.S. Akmandor, NREL VI rotor blade: numerical investigation and winglet design and optimization using CFD, *Wind Energy* 17(4) (2014) 605-626.
- [63] M.C. Hsu, I. Akkerman, Y. Bazilevs, Finite element simulation of wind turbine aerodynamics: validation study using NREL Phase VI experiment, *Wind Energy* 17(3) (2014) 461-481.
- [64] D.O. Yu, O.J. Kwon, Predicting wind turbine blade loads and aeroelastic response using a coupled CFD-CSD method, *Renewable Energy* 70 (2014) 184-196.
- [65] A.C. Aranake, V.K. Lakshminarayan, K. Duraisamy, Computational analysis of shrouded wind turbine configurations using a 3-dimensional RANS solver, *Renewable Energy* 75 (2015) 818-832.

- [66] M. Carrión, R. Steijl, M. Woodgate, G. Barakos, X. Munduate, S. Gomez-Iradi, Computational fluid dynamics analysis of the wake behind the MEXICO rotor in axial flow conditions, *Wind Energy* 18(6) (2015) 1023-1045.
- [67] M. Ghasemian, A. Nejat, Aerodynamic noise prediction of a horizontal axis wind turbine using improved delayed detached eddy simulation and acoustic analogy, *Energy Conversion and Management* 99 (2015) 210-220.
- [68] B. Plaza, R. Bardera, S. Visiedo, Comparison of BEM and CFD results for MEXICO rotor aerodynamics, *Journal of Wind Engineering and Industrial Aerodynamics* 145 (2015) 115-122.
- [69] S. Sicklinger, C. Lerch, R. Wüchner, K.-U. Bletzinger, Fully coupled co-simulation of a wind turbine emergency brake maneuver, *Journal of Wind Engineering and Industrial Aerodynamics* 144 (2015) 134-145.
- [70] S.A. Abdulqadir, H. Iacovides, A. Nasser, The physical modelling and aerodynamics of turbulent flows around horizontal axis wind turbines, *Energy* (2016).
- [71] X. Cai, R. Gu, P. Pan, J. Zhu, Unsteady aerodynamics simulation of a full-scale horizontal axis wind turbine using CFD methodology, *Energy Conversion and Management* 112 (2016) 146-156.
- [72] K. Lee, Z. Huque, R. Kommalapati, S.-E. Han, Evaluation of equivalent structural properties of NREL phase VI wind turbine blade, *Renewable Energy* 86 (2016) 796-818.
- [73] M.-H. Lee, Y. Shiah, C.-J. Bai, Experiments and numerical simulations of the rotor-blade performance for a small-scale horizontal axis wind turbine, *Journal of Wind Engineering and Industrial Aerodynamics* 149 (2016) 17-29.
- [74] R. Rafiee, M. Tahani, M. Moradi, Simulation of aeroelastic behavior in a composite wind turbine blade, *Journal of Wind Engineering and Industrial Aerodynamics* 151 (2016) 60-69.
- [75] N.N. Sørensen, F. Zahle, K. Boorsma, G. Schepers, CFD computations of the second round of MEXICO rotor measurements, *Journal of Physics: Conference Series*, IOP Publishing, 2016, p. 022054.
- [76] A. Sudhamshu, M.C. Pandey, N. Sunil, N. Satish, V. Mugundhan, R.K. Velamati, Numerical study of effect of pitch angle on performance characteristics of a HAWT, *Engineering Science and Technology, an International Journal* 19(1) (2016) 632-641.
- [77] L. Wang, R. Quant, A. Kolios, Fluid structure interaction modelling of horizontal-axis wind turbine blades based on CFD and FEA, *Journal of Wind Engineering and Industrial Aerodynamics* 158 (2016) 11-25.

BIBLIOGRAPHY

- [78] A. Bouhelal, A. Smaili, C. Masson, O. Guerri, Effects of Surface Roughness on Aerodynamic Performance of Horizontal Axis Wind Turbines, The 25th Annual Conference of the Computational Fluid Dynamics Society of Canada, CFD2017-337, University of Windsor. (2017).
- [79] M.O. Hansen, J. Johansen, Tip studies using CFD and comparison with tip loss models, *Wind Energy* 7(4) (2004) 343-356.
- [80] L. Prandtl, A. Betz, Vier abhandlungen zur hydrodynamik und aerodynamik, 3 (1927).
- [81] R.E. Wilson, P. Lissaman, Applied aerodynamics of wind power machines, [Corvallis, Or., Oregon State University]1974.
- [82] O.d. Vries, Fluid dynamic aspects of wind energy conversion, Advisory Group for Aerospace Research and Development NEUILLY-SUR-SEINE (France), 1979.
- [83] W.Z. Shen, R. Mikkelsen, J.N. Sørensen, C. Bak, Tip loss corrections for wind turbine computations, *Wind Energy* 8(4) (2005) 457-475.
- [84] E. Branlard-Mac Gaunaa, Development of new tip-loss corrections based on vortex theory and vortex methods.
- [85] J.L. Tangler, M.S. Selig, An evaluation of an empirical model for stall delay due to rotation for HAWTs, National Renewable Energy Lab., Golden, CO (United States), 1997.
- [86] T. Wang, A brief review on wind turbine aerodynamics, *Theoretical and Applied Mechanics Letters* 2(6) (2012).
- [87] H. Snel, R. Houwink, J. Bosschers, Sectional prediction of lift coefficients on rotating wind turbine blades in stall, Netherlands Energy Research Foundation Petten, Netherlands1994.
- [88] Z. Du, M.S. Selig, A 3-D stall-delay model for horizontal axis wind turbine performance prediction, AIAA paper 21 (1998) 9-19.
- [89] Z. Du, M. Selig, The effect of rotation on the boundary layer of a wind turbine blade, *Renewable Energy* 20(2) (2000) 167-181.
- [90] P. Chaviaropoulos, M.O. Hansen, Investigating three-dimensional and rotational effects on wind turbine blades by means of a quasi-3D Navier-Stokes solver, *Journal of Fluids Engineering* 122(2) (2000) 330-336.
- [91] C. Lindenburg, Modelling of rotational augmentation based on engineering considerations and measurements, European Wind Energy Conference, London, 2004, pp. 22-25.
- [92] H. Dumitrescu, V. Cardoso, A. Dumitrache, Modelling of inboard stall delay due to rotation, *Journal of Physics: Conference Series*, IOP Publishing, 2007, p. 012022.

BIBLIOGRAPHY

- [93] H. Dumitrescu, V. Cardoso, Inboard stall delay due to rotation, *Journal of aircraft* 49(1) (2012) 101-107.
- [94] C. Bak, J. Johansen, P.B. Andersen, Three-dimensional corrections of airfoil characteristics based on pressure distributions, *Proceedings of the European Wind Energy Conference*, 2006, pp. 1-10.
- [95] G.J. Leishman, *Principles of helicopter aerodynamics with CD extra*, Cambridge university press 2006.
- [96] O. Guerri, A. Hamdouni, A. Sakout, Fluid structure interaction of wind turbine airfoils, *Wind Engineering* 32(6) (2008) 539-557.
- [97] J.W. Larsen, S.R. Nielsen, S. Krenk, Dynamic stall model for wind turbine airfoils, *Journal of Fluids and Structures* 23(7) (2007) 959-982.
- [98] S. Guntur, N.N. Sørensen, S. Schreck, L. Bergami, Modeling dynamic stall on wind turbine blades under rotationally augmented flow fields, *Wind Energy* 19(3) (2016) 383-397.
- [99] L. CARR, Progress in analysis and prediction of dynamic stall, *Journal of aircraft* 25(1) (1988) 6-17.
- [100] L. Ericsson, J. Reding, Fluid mechanics of dynamic stall part I. Unsteady flow concepts, *Journal of fluids and structures* 2(1) (1988) 1-33.
- [101] L. Ericsson, J. Reding, Fluid mechanics of dynamic stall part II. Prediction of full scale characteristics, *Journal of Fluids and Structures* 2(2) (1988) 113-143.
- [102] S. Gupta, J.G. Leishman, Dynamic stall modelling of the S809 aerofoil and comparison with experiments, *Wind Energy* 9(6) (2006) 521-547.
- [103] D.W. Gross, F.D. Harris, Prediction of in-flight stalled airloads from oscillating airfoil data, 25th Annual Forum of the American Helicopter Society, 1969, pp. 14-16.
- [104] F. Tarzanin, Prediction of control loads due to blade stall, *Journal of the American Helicopter Society* 17(2) (1972) 33-46.
- [105] C. Tran, D. Petot, Semi-empirical model for the dynamic stall of airfoils in view of the application to the calculation of responses of a helicopter blade in forward flight, (1980).
- [106] J.G. Leishman, T. Beddoes, A Semi-Empirical Model for Dynamic Stall, *Journal of the American Helicopter society* 34(3) (1989) 3-17.
- [107] S. Øye, Dynamic stall simulated as time lag of separation, *Proceedings of the 4th IEA Symposium on the Aerodynamics of Wind Turbines*, Rome, Italy, 1991.
- [108] M.H. Hansen, M. Gaunaa, H.A. Madsen, A Beddoes-Leishman type dynamic stall model in state-space and indicial formulations, (2004).

BIBLIOGRAPHY

- [109] C.E. Lynch, Advanced CFD methods for wind turbine analysis, Georgia Institute of Technology, 2011.
- [110] R. Lanzafame, M. Messina, Fluid dynamics wind turbine design: Critical analysis, optimization and application of BEM theory, *Renewable energy* 32(14) (2007) 2291-2305.
- [111] J. Tangler, D. Kocurek, Wind turbine post-stall airfoil performance characteristics guidelines for blade-element momentum methods, 43rd AIAA Aerospace Sciences Meeting and Exhibit, 2005, p. 591.
- [112] I.F.S.A. Kabir, E. Ng, Insight into stall delay and computation of 3D sectional aerofoil characteristics of NREL phase VI wind turbine using inverse BEM and improvement in BEM analysis accounting for stall delay effect, *Energy* 120 (2017) 518-536.
- [113] G.-H. Cottet, P.D. Koumoutsakos, *Vortex methods: theory and practice*, Cambridge university press 2000.
- [114] L. Prandtl, *Applications of modern hydrodynamics to aeronautics*, (1923).
- [115] J.-J. Chattot, Helicoidal vortex model for wind turbine aeroelastic simulation, *Computers & structures* 85(11) (2007) 1072-1079.
- [116] K. Badreddinne, H. Ali, A. David, Optimum project for horizontal axis wind turbines ‘OPHWT’, *Renewable Energy* 30(13) (2005) 2019-2043.
- [117] F. Coton, T. Wang, The prediction of horizontal axis wind turbine performance in yawed flow using an unsteady prescribed wake model, *Proceedings of the Institution of Mechanical Engineers, Part A: Journal of Power and Energy* 213(1) (1999) 33-43.
- [118] S. Gupta, Development of a time-accurate viscous Lagrangian vortex wake model for wind turbine applications, 2006.
- [119] S.D. Pasmajoglou, J. Graham, Prediction of aerodynamic forces on horizontal axis wind turbines in free yaw and turbulence, *Journal of Wind Engineering and Industrial Aerodynamics* 86(1) (2000) 1-14.
- [120] S.G. Voutsinas, Vortex methods in aeronautics: how to make things work, *International Journal of Computational Fluid Dynamics* 20(1) (2006) 3-18.
- [121] J.L. Hess, Review of integral-equation techniques for solving potential-flow problems with emphasis on the surface-source method, *Computer Methods in Applied Mechanics and Engineering* 5(2) (1975) 145-196.
- [122] L.L. Erickson, *Panel methods: An introduction*, (1990).
- [123] I. Paraschivoiu, *Aérodynamique subsonique*, Presses inter Polytechnique 1998.

BIBLIOGRAPHY

- [124] C. Masson, I. Paraschivoiu, Description et comparaison de cinq methodes de panneaux en deux dimensions, Dép. de génie mécanique, École polytechnique1990.
- [125] M. Drela, XFOIL: An analysis and design system for low Reynolds number airfoils, Low Reynolds number aerodynamics, Springer1989, pp. 1-12.
- [126] E.L. Houghton, P.W. Carpenter, Aerodynamics for engineering students, Butterworth-Heinemann2003.
- [127] J.L. Hess, A.M.O. Smith, Calculation of potential flow about arbitrary bodies, Progress in Aerospace Sciences 8 (1967) 1-138.
- [128] H. Abedi, L. Davidson, S. Voutsinas, Vortex method application for aerodynamic loads on rotor blades, EWEA 2013: Europe's Premier Wind Energy Event, Vienna, 4-7 February 2013, 2013, pp. 912-921.
- [129] J.N. Sørensen, P.S. Larsen, B.M. Pedersen, J.T. Jensen, Three-level, viscous-inviscid interaction technique for the prediction of separated flow past rotating wing, Technical University of DenmarkDanmarks Tekniske Universitet, AdministrationAdministration, Office for Finance and AccountingAfdelingen for Økonomi og Regnskab, 1986.
- [130] B. Mughal, M. Drela, A calculation method for the three-dimensional boundary-layer equations in integral form, AIAA Paper 786 (1993).
- [131] W. Rankin, On the mechanical principles of the action of propellers, Trans. Inst. Naval Architects 6 (1865) 13-39.
- [132] R.E. Froude, On the part played in propulsion by differences of fluid pressure, Trans. Inst. Naval Architects 30 (1889) 390.
- [133] B. Sanderse, S. Pijl, B. Koren, Review of computational fluid dynamics for wind turbine wake aerodynamics, Wind energy 14(7) (2011) 799-819.
- [134] I. Ammara, C. Leclerc, C. Masson, A viscous three-dimensional differential/actuator-disk method for the aerodynamic analysis of wind farms, Transactions-American Society of Mechanical Engineers Journal of Solar Energy Engineering 124(4) (2002) 345-356.
- [135] A. Jimenez, A. Crespo, E. Migoya, J. García, Advances in large-eddy simulation of a wind turbine wake, Journal of Physics: Conference Series, IOP Publishing, 2007, p. 012041.
- [136] C. Masson, I. Ammara, I. Paraschivoiu, An aerodynamic method for the analysis of isolated horizontal-axis wind turbines, International Journal of Rotating Machinery 3(1) (1997) 21-32.

BIBLIOGRAPHY

- [137] L.M. Tossas, S. Leonardi, Wind turbine modeling for computational fluid dynamics: December 2010-December 2012, National Renewable Energy Laboratory (NREL), Golden, CO., 2013.
- [138] J. Sørensen, W.Z. Shen, Numerical modeling of wind turbine wakes, *J. Fluids Eng* 124(2) (2002) 393-399.
- [139] S. Ivanell, J.N. Sørensen, R. Mikkelsen, D. Henningson, Analysis of numerically generated wake structures, *Wind Energy* 12(1) (2009) 63-80.
- [140] R. Mikkelsen, J.N. Sørensen, S. Øye, N. Troldborg, Analysis of power enhancement for a row of wind turbines using the actuator line technique, *Journal of Physics: Conference Series*, IOP Publishing, 2007, p. 012044.
- [141] K. Nilsson, W.Z. Shen, J.N. Sørensen, S.P. Breton, S. Ivanell, Validation of the actuator line method using near wake measurements of the MEXICO rotor, *Wind Energy* 18(3) (2015) 499-514.
- [142] R. Mikkelsen, Actuator disc methods applied to wind turbines, Technical University of Denmark (2003).
- [143] S. Sarmast, W.Z. Shen, W.J. Zhu, R.F. Mikkelsen, S. Breton, S. Ivanell, Validation of the actuator line and disc techniques using the New MEXICO measurements, *Journal of Physics: Conference Series*, IOP Publishing, 2016, p. 032026.
- [144] C. Sibuet Watters, C. Masson, Modeling of lifting-device aerodynamics using the actuator surface concept, *International journal for numerical methods in fluids* 62(11) (2010) 1264-1298.
- [145] R. Arieli, M. Tauber, Computation of subsonic and transonic flow about lifting rotor blades, (1979).
- [146] C. Borland, D. Rizzetta, H. Yoshihar, Numerical solution of three-dimensional unsteady transonic flow over swept wings, *AIAA Journal* 20(3) (1982) 340-347.
- [147] N. Sankar, J. Malone, Y. Tassa, An implicit conservative algorithm for steady and unsteady three-dimensional transonic potential flows, *AIAA Paper* 811016 (1981) 199-212.
- [148] F. Caradonna, C. Tung, A. Desopper, Finite difference modeling of rotor flows including wake effects, *Journal of the American Helicopter Society* 29(2) (1984) 26-33.
- [149] N. Sankar, B. Wake, S. Lekoudis, Solution of the unsteady Euler equations for fixed and rotor wing configurations, *Journal of Aircraft* 23(4) (1986) 283-289.
- [150] A. Jameson, Solution of the Euler equations for complex configurations, No. 83-1929 (1983).

BIBLIOGRAPHY

- [151] R. Agarwal, J. Deese, Euler calculations for flowfield of a helicopter rotor in hover, *Journal of Aircraft* 24(4) (1987) 231-238.
- [152] G. Srinivasan, W. McCroskey, Navier-Stokes calculations of hovering rotor flowfields, *Journal of Aircraft* 25(10) (1988) 865-874.
- [153] G. Srinivasan, V. Raghavan, E. Duque, W. McCroskey, Flowfield Analysis of Modern Helicopter Rotors in Hover by Navier-Stokes Method, *Journal of the American Helicopter Society* 38(3) (1993) 3-13.
- [154] G. Srinivasan, J. Baeder, S. Obayashi, W. McCroskey, Flowfield of a lifting rotor in hover-A Navier-Stokes simulation, *AIAA journal* 30(10) (1992) 2371-2378.
- [155] M.E. Berkman, L.N. Sankar, C.R. Berezin, M.S. Torok, Navier-Stokes/full potential/free-wake method for rotor flows, *Journal of aircraft* 34(5) (1997) 635-640.
- [156] M.O.L. Hansen, J.N. Sørensen, J.A. Michelsen, N.N. Sørensen, A global Navier-Stokes rotor prediction model, *AIAA Paper* 97 (1997).
- [157] N.N. Sørensen, M.O.L. Hansen, Rotor performance predictions using a Navier-Stokes method, 36th AIAA Aerospace Sciences Meeting and Exhibit, American Institute of Aeronautics & Astronautics, 1997, pp. 52-59.
- [158] E.P. Duque, C. Van Dam, S.C. Hughes, Navier-Stokes simulations of the NREL combined experiment phase II rotor, *EWEC-CONFERENCE-*, 1999, pp. 79-84.
- [159] B.S. Baldwin, H. Lomax, Thin layer approximation and algebraic model for separated turbulent flows, *American Institute of Aeronautics and Astronautics* 1978.
- [160] N.N. Sørensen, J. Michelsen, S. Schreck, Navier-Stokes predictions of the NREL phase VI rotor in the NASA Ames 80 ft \times 120 ft wind tunnel, *Wind Energy* 5(2-3) (2002) 151-169.
- [161] S. Benjanirat, L.N. Sankar, G. Xu, Evaluation of turbulence models for the prediction of wind turbine aerodynamics, *AIAA paper* 517 (2003) 2003.
- [162] N. Tachos, A. Filios, D. Margaris, A comparative numerical study of four turbulence models for the prediction of horizontal axis wind turbine flow, *Proceedings of the Institution of Mechanical Engineers, Part C: Journal of Mechanical Engineering Science* 224(9) (2010) 1973-1979.
- [163] R. Lanzafame, S. Mauro, M. Messina, Wind turbine CFD modeling using a correlation-based transitional model, *Renewable Energy* 52 (2013) 31-39.
- [164] J. Van Ingen, The eN method for transition prediction: Historical review of work at TU Delft, *AIAA* 2008.

BIBLIOGRAPHY

- [165] J. Valentine, R. Decker, A Lagrangian-Eulerian scheme for flow around an airfoil in rain, *International journal of multiphase flow* 21(4) (1995) 639-648.
- [166] M.G. Khalfallah, A.M. Koliub, Effect of dust on the performance of wind turbines, *Desalination* 209(1-3) (2007) 209-220.
- [167] M. Parsi, M. Agrawal, V. Srinivasan, R.E. Vieira, C.F. Torres, B.S. McLaury, S.A. Shirazi, CFD simulation of sand particle erosion in gas-dominant multiphase flow, *Journal of Natural Gas Science and Engineering* 27 (2015) 706-718.
- [168] G. Xu, J. Wang, CFD modeling of particle dispersion and deposition coupled with particle dynamical models in a ventilated room, *Atmospheric Environment* 166 (2017) 300-314.
- [169] L. Kang, L. Guo, Eulerian–Lagrangian simulation of aeolian sand transport, *Powder technology* 162(2) (2006) 111-120.
- [170] C. Paz, E. Suarez, C. Gil, M. Concheiro, Numerical study of the impact of windblown sand particles on a high-speed train, *Journal of Wind Engineering and Industrial Aerodynamics* 145 (2015) 87-93.
- [171] W.P. Adamczyk, A. Klimanek, R.A. Białecki, G. Węcel, P. Kozolub, T. Czakiert, Comparison of the standard Euler–Euler and hybrid Euler–Lagrange approaches for modeling particle transport in a pilot-scale circulating fluidized bed, *Particuology* 15 (2014) 129-137.
- [172] Z. Zhang, Q. Chen, Comparison of the Eulerian and Lagrangian methods for predicting particle transport in enclosed spaces, *Atmospheric environment* 41(25) (2007) 5236-5248.
- [173] A.F. Ansys, 17.0 Theory Guide, ANSYS inc (2017).
- [174] L. Kang, G. Zhao, X. Zou, C. Zhang, H. Cheng, An improved particle counting method for particle volume concentration in aeolian sand transport, *Powder Technology* 280 (2015) 191-200.
- [175] A. Mansouri, H. Arabnejad, S. Karimi, S.A. Shirazi, B.S. McLaury, Improved CFD modeling and validation of erosion damage due to fine sand particles, *Wear* 338 (2015) 339-350.
- [176] ANSYS_Fluent, 17 Documentation, 2017.
- [177] A.N. Kolmogorov, Dissipation of energy in locally isotropic turbulence, *Dokl. Akad. Nauk SSSR*, 1941, pp. 16-18.
- [178] A.N. Kolmogorov, The local structure of turbulence in incompressible viscous fluid for very large Reynolds numbers, *Dokl. Akad. Nauk SSSR*, 1941, pp. 299-303.

BIBLIOGRAPHY

- [179] J. Smagorinsky, General circulation experiments with the primitive equations: I. The basic experiment, *Monthly weather review* 91(3) (1963) 99-164.
- [180] M. Germano, U. Piomelli, P. Moin, W.H. Cabot, A dynamic subgrid-scale eddy viscosity model, *Physics of Fluids A: Fluid Dynamics* 3(7) (1991) 1760-1765.
- [181] W.-W. Kim, S. Menon, A new dynamic one-equation subgrid-scale model for large eddy simulations, 33rd Aerospace Sciences Meeting and Exhibit, 1995, p. 356.
- [182] F. Nicoud, F. Ducros, Subgrid-scale stress modelling based on the square of the velocity gradient tensor, *Flow, turbulence and Combustion* 62(3) (1999) 183-200.
- [183] D. You, P. Moin, A dynamic global-coefficient subgrid-scale eddy-viscosity model for large-eddy simulation in complex geometries, *Physics of Fluids* 19(6) (2007) 065110.
- [184] P.R. Spalart, Strategies for turbulence modelling and simulations, *International Journal of Heat and Fluid Flow* 21(3) (2000) 252-263.
- [185] O. Reynolds, On the dynamical theory of incompressible viscous fluids and the determination of the criterion, *Proceedings of the Royal Society of London* 56(336-339) (1894) 40-45.
- [186] D.C. Wilcox, *Turbulence modeling for CFD*, DCW industries La Canada, CA1998.
- [187] F.G. Schmitt, About Boussinesq's turbulent viscosity hypothesis: historical remarks and a direct evaluation of its validity, *Comptes Rendus Mécanique* 335(9-10) (2007) 617-627.
- [188] J. Boussinesq, *Essai sur la théorie des eaux courantes*, Imprimerie nationale 1877.
- [189] J. Blazek, *Computational fluid dynamics: principles and applications*, Butterworth-Heinemann 2015.
- [190] P. Spalart, S. Allmaras, A one-equation turbulence model for aerodynamic flows, 30th aerospace sciences meeting and exhibit, 1992, p. 439.
- [191] B.E. Launder, D.B. Spalding, *Lectures in mathematical models of turbulence*, (1972).
- [192] V. Yakhot, S.A. Orszag, Renormalization group analysis of turbulence. I. Basic theory, *Journal of scientific computing* 1(1) (1986) 3-51.
- [193] T.-H. Shih, W.W. Liou, A. Shabbir, Z. Yang, J. Zhu, A new k- ϵ eddy viscosity model for high reynolds number turbulent flows, *Computers & Fluids* 24(3) (1995) 227-238.
- [194] F.R. Menter, Two-equation eddy-viscosity turbulence models for engineering applications, *AIAA journal* 32(8) (1994) 1598-1605.

- [195] D.K. Walters, D. Cokljat, A three-equation eddy-viscosity model for Reynolds-averaged Navier–Stokes simulations of transitional flow, *Journal of fluids engineering* 130(12) (2008) 121401.
- [196] R.B. Langtry, F.R. Menter, Correlation-based transition modeling for unstructured parallelized computational fluid dynamics codes, *AIAA journal* 47(12) (2009) 2894-2906.
- [197] M. Gibson, B. Launder, Ground effects on pressure fluctuations in the atmospheric boundary layer, *Journal of Fluid Mechanics* 86(3) (1978) 491-511.
- [198] S. Fu, B. Launder, M. Leschziner, Modelling strongly swirling recirculating jet flow with Reynolds-stress transport closures, 6th Symposium on Turbulent Shear Flows, 1987, pp. 17-6.
- [199] B.E. Launder, Second-moment closure: present... and future?, *International Journal of Heat and Fluid Flow* 10(4) (1989) 282-300.
- [200] B.E. Launder, Second-moment closure and its use in modelling turbulent industrial flows, *International Journal for Numerical Methods in Fluids* 9(8) (1989) 963-985.
- [201] V. Yakhot, S. Orszag, S. Thangam, T. Gatski, C. Speziale, Development of turbulence models for shear flows by a double expansion technique, *Physics of Fluids A: Fluid Dynamics* 4(7) (1992) 1510-1520.
- [202] D.C. Wilcox, Formulation of the kw turbulence model revisited, *AIAA journal* 46(11) (2008) 2823-2838.
- [203] R.B. Langtry, F. Menter, S. Likki, Y. Suzen, P. Huang, S. Völker, A correlation-based transition model using local variables—part II: test cases and industrial applications, *Journal of Turbomachinery* 128(3) (2006) 423-434.
- [204] F.R. Menter, R.B. Langtry, S. Likki, Y. Suzen, P. Huang, S. Völker, A correlation-based transition model using local variables—Part I: model formulation, *Journal of turbomachinery* 128(3) (2006) 413-422.
- [205] B. Launder, G.J. Reece, W. Rodi, Progress in the development of a Reynolds-stress turbulence closure, *Journal of fluid mechanics* 68(3) (1975) 537-566.
- [206] C.T. Crowe, J.D. Schwarzkopf, M. Sommerfeld, Y. Tsuji, *Multiphase flows with droplets and particles*, CRC press 2011.
- [207] A. Gosman, E. Loannides, Aspects of computer simulation of liquid-fueled combustors, *Journal of Energy* 7(6) (1983) 482-490.
- [208] S. Morsi, A. Alexander, An investigation of particle trajectories in two-phase flow systems, *Journal of Fluid Mechanics* 55(2) (1972) 193-208.

BIBLIOGRAPHY

- [209] A. Li, G. Ahmadi, Dispersion and deposition of spherical particles from point sources in a turbulent channel flow, *Aerosol science and technology* 16(4) (1992) 209-226.
- [210] P. Saffman, The lift on a small sphere in a slow shear flow, *Journal of fluid mechanics* 22(2) (1965) 385-400.
- [211] L. Fingersh, D. Simms, M. Hand, D. Jager, J. Cotrell, M. Robinson, S. Schreck, S. Larwood, Wind tunnel testing of NREL's unsteady aerodynamics experiment, 20th 2001 ASME Wind Energy Symposium, 2001, p. 35.
- [212] D. Simms, S. Schreck, M. Hand, L. Fingersh, NREL unsteady aerodynamics experiment in the NASA-Ames wind tunnel: a comparison of predictions to measurements, National Renewable Energy Laboratory, Golden, CO, Report No. NREL/TP-500-29494 (2001).
- [213] S. Schreck, The NREL full-scale wind tunnel experiment Introduction to the special issue, *Wind Energy* 5(2-3) (2002) 77-84.
- [214] H. Snel, J. Schepers, B. Montgomerie, The MEXICO project (Model Experiments in Controlled Conditions): The database and first results of data processing and interpretation, *Journal of Physics: Conference Series*, IOP Publishing, 2007, p. 012014.
- [215] K. Boorsma, J. Schepers, New Mexico Experiment, Preliminary overview with initial validation, Technical report, Energy Research Center of the Netherlands, ECN, 2014.
- [216] H. Snel, G. Schepers, N. Siccama, Mexico Project: the database and results of data processing and interpretation, 47th AIAA Aerospace Sciences Meeting Including the New Horizons Forum and Aerospace Exposition, 2009, p. 1217.
- [217] J. Schepers, K. Boorsma, S. Gomez-Iradi, P. Schaffarczyk, H.A. Madsen, N.N. Sørensen, W.Z. Shen, T. Lutz, C. Schulz, I. Herraiez, S. Schreck, Final report of IEA Wind Task 29: Mexnext (Phase 2), (2014).
- [218] L. Oggiano, K. Boorsma, G. Schepers, M. Kloosterman, Comparison of simulations on the NewMexico rotor operating in pitch fault conditions, *Journal of Physics: Conference Series*, IOP Publishing, 2016, p. 022049.
- [219] S.A. Abdulqadir, H. Iacovides, A. Nasser, The physical modelling and aerodynamics of turbulent flows around horizontal axis wind turbines, *Energy* 119 (2017) 767-799.
- [220] Y. Li, K.-J. Paik, T. Xing, P.M. Carrica, Dynamic overset CFD simulations of wind turbine aerodynamics, *Renewable Energy* 37(1) (2012) 285-298.
- [221] H. Schlichting, K. Gersten, E. Krause, H. Oertel, *Boundary-layer theory*, Springer1955.

- [222] B. Launder, B. Sharma, Application of the energy-dissipation model of turbulence to the calculation of flow near a spinning disc, *Letters in heat and mass transfer* 1(2) (1974) 131-137.
- [223] O. Cadot, *Introduction à la turbulence, cours de l'ENSTA-ParisTech 2A*, ENSTA-ParisTech, 2013.
- [224] T. Craft, S. Gant, H. Iacovides, B. Launder, Development and application of a new wall function for complex turbulent flows, *ECCOMAS CFD Conference*, Swansea, UK, 2001.
- [225] J. Luo, A. Gosman, Prediction of impeller-induced flow in mixing vessels using multiple frames of reference, *INSTITUTE OF CHEMICAL ENGINEERS SYMPOSIUM SERIES*, 1994.
- [226] J.R. Cash, A.H. Karp, A variable order Runge-Kutta method for initial value problems with rapidly varying right-hand sides, *ACM Transactions on Mathematical Software (TOMS)* 16(3) (1990) 201-222.
- [227] C.T. Crowe, M.P. Sharma, D.E. Stock, The particle-source-in cell (PSI-CELL) model for gas-droplet flows, *Journal of fluids engineering* 99(2) (1977) 325-332.
- [228] C.-l. Lin, P. Fox, A. Ecer, N. Satofuka, J. Periaux, *Parallel Computational Fluid Dynamics' 98: Development and Applications of Parallel Technology*, Elsevier1999.
- [229] P. Li, S.J. Eckels, N. Zhang, G.W. Mann, Effects of Parallel Processing on Large Eddy Simulations in ANSYS Fluent, *ASME 2016 Fluids Engineering Division Summer Meeting collocated with the ASME 2016 Heat Transfer Summer Conference and the ASME 2016 14th International Conference on Nanochannels, Microchannels, and Minichannels*, American Society of Mechanical Engineers, 2016, pp. V01BT26A004-V01BT26A004.
- [230] S. Tekkouk, *Le calcul de haute performance appliqué à l'étude du comportement électromagnétique des structures en matériaux composites d'un avion*, Université du Québec à Trois-Rivières, 2014.
- [231] N.N. Sørensen, A. Bechmann, P.E. Réthoré, F. Zahle, Near wake Reynolds-averaged Navier–Stokes predictions of the wake behind the MEXICO rotor in axial and yawed flow conditions, *Wind Energy* 17(1) (2014) 75-86.
- [232] X. Liu, Z. Dong, Experimental investigation of the concentration profile of a blowing sand cloud, *Geomorphology* 60(3) (2004) 371-381.
- [233] M. Benhammou, B. Draoui, M. Hamouda, Improvement of the summer cooling induced by an earth-to-air heat exchanger integrated in a residential building under hot and arid climate, *Applied Energy* 208 (2017) 428-445.

BIBLIOGRAPHY

- [234] E. ISO, 14688-1: 2002: Geotechnical investigation and testing–Identification and classification of soil–Part 1: Identification and description, British Standards Institution (2002).
- [235] H.D. Nedjari, S.K. Haddouche, A. Balehouane, O. Guerri, Optimal windy sites in Algeria: Potential and perspectives, *Energy* (2017).
- [236] M. Adaramola, O. Oyewola, On wind speed pattern and energy potential in Nigeria, *Energy Policy* 39(5) (2011) 2501-2506.
- [237] S. Diaf, G. Notton, D. Diaf, Technical and economic assessment of wind farm power generation at Adrar in Southern Algeria, *Energy Procedia* 42 (2013) 53-62.
- [238] T. Wakeman, W. Tabakoff, Measured particle rebound characteristics useful for erosion prediction, ASME 1982 International Gas Turbine Conference and Exhibit, American Society of Mechanical Engineers, 1982, pp. V003T05A005-V003T05A005.

Appendix A

MEXICO blade geometry

Table 9: Chord and twist distribution on the MEXICO blade [24].

Station Number	Span (m)	Chord (m)	Twist (°)	Profile Shape (-)
1	0	0.195	0	Cylinder
2	0.02	0.195	0	Cylinder
3	0.025	0.09	0	Cylinder
4	0.09	0.09	0	Cylinder
5	0.165	0.165	8.2	Transition (from 0.09 to 0.24)
6	0.24	0.24	16.4	DU91-W2-250
7	0.465	0.207	12.1	DU91-W2-250
8	0.690	0.178	8.3	DU91-W2-250
9	0.815	0.166	7.1	DU91-W2-250
10	0.915	0.158	6.1	Transition (from 0.815 to 1.015)
11	1.015	0.15	5.5	RISØ-A1-21
12	1.140	0.142	4.8	RISØ-A1-21
13	1.265	0.134	4	RISØ-A1-21
14	1.365	0.129	3.700	Transition (from 1.265 to 1.465)
15	1.465	0.123	3.2	NACA 64-418
16	1.59	0.116	2.6	NACA 64-418
17	1.815	0.102	1.5	NACA 64-418
18	1.955	0.092	0.7	NACA 64-418
19	1.983	0.082	0.469	NACA 64-418
20	2.012	0.056	0.231	NACA 64-418
21	2.04	0.011	0	NACA 64-418

Note that the span has been measured from the blade root (0.21 m from rotor center).

Appendix B

Numerical results of standard $k-\omega$ and $k-\omega$ BSL turbulence models

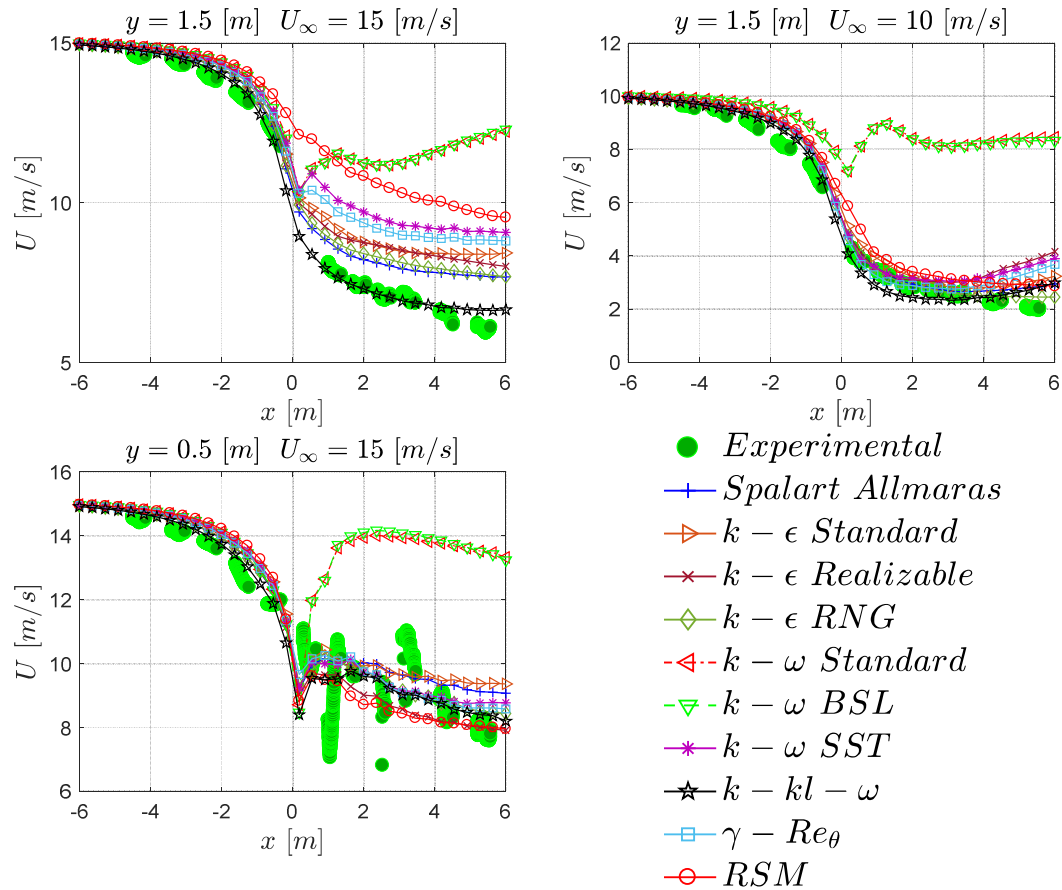


Figure 69: Comparison between different velocity components for different wind speeds.

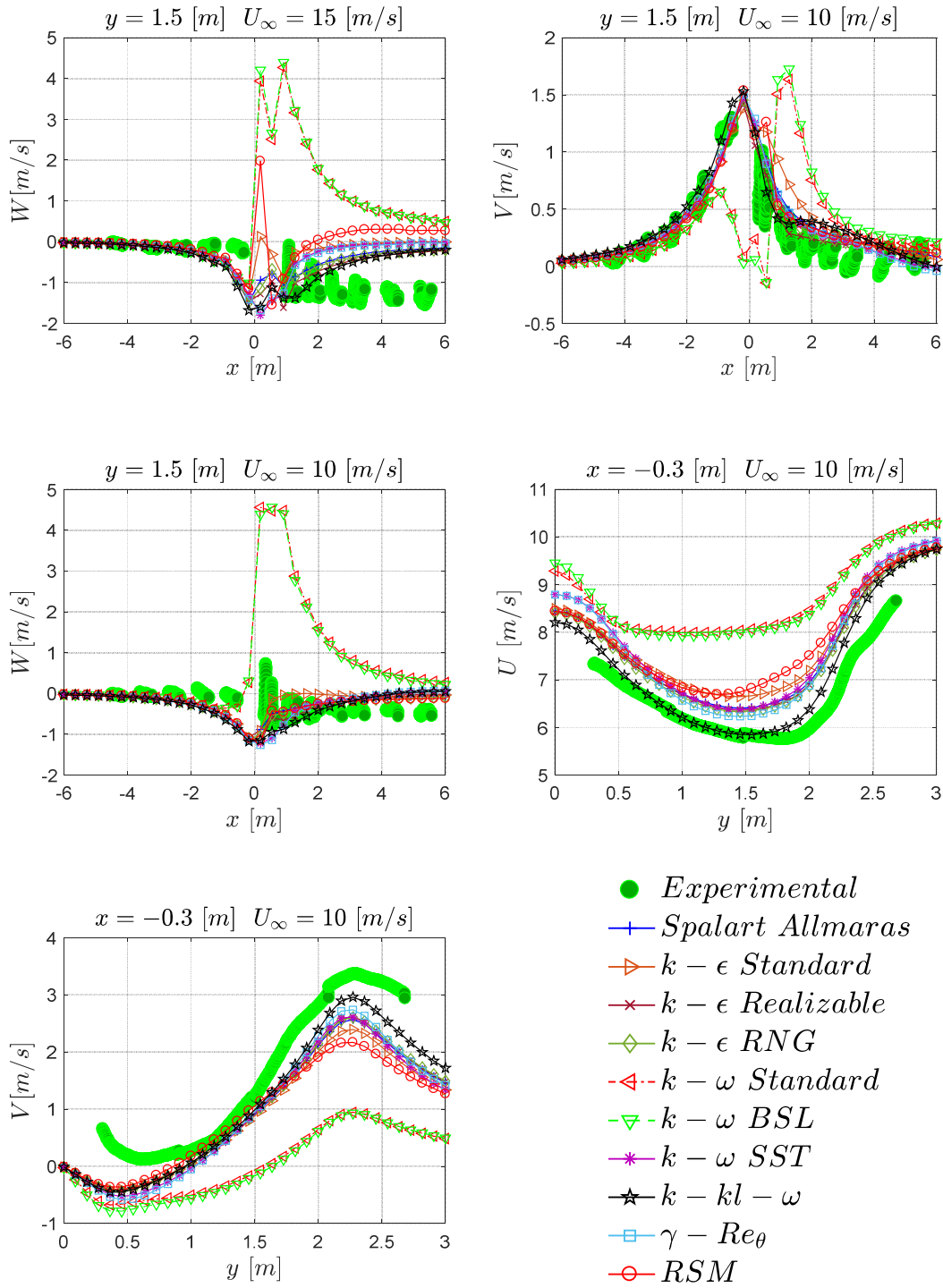


Figure 70: Comparison between different velocity components for $U_\infty=10$ m/s.

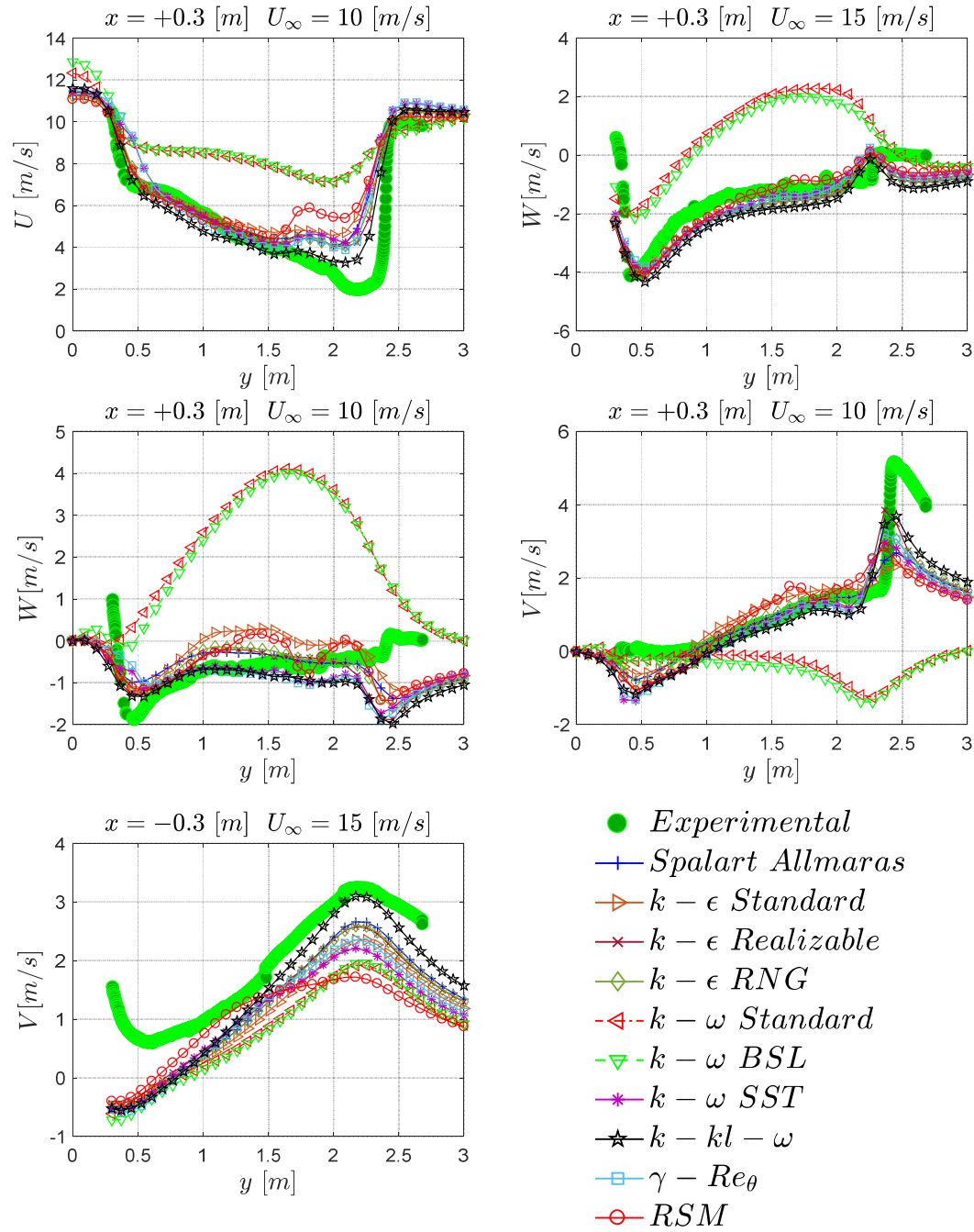


Figure 71: Comparison between different radial velocity components.

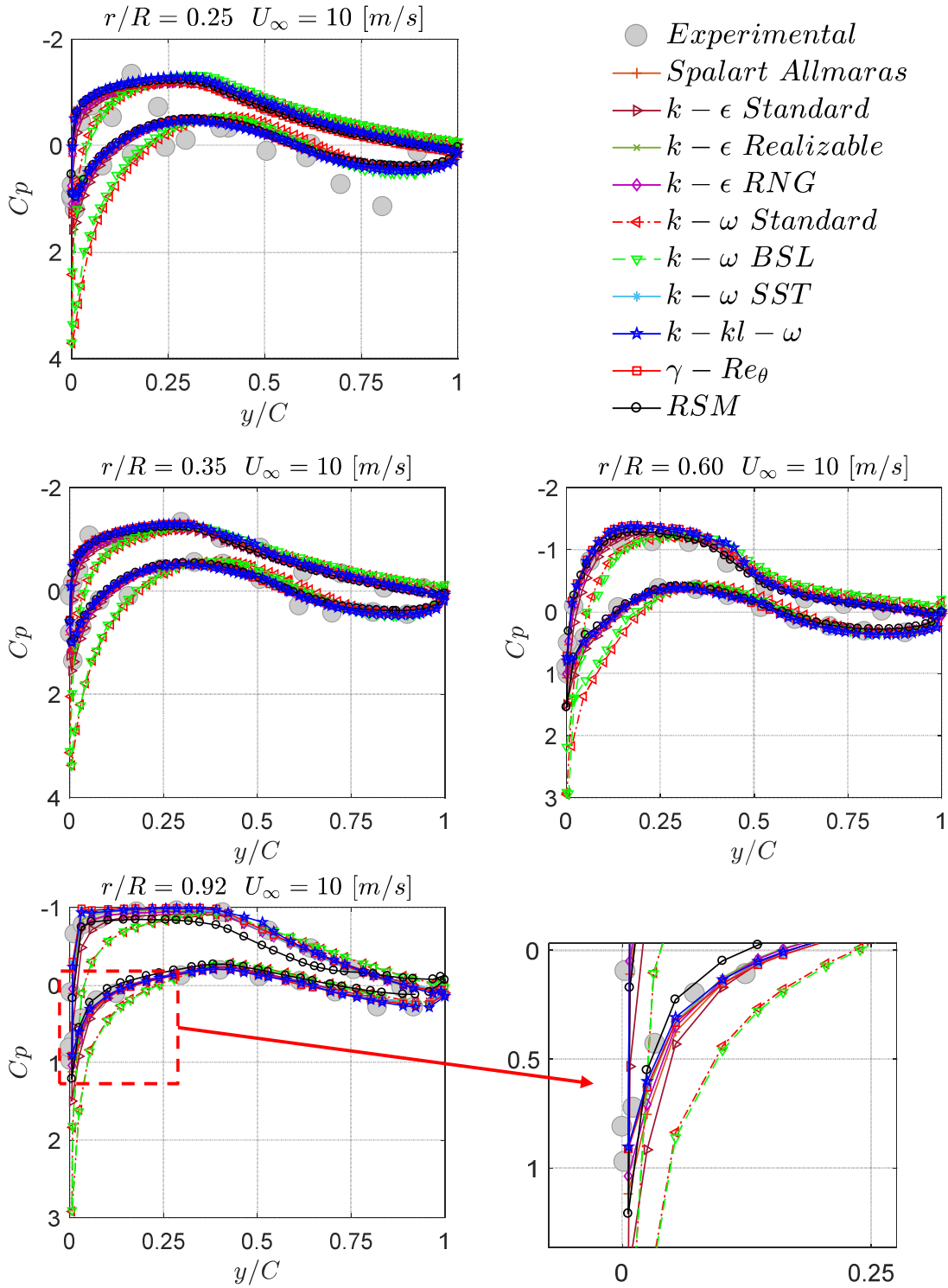


Figure 72: Comparison between simulated and measured pressure coefficient distributions using ten turbulence models, for $U_\infty = 10$ m/s.

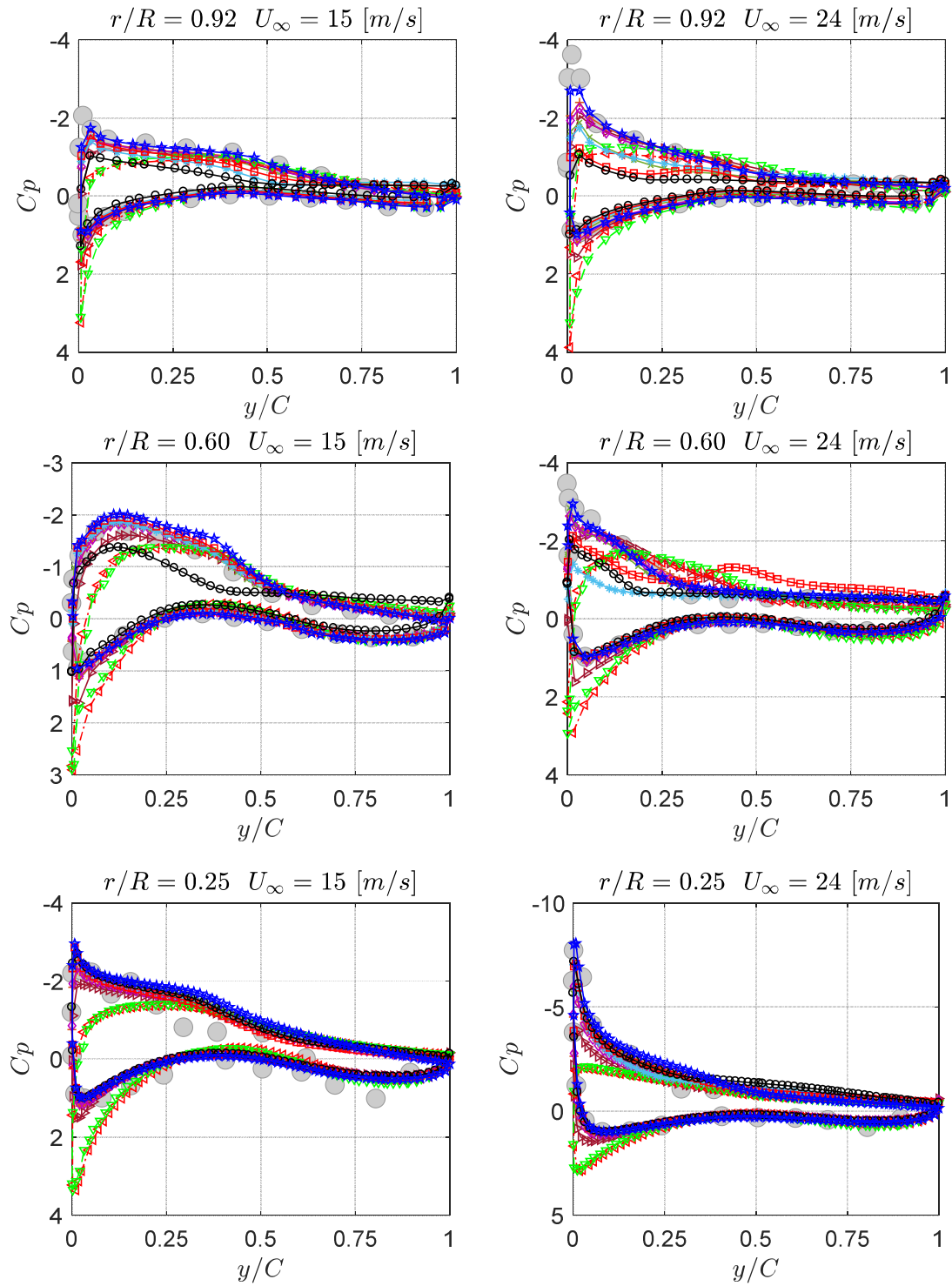


Figure 73: Comparison between simulated and measured pressure coefficient distributions using ten turbulence models, for $U_\infty = 15$ and 24 m/s.